Investigation of the charge transfer processes in bio-inorganic transition metal complexes

Dissertation
zur Erlangung des Doktorgrades
and der Fakultät für Mathematik, Informatik und Naturwissenschaften
Fachbereich Physik
der Universität Hamburg

Vorgelegt von
Mykola Biednov

Hamburg
2018

Gutachter der Dissertation:	Prof. Dr. Michael Rübhausen Prof. Dr. Nils Huse
Zusammensetzung der Prüfungskommission:	Prof. Dr. Michael Rübhausen Prof. Dr. Arwen Pearson Prof. Dr. Nils Huse Prof. Dr. Robin Santra Prof. Dr. Dorota Koziej
Vorsitzende/r der Prüfungskommission:	
Datum der Disputation:	5 Juli 2018
Vorsitzender Fach-Promotionsausschusses PHYSIK:	Prof. Dr. Wolfgang Hansen
Leiter des Fachbereichs PHYSIK:	Prof. Dr. Michael Potthoff
Dekan der Fakultät für Mathematik,	Prof. Dr. Heinrich Graener

Abstract

The versatility of transition metal complexes results in their frequent occurrence in nature and allows them to find many applications industry. The binuclear copper complex hemocyanin is capable of reversible oxygen binding and is the second most frequently found oxygen transport agent in nature. Another copper-containing enzyme tyrosinase is also able to reversibly bind molecular oxygen and plays an important role in the production cycle of melanin. The cytochrome c oxidase is a transmembrane complex that contains several iron and copper sites and is a part of the electron transport chain in the membrane of bacteria.

Small synthetic complexes are good model systems to study how the ligand environment and organization of the central metal core affect the properties of the complex.

Within the scope of the thesis, the ground and excited state structure, as well as electronic properties of five different transition metal complexes were characterized. For the mononuclear $Cu(TMGqu)_2$ and $Fe(Pz_2Py)_2$ complexes pump-probe X-ray absorption measurements at the P11 beamline of the PETRA III synchrotron were performed. The measurements allowed to extract the lifetime of the optically excited state of both complexes, to determine the oxidation state of the central metal atom and the geometry of the $Cu(TMGqu)_2$ molecule in the ground and excited state and also to make assumptions about the spin multiplicity of the excited state of the $Fe(Pz_2Py)_2$ complex. X-ray photoelectron spectroscopy measurements on the $Cu(DMEGqu)_2$ complex allowed to confirm the oxidation state of the central copper atom in the complex, as well as to extract the core level binding energies of the nitrogen atoms, in order to provide a deeper insight into the distribution of electron density in the complex. A low temperature resonant Raman spectroscopy study on the oxygenated form of the [Cu(btmgp)]I and $[Cu(TMG_2tol)]_2$ species confirmed the capability of these complexes to bind molecular oxygen.

In addition to the investigation of the transition metal complexes, a special approach was developed and used to align the vacuum-ultraviolet Raman spectrometer, that is permanently installed as an experimental end-station at the free-electron laser FLASH in Hamburg. The alignment approach is based on optical laser interferometry, Hartmann-Shack wavefront-sensing and off-line soft X-ray measurements. The experimental techniques were additionally supported by extensive optical simulations.

Kurzfassung

Die Vielseitigkeit von Übergangsmetallkomplexen ermöglicht es ihnen, verschiedene Anwendungen in der Natur und in der Industrie zu finden. Der binukleare Kupferkomplex Hämocyanin ist in der Lage, Sauerstoff reversibel zu binden und ist der zweithäufigste Sauerstofftransporter in der Natur. Ein weiteres kupferhaltiges Enzym, Tyrosinase, ist ebenfalls in der Lage, molekularen Sauerstoff reversibel zu binden und spielt eine wichtige Rolle im Produktionszyklus von Melanin. Die cytochrom-c-Oxidase ist ein Transmembrankomplex, der mehrere Eisen- und Kupferzentren enthält und Teil der Elektronentransportkette in der Membran von Bakterien ist.
Kleine synthetische Komplexe dienen als gute Modelle dafür, die Einflüsse der unterschiedlichen Ligandenumgebung und die Anordnung des zentralen Metallkerns auf die Eigenschaften des Komplexes zu untersuchen.
Im Rahmen der vorliegenden Arbeit wurden Grund- und angeregte Zustände, sowie elektronische Eigenschaften von fünf verschiedenen Übergangsmetallkomplexen charakterisiert. Für die mononuklearen $Cu(TMGqu)_2$- und $Fe(Pz_2Py)_2$-Komplexe wurden Röntgenabsorptionsmessungen an der P11 Beamline des PETRA III Synchrotrons durchgeführt. Die Messungen erlaubten es, die Lebensdauer des optisch angeregten Zustandes beider Komplexe zu bestimmen, den Oxidationszustand des zentralen Metallatoms und die Geometrie des $Cu(TMGqu)_2$-Moleküls im Grund- und angeregten Zustand zu erhalten und auch Annahmen über die Spinmultiplizität des angeregten Zustandes des $Fe(Pz_2Py)_2$-Komplexes zu treffen. Röntgen Photoelektronenspektroskopie-Messungen am $Cu(DMEGqu)_2$-Komplex erlaubten es, den Oxidationszustand des zentralen Kupferatoms im Komplex zu bestätigen, sowie die Bindungsenergien der Stickstoffatome zu bestimmen und somit einen tieferen Einblick in die Verteilung der Elektronendichte im Komplex zu erlangen.
Eine resonante Raman-Studie bei tiefen Temperaturen an der oxygenierten Form von $[Cu(btmgp)]I$ und $[Cu(TMG_2tol)]_2$ bestätigte die Fähigkeit dieser Komplexe, molekularen Sauerstoff zu binden.
Neben der Untersuchung der Übergangsmetallkomplexe wurde ein spezieller Ansatz zur Justage des Vakuum-Ultraviolett-Raman-Spektrometers, welches als experimentelle Endstation am Freie-Elektronen Laser FLASH in Hamburg fest installiert ist, entwickelt

und eingesetzt. Dieser Justageansatz basiert auf der optischen Laserinterferometrie, der Hartmann-Shack-Wellenfrontsensorik und der Offline Weichröntgenmessung. Die experimentellen Techniken wurden zusätzlich durch umfangreiche optische Simulationen unterstützt.

Contents

Chapter 1

Introduction

1.1 Motivation

Transition metal complexes play an important role in nature, as well as in different branches of industry [1–3]. They can perform various functions like electron transfer, reversible oxygen binding or selective mediation of specific chemical reactions. Biological function appears to be closely connected to the structure of the transition metal complex and often at a first glance very similar molecules perform completely different chemical functions [1, 4–7]. It is therefore of a great importance to understand relation of the geometric and electronic structures to the function of the complex to be able to mimic and tailor it in future.

The ability of bioinorganic chemists to synthesize small model complexes with varying organization of the central metal core and ligand environment along with the advances in modern spectroscopic techniques, allows to perform very systematic studies of these complexes not only in their ground state, but also in the excited state and more importantly to understand transition dynamics and unveil possible photochemical pathways.

Another important aspect is the development in instrumentation itself – a key to perform better experiments and deliver data with unprecedented level of quality and detail and, potentially, uncover new effects, that were unreachable before. Therefore, a lot of effort was devoted to alignment of the unique VUV Raman spectrometer at the PG1 beamline of the Free-Electron Laser FLASH. The VUV Raman spectrometer is designed to study quasiparticle excitations at L and M absorption edges of transition metals with high resolution and unique stray-light rejection capabilities at ultrafast timescales.

1.2 Material systems and phenomena

Within the thesis, structure, electronic and optical properties of the $Fe(Pz_2Py)_2$, $Cu(TMGqu)_2$, $Cu(DMEGqu)_2$, [Cu(btmgp)]I and $[Cu(TMG_2tol)]_2$ complexes were in-

vestigated. $Fe(Pz_2Py)_2$ complex belongs to a class of compounds, that exhibit a *Spin Crossover* (SCO) phenomenon upon the optical excitation [2, 8]. Upon absorption of a photon of light and subsequent relaxation, central Iron atom changes its spin state from singlet to predominantly quintet, with a maximum of four unpaired electrons in the $3d$ orbitals for the $3d^6$ electronic configuration. The change of a spin state is accompanied by the very distinct change in the structure and optical properties of the molecule. This phenomenon opens a pathway for a new generation of optically controlled magnetic switches that can find applications in screen technology or data storage devices [2].
$Cu(TMGqu)_2$ and $Cu(DMEGqu)_2$ complexes belong to a class of mononuclear metaloproteins, that exhibit *entatic state* properties. *Entatic state* means predistortion of the molecular geometry towards the structural transition, that effectively lowers the potential barrier and facilitates the transition [9,10]. $Cu(TMGqu)_2$ and $Cu(DMEGqu)_2$ can switch their oxidation state between Cu(I) and Cu(II) via optical *metal to ligand charge transfer* (MLCT) transition [6]. This change in the oxidation state is accompanied by a change in the geometry of the molecule, that ideally prefers square planar organization in the Cu(I) state and tetrahedral for the Cu(II). Implication of the sterically demanding ligands does not allow the molecule to take either of the geometries and distorts them towards the intermediate geometry, lowering the barrier for the transition between both states [11].
Finally, [Cu(btmgp)]I and $[Cu(TMG_2tol)]_2$ are the model complexes, that mimic activity of the natural tyrosinase enzyme [12, 13]. The active site of the tyrosinase is formed by two Cu atoms, that can form a peroxide core by binding the molecular oxygen [1,14]. The formed intermediate is highly reactive for selective oxidation of phenols and is a critical element in the production cycle of melanine and other pigments.

Chapter 2

Theory

In this section important electronic properties of the transition metal complexes as well as their interaction with ligand molecules will be introduced. This will be followed by the theoretical aspects of studied phenomena and measurement techniques.

2.1 $3d$-transition metal complexes

Transition metals [15] are referred to as chemical elements or their ions with partially filled d-subshell. The electron configuration of transition metals can be generally written as $(n-1)d^{1-10}ns^{0-2}$ reflecting the concurrence between filling of the s levels with larger main quantum number n and d levels with main quantum number $n-1$. The lightest transition metal element is Scandium with an atomic number 21 and electron configuration $3d^1 4s^2$. Here concurrence between $4s$ and $3d$ levels is obvious: first $4s$ energy level is filled with two electrons and only then $3d$ subshell starts to be filled. In the periodic table, transition metals are elements from the groups 3-12 (fig. 2.1).
Transition metal ions are usually found in various oxidation states like +1 and +2 for copper, +2 to +7 for manganese, or even up to +8 for ruthenium and osmium. The accessibility of the different oxidation states is an important feature of this class of ions that is responsible for their rich chemistry.
Chemical properties of the transition metal complexes can be conveniently explained within the *Crystal field theory* (CFT) [1, 15]. This theory is mostly applicable to the description of the properties of elements with incomplete d and f subshells. within this work focus the focus lies on the d-levels. Within the CFT, ligands, that surround the central transition metal ion are represented as negative point charges and their effect on the electronic levels of the metal is studied. The distribution of the electron density for the $3d$-level is shown in fig. 2.2. The $3d$-level consists of five electron orbitals that can be occupied by a maximum of ten electrons, according to the Pauli principle. As can be seen, two orbitals are located along the cartesian axes and three others have their electron

density distributed between the axes. If a transition metal ion is located in a spherically

	III	IV	V	VI	VII	VIII	IX	X	XI	XII
4	21 Sc	22 Ti	23 V	24 Cr	25 Mn	26 Fe	27 Co	28 Ni	29 Cu	30 Zn
5	39 Y	40 Zr	41 Nb	42 Mo	43 Tc	44 Ru	45 Rh	46 Pd	47 Ag	48 Cd
6	71 Lu	72 Hf	73 Ta	74 W	75 Re	76 Os	77 Ir	78 Pt	79 Au	80 Hg

Figure 2.1: Block of the Periodic table with transition metals. Elements within each row have partially filled d-subshell of the same quantum number.

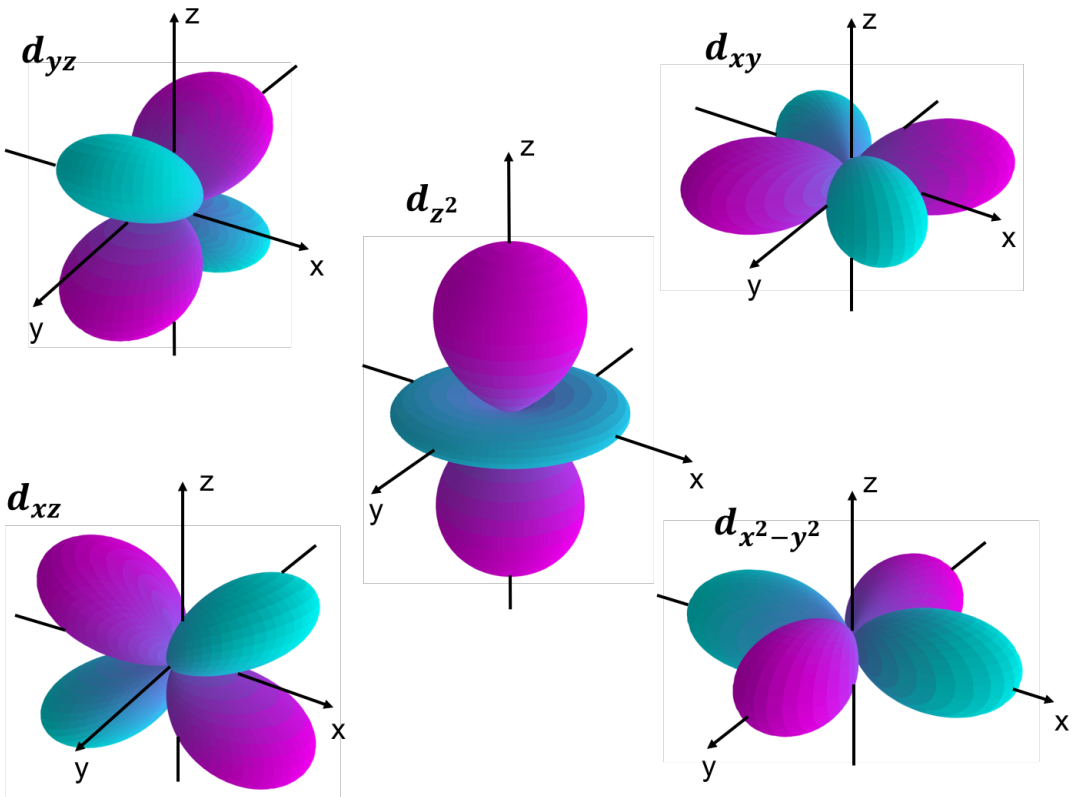

Figure 2.2: Distribution of the electron density for the atomic d-orbitals in the cartesian coordinate system.

symmetric ligand field, all five d-orbitals will increase their energy equally, changing the total energy of the atom or ion, but not affecting degeneracy of the electronic levels. However, in a ligand field with a lower symmetry, for example in the octahedral one (negative point charges are located on the x, y and z axis, fig. 2.3), the situation will be different. The electron density of the $d_{x^2-y^2}$ and d_{z^2} orbitals will have the strongest overlap with the ligand electronic orbitals, effectively increasing the energy of these two orbitals due to the increased electron repulsion. d_{xy}, d_{xz} and d_{yz} orbitals are located between the axes and therefore have lower energy becasue of a weaker electron repulsion. The resulting picture of the $3d$ energy levels and geometric location of the point charges, that represent the ligands is shown in fig. 2.3 [1]. As can be seen, degeneracy of the $3d$ levels is lifted and two bands are formed: three-fold degenerate t_{2g} band, formed by d_{xy}, d_{xz} and d_{yz} orbitals and two-fold degenerate e_g band formed by the $d_{x^2-y^2}$ and d_{z^2} orbitals. In the common case of the tetrahedral ligand field the location of the energy levels is inverted: t_{2g} band is formed by the d_{xy}, d_{xz} and d_{yz} orbitals and e_g by the $d_{x^2-y^2}$ and d_{z^2} orbitals. The energy difference Δ between them is referred to as *ligand-field splitting* 10Dq [15].

In general, magnitude of the ligand field splitting is proportional to the main quantum number of the orbital e.g. higher for $4d$ orbital than for $3d$ and is higher for the atoms in higher oxidation states. The dependence on the nature of the ligand is reflected in the experimentally derived spectrochemical series:

$$\mathrm{CO{>}CN{>}NO_2{>}NH_3{>}H_2O{>}F{>}HO{>}Cl{>}Br{>}I}$$

Crystal field splitting for these ligands decreases from left to right. Depending on the occupancy of the d-orbitals crystal field splitting might be a very important characterisitc that defines optical and magnetic properties of the complex [8,16]. Let us consider an ion in the octahedral field as an example. The ion has 3 orbitals with a lower energy and two orbitals with a higher energy. It is clear that for d^1, d^2 and d^3 electronic configurations the electrons will occupy t_{2g} set with one electron at each orbital, according to the Hunds rule. The same applies for d^8, d^9 and d^{10} configurations. A more complex picture is obtained for the intermediate occupancies d^4-d^7. As an example a d^6 configuration can be considered. For this configuration there are two ways how electrons can be distributed in the atomic orbitals: a high-spin and a low-spin. The realization of one of the states is defined by the ratio between the energy P, needed to add a second electron to the atomic orbital, already occupied with one electron and the crystal field splitting Δ. If $\Delta > P$ then all six electrons group in the t_{2g} level and the spin is zero. If $\Delta < P$ then the high spin state is realized with a maximum number of unpaired electrons. For the d^6 configuration this results in the quintet spin state with $S = 2$ and $\kappa = 5$. Such a situation can be observed for the Fe^{2+} ion.

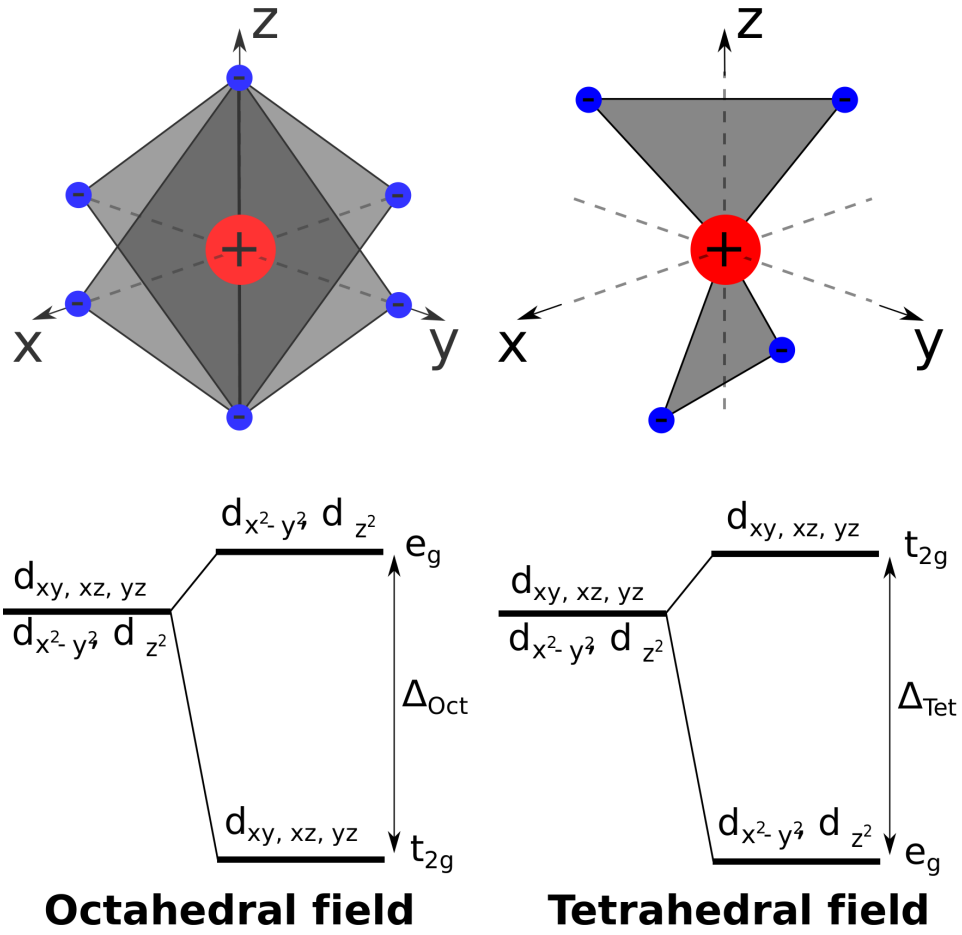

Figure 2.3: Spliting of the 3d energy levels into e_g and t_{2g} sets in octahedral and tetrahedral ligand fields. The ligand field splitting is marked as Δ.

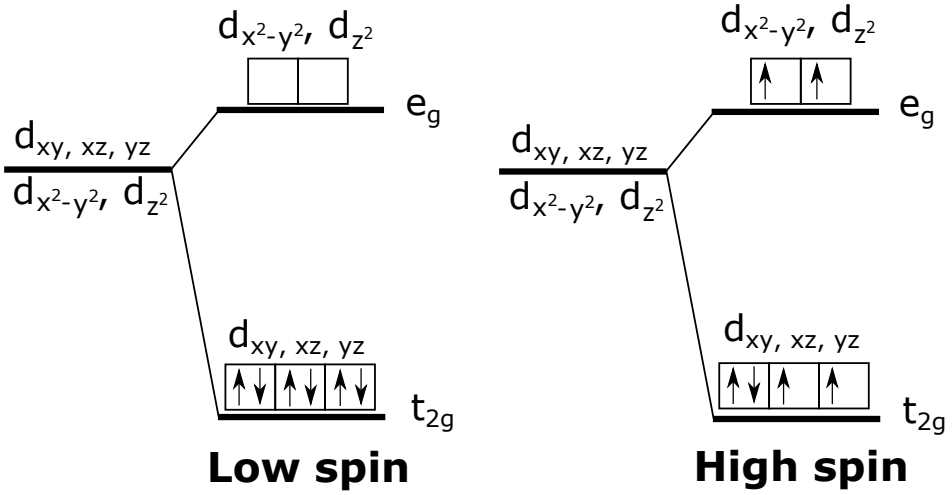

Figure 2.4: Occupancy of the $3d$ atomic orbitals in the octahedral ligand field in the low spin and high spin states for the $3d^6$ electron configuration.

2.2 Raman Scattering

Raman scattering is the process of the inelastic scattering of light by a material system, in which the energy shift between the scattered and the incident photons corresponds to a characteristic elementary excitation of the system [17–19]. A typical example of this excitation can be a phonon in a crystal [20,21] or a vibrational mode of a molecule [18]. The light wave can also be scattered by the free or bound charge carriers, plasmons, polaritons, magnons [20]. Historically this effect was independently observed by two groups: Mandelschtamm and Raman and Krischnan. Mandelschtamm observed symmetrically located satellites of the excitation line in the spectrum of light, scattered by a quartz crystal. Raman and Krischnan observed the same effect, working with liquids. In 1930 Raman was awarded the Nobel Prize in physics for his discovery. Its important to point

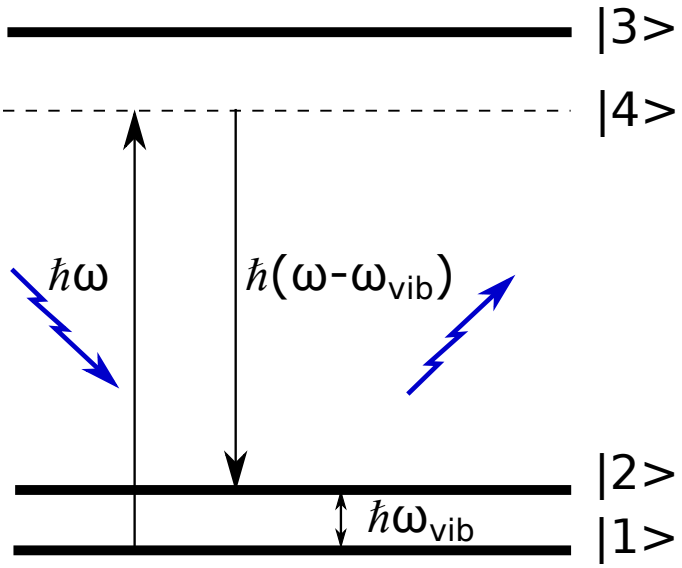

Figure 2.5: Energy level scheme of the Stokes Raman scattering. Incident photon has frequency ω. After the scattering, the scattered photon has decreased frequency $\omega - \omega_{vib}$, and a phonon with the energy $\hbar\omega_{vib}$ is left in the system.

out that the Raman spectra are plotted in the relative coordinate, that is calculated as the energy difference in inverse centimeters between the scattered and the incident photons. Depending on the sign of the energy shift Stokes and Anti-Stokes components of a Raman spectrum can be distinguished [17]. The stokes component represents a process in which the photon looses the energy upon the scattering and the Anti-Stokes represents the process in which the photon gains the energy upon scattering. To exhibit the antistokes scattering, system must be in the excited state so that the energy of the excitation can be transferred to the photon. Therefore, according to the Boltzman rule, at a room temperature Stokes component is usually dominant in intensity. In the visible spectral range, intensity ratio of the elastically scattered light to the inelastically scattered Stokes

component is on the order of 10^6. Typical energy shifts in the Raman spectra are ranging from few to thousands of inverse centimeters, which together with the low intensity of the scattered light puts strong demands to the bandwidth of the excitation source and the resolution of the spectrometer. A huge leap in Raman spectroscopy was brought by invention of laser in 1960s. Unprecedented bandwidth of He-Ne laser, frequency tunability of Organic dye or Ti:Sapphire based lasers along with the double- and triple-monochromator spectrometer design led to many exciting discoveries [20]. Nowadays Raman scattering is a versatile and powerfull tool used in many fields of science.

2.2.1 Classical theory of Raman Scattering

A simple but explanatory description of the basic aspects of the Raman Scaterring phenomenon can be given within the classical theory of electromagnetic radiation [19, 20]. Within the classical theory, scattering of light occurs due to oscillations of the dipole momentum of the system (molecule), induced by the incident light wave. The ability of the electron cloud to deform under an external electromagnetic field depends on the current configuration of the nuclei and if the nuclei are vibrating at some characteristic frequency, than the polarizability of the molecule will be modulated at this frequency. Therefore, within the classical approach, Raman scattering can be described as a result of the modulation of the induced dipole momentum by the vibrations of the molecule. Let us assume interaction of the electromagnetic wave

$$E = E_0 \cos(2\pi\nu_0 t) \tag{2.1}$$

with the amplitude E_0 that oscillates with the frequency ν_0 with a medium. In the simplest case induced dipole momentum $\vec{P}$ will be colinear with the incident wave $\vec{E}$ and their values will be proportional

$$\vec{P} = \alpha\vec{E} \tag{2.2}$$

where α is scalar polarisability of the system. If the polarisability is constant, i.e. $\alpha = \alpha_0$, then according to (2.2) and (2.1) we get

$$\vec{P} = \alpha_0\vec{E_0} \cos(2\pi\nu_0 t) \tag{2.3}$$

Thereby, induced dipole momentum is oscillating with the same frequency as the incident light wave. For such oscillating dipole, energy emitted in all directions in the unit of time can be calculated as

$$W_{\nu_0} = \frac{2}{3c^2}\left|\frac{d^2\vec{P}}{dt^2}\right|^2 = \frac{32\pi^2\nu_0^4}{3c^3}|\alpha_0|^2 E_0^2 \cos^2 2\pi\nu_0 t \tag{2.4}$$

As can be seen, phase and frequency of the scattered wave remain the same. Averaging over time yields

$$\overline{W_{\nu_0}} = \frac{16\pi^4\nu_0^4}{3c^3}|\alpha_0|^2 E_0^2 \tag{2.5}$$

When the polarisability of the scattering medium is not constant, expression (2.2) has to be modified. A typical example of the system with a time-dependent polarisability is a vibrating molecule: from a classical point of view molecular vibrations lead to the modulation of the polarisability with the frequency of the vibration. In this case the oscillating polarizability can be expressed as:

$$\alpha = \alpha_0 + \alpha_\nu \cos(2\pi\nu t) \tag{2.6}$$

where along with the constant term α, polarisability contains also a term, that is oscillating with a frequency ν. Then, instead of (2.3) we get

$$\vec{P} = \alpha_0 E_0 \cos(2\pi\nu_0 t) + \alpha_\nu E_0 \cos(2\pi\nu t)\cos(2\pi\nu_0 t) \tag{2.7}$$

which can be transformed into

$$\vec{P} = \alpha_0 E_0 \cos(2\pi\nu_0 t) + \frac{1}{2}\alpha_\nu E_0 \cos(2\pi(\nu-\nu_0)t) + \frac{1}{2}\alpha_\nu E_0 \cos(2\pi(\nu+\nu_0)t) \tag{2.8}$$

As can be seen, the first term is proportional only to the static part of the polarisability and oscillates with the frequency of the incident wave, which corresponds to the elastic (Rayleigh) scattering of light. The second and the third terms are oscillating at frequencies $\nu_0 - \nu$ and $\nu_0 + \nu$. These terms are responsible for the scattering of light with a shifted frequency with respect to that of the incident wave, i.e. Stokes and Anti-Stokes terms of the Raman scattering. The intensity of the Stokes component for an isolated molecule is:

$$\overline{W_{\nu_0-\nu}} = \frac{4\pi^4(\nu-\nu_0)^4}{3c^3}|\alpha_\nu|^2 E_0^2 \tag{2.9}$$

This intensity is proportional to the square of the amplitude of the incident wave, fourth power of the frequency of the scattered light and a square of the amplitude, with which the polarisability is modulated.

2.2.2 Polarisability tensor

The relation between the vectors of the incident electromagnetic wave and the induced dipole momentum (2.2) used in the previous paragraph is only valid for the atoms and some other systems with high symmetry. In general case components of the dipole momentum P_x, P_y, P_z are linear functions of the components E_x, E_y, E_z of the incident electromagnetic wave [19, 20]:

$$\begin{cases} P_x = \alpha_{xx}E_x + \alpha_{xy}E_y + \alpha_{xz}E_z \\ P_y = \alpha_{yx}E_x + \alpha_{yy}E_y + \alpha_{yz}E_z \\ P_z = \alpha_{zx}E_x + \alpha_{zy}E_y + \alpha_{zz}E_z \end{cases} \tag{2.10}$$

The values $\alpha_{\lambda\mu}$ form a polarizability tensor, that defines ability of the system to be polarized in different directions by differently oriented external electrical field. For example, α_{xy} characterizes the polarizability in the direction x by a field in the direction of y. The tensor $\alpha_{\lambda\mu}$ is symmetric, i.e. $\alpha_{\lambda\mu} = \alpha_{\mu\lambda}$. It is possible to define a coordinate system in such a way that non-diagonal components become zero. Then, relation 2.10 simplifies to

$$P_x = \alpha_x E_x, P_y = \alpha_y E_y, P_z = \alpha_z E_z \tag{2.11}$$

2.2.3 Quantum-Mechanical description

Let us assume a two-level quantum system with the energy levels E_0 and E_1, exposed to the external oscillating field $E = E_i \cos(\omega t)$ with a wavelength much larger than the characteristic system dimensions [18]. For the Raman Scattering energy of a quantum of this field must not be in resonance, i.e. $\omega \neq (E_1 - E_0)/h$, and we assume that the incident wave induces an oscillating dipole momentum in the system, that is then re-radiating. The unperturbed system has a Hamiltonian H^0, so that

$$H^0 \psi_n^0 = ih \frac{\partial \psi_n^0}{\partial t} \tag{2.12}$$

with ψ_n^0 set being a solution of this equation

$$H^0 \psi_n^0 = E_n^0 \psi_n^0 \tag{2.13}$$

with the stationary energy levels E_n^0. The Hamiltonian of the perturbed system will have the additional term, that describes the energy, that electrical dipole gains in the external electrical field

$$-PE_i \cos(\omega t) \tag{2.14}$$

where P is the induced dipole momentum of the system. Under the assumption of a small perturbing field, the wavefunction of the perturbed state can be expressed as

$$\psi_n = \psi_n^0 + \psi_n^1 + ... \tag{2.15}$$

and the resulting Schroedinger equation for the perturbed state with the first-order correction is

$$\Big(H^0 - PE_i \cos(\omega t)\Big)\Big(\psi_n^0 + \psi_n^1\Big) = ih \frac{\partial}{\partial t}\Big(\psi_n^0 + \psi_n^1\Big) \tag{2.16}$$

By using the solution for the unperturbed case (2.13) and inserting a unity in the equation in a form of

$$1 = \sum_r \left|\psi_r^0\right\rangle \left\langle\psi_r^0\right| \tag{2.17}$$

first-order correction for the perturbed wavefunction can be found [18] as

$$\psi_n^1 = \frac{1}{2h} \sum_r \psi_r^0 \Big(\frac{P_{rn} E_i}{\omega_{rn} - \omega} e^{-i(\omega_n + \omega)t} + \frac{P_{rn} E_i}{\omega_{rn} + \omega} e^{-i(\omega_n - \omega)t} \Big) \tag{2.18}$$

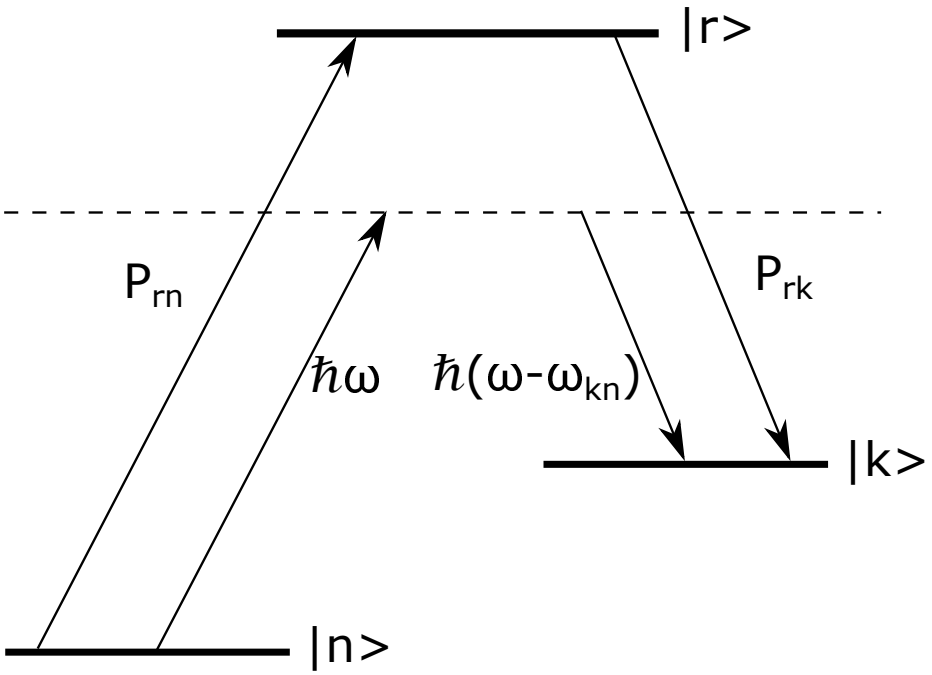

Figure 2.6: Energy-level scheme for the Stokes Raman scattering from the initial state $|n\rangle$ into final state $|k\rangle$. The figure is adapted from [18].

where $P_{rn} = \langle\psi_r^0|\, P\, |\psi_n^0\rangle$ are matrix elements of P.

According to the Fermis Golden Rule [20], transition probability is proportional to the square of the transition matrix element

$$M_{kn} = \langle\psi_k|\, P\, |\psi_n\rangle \approx \left\langle\psi_n^0 + \psi_n^1\right|\, P\, \left|\psi_n^0 + \psi_n^1\right\rangle \tag{2.19}$$

And the first-order perturbation theory yields the expression for the matrix element of the Raman transition from the state $|n\rangle$ to the state $|k\rangle$

$$M_{kn}^1 = \frac{e^{i(\omega_{kn}-\omega)t}}{2h} \sum_r \Big(\frac{P_{kr}(P_{rn}E_i)}{\omega_{rn}-\omega} + \frac{P_{rn}(P_{kr}E_i)}{\omega_{rk}+\omega} \Big) \tag{2.20}$$

Corresponding components of the polarizability tensor are then

$$\alpha_{ij} = \frac{1}{h} \sum_r \Big(\frac{(P_i)_{kr}(P_j)_{rn}}{\omega_{rn}-\omega} + \frac{(P_i)_{rn}(P_j)_{kr}}{\omega_{rk}+\omega} \Big) \tag{2.21}$$

where $i, j = x, y, z$ are Cartesian coordinates and summing takes place over all intermediate states $r \neq k, n$. In order to avoid discontinuities when the frequency of the incident light ω approaches that of the electronic transition ω_{rn}, a damping term $i\Gamma_r$ can be introduced into denominators, reflecting the finite lifetime of the intermediate states $|r\rangle$.

2.2.4 Selection rules

A molecule that consists of N atoms, has $r = 3N-6$ in general case and $r = 3N-5$ in the case of a linear molecule, vibrational degrees of freedom. But not all of these vibrations will show themselves in the Infrared or Raman spectra. Selection rules, that govern "activity" of the certain mode and its overtones are based on the symmetry of this mode and the presence of the anharmonicity [19]. If there is a mechanical harmonicity: potential energy is a quadratic function of the vibration coordinate and electrooptical harmonicity: dipole momentum and polarizability are linear functions of vibrational coordinates, than a system can be represented as quantum harmonic oscillator with discrete energy levels

$$E_n = h\nu(n+1), n = 0, 1, 2... \tag{2.22}$$

The only possible transition for such system is the transition, where $\Delta n = 0, \pm 1$. If the anharmonicity is present, than transitions, where the quantum number for a certain normal mode changes for a value, greater than 1, or several normal modes are changing their quantum numbers simultaneously, become possible. This results in the appearance of the overtones ($\Delta n > 1$) or combined frequencies ($\Delta n_i \neq 0, \Delta n_i \neq 0$) [19].
More general selection rules for the IR and Raman transitions from the state $|n\rangle$ to the state $|k\rangle$ are based on the matrix elements of the dipole momentum [18, 19]

$$P_{kn} = \langle \psi_k | \, P \, | \psi_n \rangle = \int_{-\infty}^{\infty} \psi_k^* P \psi_n dx \tag{2.23}$$

and the polarisability tensor (2.21). The transition is "allowed" if the corresponding matrix element has a non-zero value. According to (2.21), components of the polarizability tensor α_{ij} are formed by the products of the dipole moment matrix elements, and therefore, they transform like products of the Cartesian coordinates, $x^2, y^2, z^2, xy, xz, yz$ and the resulting symmetry for the dipole and polarizability matrix elements will be different. If a product of the type $\psi_k^* f \psi_n$ in (2.23) is an antisymmetric function, then integration yields zero and the corresponding transition is forbidden.
For the important case of centrosymmetric molecules, the ground state wave function has always g (odd) parity, as well as the components of the polarizability tensor. Therefore, in order for the Raman matrix element not to be zero, excited state wave function must also have g parity. Dipole momentum components always have u parity. Therefore, only transitions to levels with the same parity are IR allowed. This is known as the rule of mutual exclusion: if a molecule has a center of symmetry, then a vibration can be either infrared or Raman active, but not both [19]. A example of the rule of mutual exclusion, applied to the CO_2 molecule is shown in fig. 2.7.

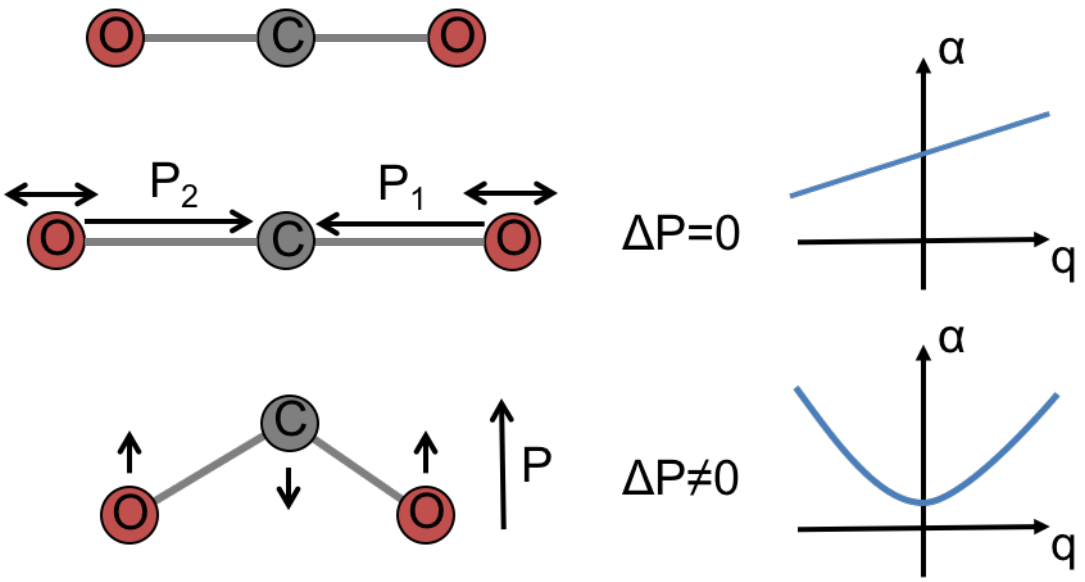

Figure 2.7: Comparison of the infrared- and Raman-active vibrations of the CO_2 molecule. q is the normal coordinate of the given vibration. The right part of the figure demonstrates the dependence of the polarizability of the molecule on the normal coordinate of the corresponding molecular vibration.

2.2.5 Resonance effects

As can be seen from formula (2.21), the values $(\alpha_{ij})_{nk}$ are defined by a sum of elements $\langle\psi_n| P_i |\psi_r\rangle \langle\psi_r| P_j |\psi_k\rangle$ over all possible intermediate states $|\psi_r\rangle$. Thus, the conventional Raman scattering involves all possible pathways between the initial and the final state through the intermediate states $|\psi_r\rangle$. In this case, direct information about the intermediate states cannot be obtained, and efficiently only the ground state electronic properties are probed. The situation changes, if the energy of the incident photon is close to the energy of the atomic or molecular transition ω_{rn}. Due to presence of a difference

$$\omega - \omega_{rn} - i\Gamma_r \tag{2.24}$$

in the denominator of the first term in (2.21), only the resonant term will dominate the sum, and the scattering cross-section will be enhanced. Separating the electronic and vibronic movements under the Born-Oppenheimer approximation and assuming that the electronic energy is a function of the normal coordinates for the molecule, equation (2.21) can be simplified to [19]:

$$(\alpha_{ij})_{kn} = \frac{1}{h}(P_i)_{e^g e^r}(P_j)_{e^r e^g} \sum_{v_k^r} \frac{\left\langle v_k^{f(g)} \middle| v_k^{r(r)} \right\rangle \left\langle v_k^{r(r)} \middle| v_k^{i(g)} \right\rangle}{\omega_{e^r v_k^r * e^g v_k^i} - \omega - \Gamma_{e^r v_k^r}} \tag{2.25}$$

where $|e^r\rangle$ and $\left|v^{(r)}\right\rangle$ are respectively the electronic and vibronic wave functions of the state r, the notation g stands for the ground state and r for the intermediate state. The assumption was made that the initial and final electronic state of the Raman transition is the ground state. According to the equation 2.25, in the resonant case, the

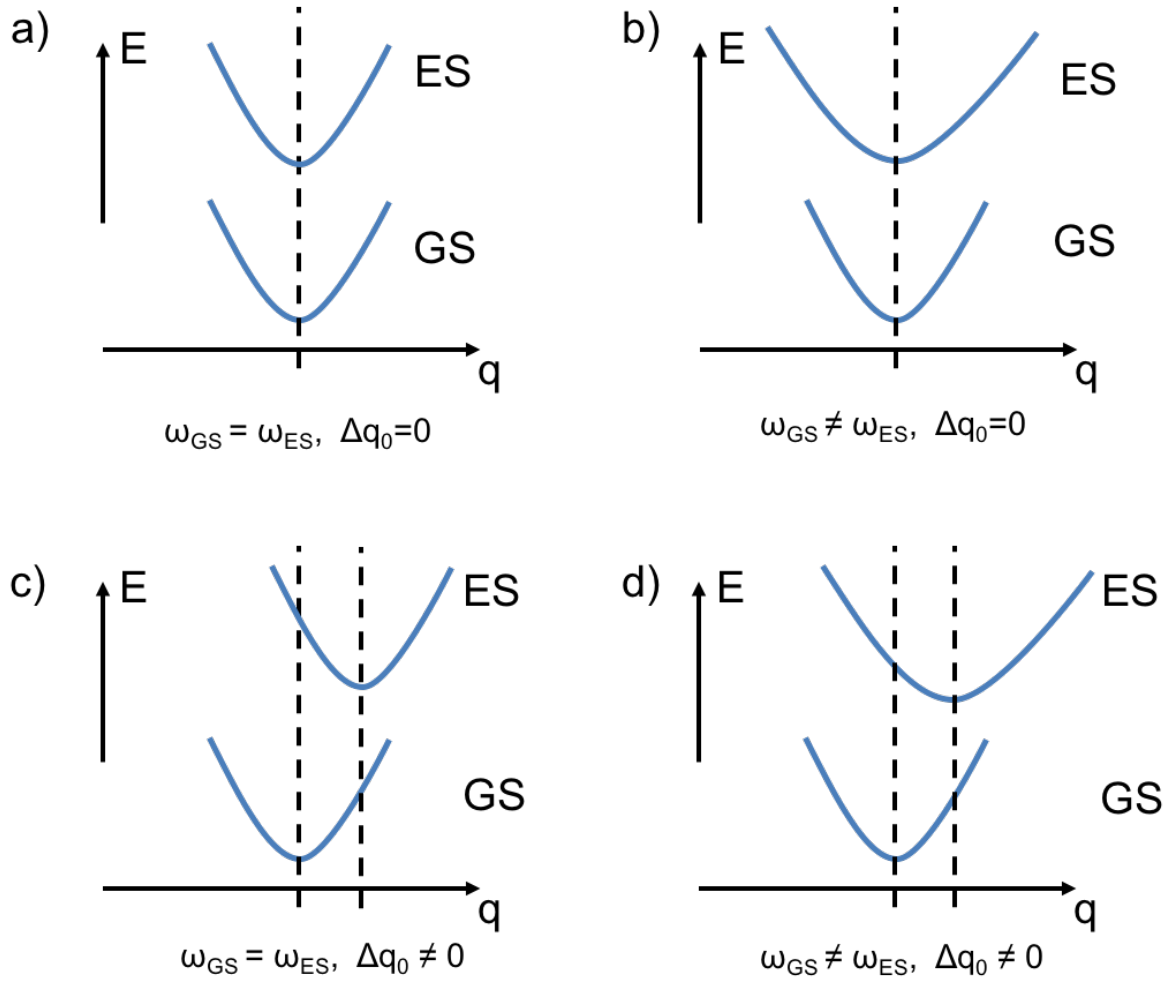

Figure 2.8: Possible potential curves for the molecular vibration in the ground and excited electronic states. All potentials are assumed to be a quadratic function of the vibrational coordinate. (a) the frequency and the equilibrium position for the potential curve does not change (b) the equilibrium position does not change but the vibrational frequency changes (c) the vibrational frequency remains constant, but the equilibrium positions shifts (d) both the frequency and the equilibrium position change in the excited state. The figure is adapted from [19].

scattering probability is proportional to the products of the dipole moment transitions $(P_i)_{e^g e^r}(P_j)_{e^r e^g}$, and the vibrational integrals $\left\langle v_k^{f(g)} \middle| v_k^{r(r)} \right\rangle \left\langle v_k^{r(r)} \middle| v_k^{i(g)} \right\rangle$.
The first condition requires the resonant transition to be dipole-allowed, for example a strong $\pi - \pi^*$ transition of the molecule. The second condition requires products of

the vibrational integrals to be non-zero. For this, either the classical frequency, or the equilibrium position of the normal coordinate for this vibration must change (fig. 2.8). Otherwise, in the harmonic case, all vibrational wave functions are orthogonal and their products will be zero, except for transitions between levels with the same quantum number. This leads to the following conculsions [18, 19]:

- vibrations, for which the normal coordinate displacements are changing during the electronic transition, can show overtones or overtone progressions in resonance Raman spectra with intensities comparable to the intensities of the fundamental frequencies (fig. 2.9).
- vibration with the greatest shift of the normal coordinate in the excited electronic state will have the strongest intensity enhancement.
- if there a conformation change following the electronic transition, then the vibration that connects the excited and the ground state geometries will be enhanced in the resonance Raman spectrum.

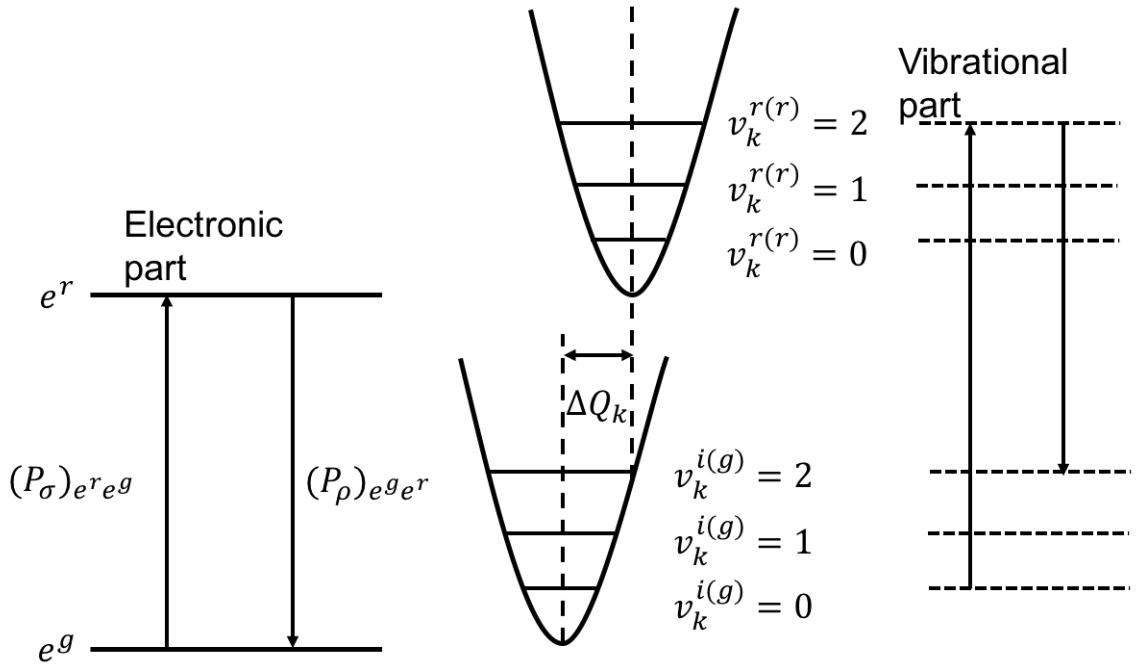

Figure 2.9: Energy scheme for the possible overtone enhancement with n=2 in the resonant Raman signal. The figure is adapted from [19].

2.3 X-ray spectroscopy techniques

X-ray spectra appear as a result of the excitation of electrons from inner shells of the atom to higher lying energy levels or continuum, or as a result of a filling of the core hole as a follow-up of the excitation process. The fact that energies of the electron orbitals uniquely represent a given chemical element or its ion, delivers a strong selectivity to X-rays. This selectivity allows to focus studies on a certain element of the periodic table and even distinguish between the same element in different chemical environments [22]. Therefore, it is possible to study processes that take place at a well-defined site of complex systems.

2.3.1 X-ray absorption spectroscopy

X-ray absorption spectroscopy (XAS) is a spectroscopy technique that is based on measuring absorption coefficient of X-rays by matter as a function of the incident photon energy [23]. The obtained absorption coefficient allows to extract information about the oxidation state and the electronic structure of the studied group of chemical elements, as well as their local geometrical environment. The attenuation of the radiation by a sample of thickness d, with the atomic mass A and density ρ can be expressed as

$$\frac{I_d}{I_0} = \exp\left(-\mu_a \frac{\rho N_A}{A} d\right) \tag{2.26}$$

where μ_a is the atomic absorption coefficient and N_a is the Avogadro number. The absorption coefficient depends on the photon energy E and the atomic number Z [23]:

$$\mu_a \propto \frac{Z^4}{E^3} \tag{2.27}$$

As can be seen, with an increase in photon energy, X-rays monotonously become more penetrating and, at the same time, absorption strongly increases for the elements with larger Z values. When the photon energy equals to the ionization energy of a certain atomic level, absorption spectrum exhibits a strong rise, called the absorption edge [23, 24]. Absorption edges are named according to the main quantum number of the electron, that is being ionized (fig. 2.10). The edge that arises from the ionization of $1s$ electron is called K-edge. When an electron with prime quantum number $n = 2$ is ionized, the L-edge is formed. L edge consists out of 3 edges L_1, L_2 and L_3. L_1 edge corresponds to the ionization of the $2s$ electron, L_2 and L_3 to the ionization of the $2p_{1/2}$ and $2p_{3/2}$ electrons, respectively. Next is the M edge, for the ionization of the electrons with $n = 3$. K and L edges are the most frequently adressed ones in XAS experiments. Less often M edges are addressed. K and L edges for most of the atomic species have the energy in the keV range, going up to hundreds of keV for heavy elements [24]. However, the absorption edge is not infinitely sharp. It has some modulation around the edge energies,

that is referred to as the *X-ray Absorption Fine Structure* (XAFS) [25,26]. XAFS reflects both the electronic state of the atom, and the coordination number with the interatomic distances from the nearest neighbors to the absorber [27]. XAFS spectrum is usually divided into two areas: *X-ray Absorption Near Edge Structure* (XANES) and *Extended X-ray Absorption Fine Structure* (EXAFS). Separation between these two is not very strict, but usually XANES is referred to as the area of ±30 eV around the edge energy and EXAFS represents the rest of the spectrum above the absorption edge [25]. Both XANES and EXAFS emerge due to the wave nature of the emitted photoelectron and the scattering of the wavepacket by the neighboring atoms [23].

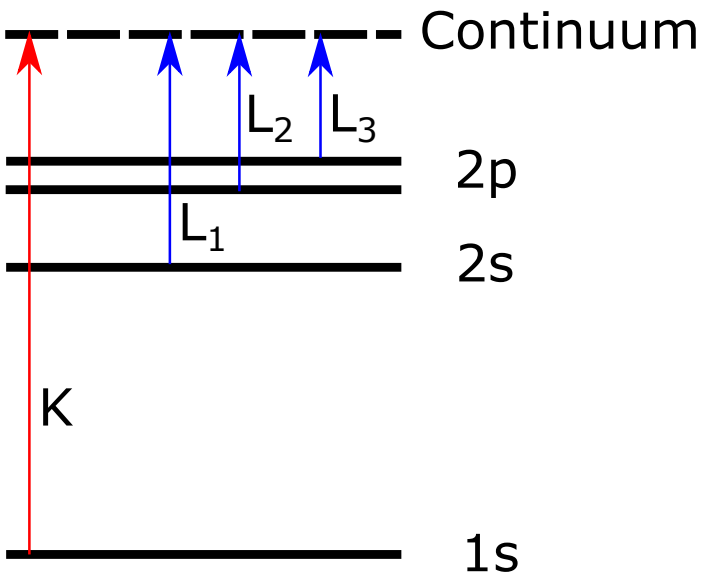

Figure 2.10: Formation of the absorption edges upon ionization of the corresponding atomic energy levels

From the quantum-mechanical point of view the absorption coefficient for the transition between the states ψ_i and ψ_f is proportional to the corresponding transition matrix element and the density of final states ρ [28]:

$$\mu = 4N_0\pi^2 l^2 \left(\frac{\omega}{c}\right) \left| \langle \psi_f | \, z \, | \psi_i \rangle \right|^2 \rho \tag{2.28}$$

where N_0 is the number of atoms in the unit volume and ω is the frequency of the incident photon.

The value of μ for a given photon frequency ω depends on the wavefunction of the final state ψ_f near the absorbing atom, where wavefunction of the initial state ψ_i is localized. Therefore, the amplitude of the matrix element $\left| \langle \psi_f | \, z \, | \psi_i \rangle \right|^2$ is defined by the wavefunction ψ_f in the region of localization of the initial state ψ_i (which coincides, for example, with $1s$ in the case of K-edge). The amplitude of the ψ_f in a certain part of a crystal or a molecule is defined by the interference of the outgoing and the backscattered

waves [28]. Consequently, these modulations in the ψ_f result in the appearance of the fine structure in the absorption spectrum: XANES and EXAFS (fig. 2.11). The kinetic energy of the photoelectron is given by the difference between the X-ray photon energy and the binding energy of the electron E_{bin}

$$T = h\omega - E_{bin} = \frac{p_e^2}{2m_e} \tag{2.29}$$

where p_e and m_e are the momentum and the mass of the electron, respectively. Knowing the momentum of the electron, its wavelength can be calculated by the *De Broigle* relation

$$\lambda_e = \frac{h}{p_e} = \frac{h}{m_e v_e} \tag{2.30}$$

Interference effects depend on the relative position of the atom, that emitted the photoelectron, and its surrounding atoms, that scatter this photoelectron (fig. 2.12). In addition, the way photoelecton wave is scattered depends also on the type of the scatterer. This allows to extract information about the nearest coordination around the absorber atom and the geometrical order from the EXAFS and XANES spectra.

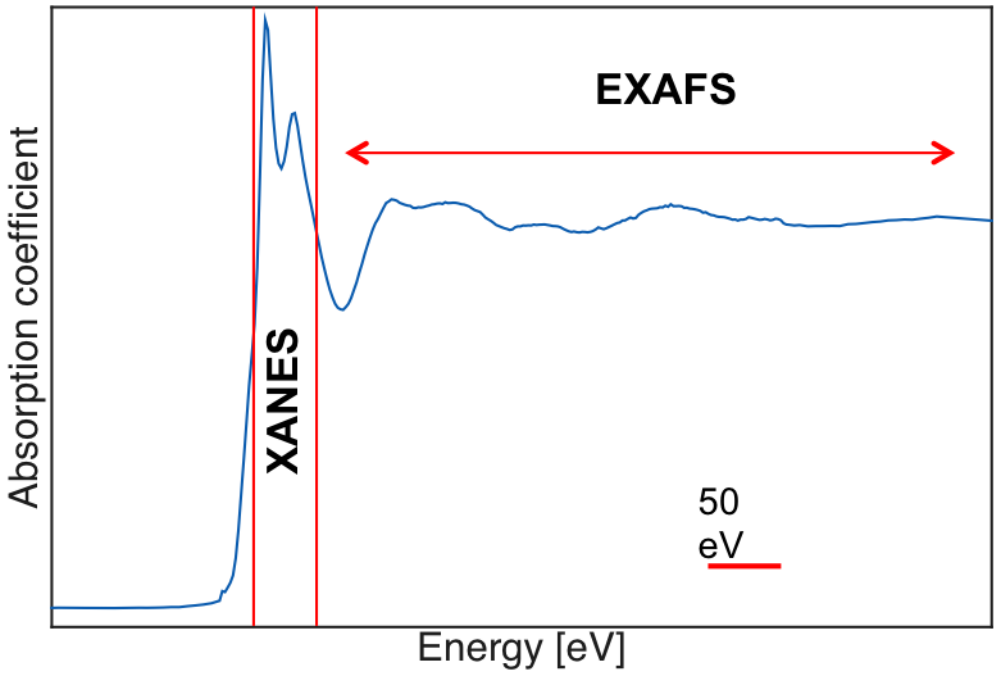

Figure 2.11: Example of the normalized XAS spectrum, measured at the K-edge of the Copper atom in a complex ligand environment. XANES region starts at the absorption edge E_0 and has a width of about 30 eV. EXAFS region corresponds to all higher photon energies.

The main difference between XANES and EXAFS is the scattering path, or the number of the scattering events, that the photoelectron experiences, before it returns to the

absorber. In the EXAFS region, photoelectron has higher kinetic energies and, therefore, shorter wavelength, which along with a shorter mean free-path implies, that single scattering (SS) events have the strongest contribution to the formation of the fine structure [28]. In the XANES region kinetic energies are low, the photoelectron can scatter off many atoms and the so called Multiple Scattering (MS) events are dominating.
The fine structure of the X-ray absorption spectrum in the EXAFS region is defined by the following expression [25]:

$$\chi(k) = \frac{\mu(k) - \mu_0(k)}{\mu_0(k) - \mu_1(k)} \tag{2.31}$$

where k is the wavevector of the photoelectron, $\mu(k)$ is the measured absorption coefficient, $\mu_1(k)$ is the absorption coefficient defined by all processes except the ionization of a given energy level. $\mu_0(k)$ is the smooth part of the absorption coefficient, what an isolated atom would have. The wavevector of the photoelectron is given by:

$$k = \Big(\frac{2m_e(h\omega - E_0)}{h^2}\Big)^{\frac{1}{2}} \tag{2.32}$$

where E_0 is the ionization potential of the given energy level.
The equation that describes the EXAFS oscillations in the Single Scattering approximation is [25, 29]:

$$\chi(k) = \frac{S_0^2}{k} \sum_i \frac{N_i e^{(-2\sigma_i^2 k^2)} e^{(-2R_j/\lambda(k))} F_j(k)}{R_j^2} \sin(2kR_j + 2\delta_c + \Phi) \tag{2.33}$$

where i represents the coordination sphere of the atoms of the same type. Other parameters in the equation are:

- number of atoms in the group N_i
- radius of the coordination sphere R_i
- Debye-Weller factor σ_i, that describes the structural disorder and the temperature dependent fluctuations of the positions of the atoms
- probability for the photoelectron to be backscattered $F_i(k)$
- phase shift of the final state on the absorber atom δ_c
- phase shift, gained by the wave, that represents the photoelectron, upon the backscattering Φ
- energy-dependent mean-free-path of the photoelectron $\lambda(k)$
- amplitude of the EXAFS modulation S_0^2

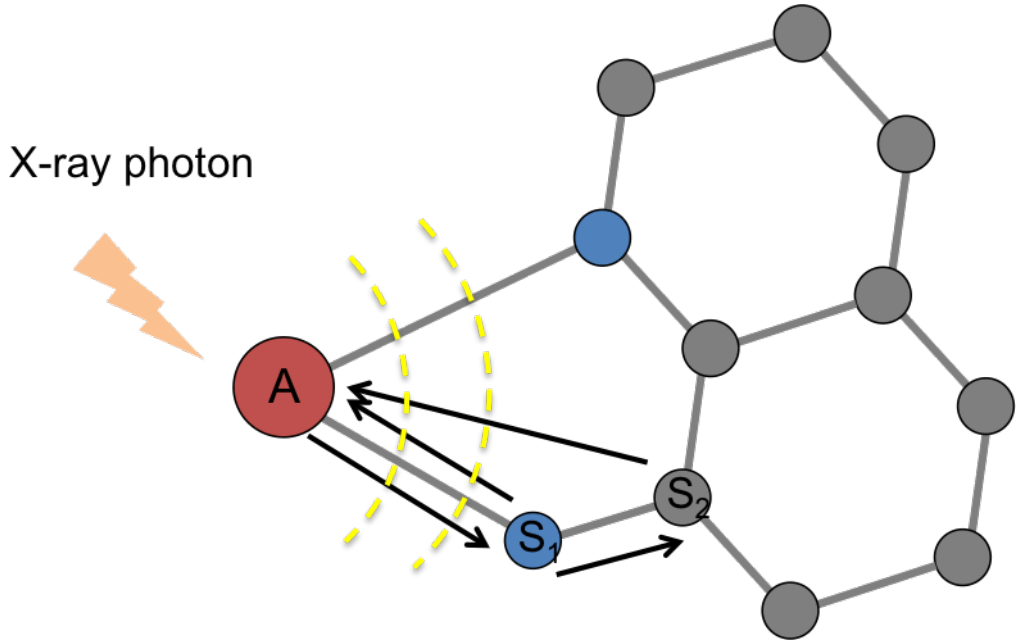

Figure 2.12: Backscattering of the photoelectron wave by the neighbouring scatterer atoms (S). The photoelectron wave is emitted when the absorber atom (A) absorbs an X-ray photon with energy above the absorption edge energy E_0. Single scattering path A-S_1-A and double scattering path A-S_1-S_2-A are shown as an example. Different colors of the atoms indicate different atoms (e.g. nitrogens and carbons).

It is convenient to analyze the EXAFS oscillations in the form of the pseudo radial distribution function $\rho(R)$, that better represents spatial distribution of the atoms around the absorber [29]. The function $\rho(R)$ is extracted from the Fourier transform of $\chi(k)$:

$$g(R) = \int_{k_{min}}^{k_{max}} \chi(k) k^n e^{-2ikR} dk \tag{2.34}$$

where, k_{min} and k_{max} define the range of the analyzed values of the wavevector k. The term k^n is included in order to compensate for a decrease in $\chi(k)$ with an increase in k, $n = 1 - 3$. $\rho(R)$ is further extracted as a power function of the Fourier-transform

$$\rho(R) = \sqrt{[Re(g(R))]^2 + [Im(g(R))]^2} \tag{2.35}$$

Apart from the information about the coordination, XANES region also contains information about the electronic structure of the studied atom. Upon increase in the oxidation state, absorption edge shifts due to different electron repulsion, and, therefore, different strength of binding of the core electrons to the nuclei. New pre-edge features can also appear in the spectrum. This happens if a vacancy in the previously fully filled shell is formed and the transitions to this empty state become possible. Transitions, that are

formally forbidden, like for example $1s \rightarrow 3d$ transition for Cu(II), become possible due to the hybridization and orbital mixing effects [1].

2.3.2 X-ray photoelectron spectroscopy

In X-ray photoelectron spectroscopy (XPS), a sample is irradiated with a monochromatic X-ray beam and the flux of the photoelectrons, emitted from the sample with a certain kinetic energy, is measured (fig. 2.13) [30, 31]. The spectrum is represented as a plot of the number of the detected electrons versus their kinetic or binding energy. The binding energy of the electron E_B, which is being ejected from a certain atomic level is given by [30]

$$E_B = h\nu - E_k - W \tag{2.36}$$

where E_k is the kinetic energy of the photoelectron, measured during the experiment, $h\nu$ is the energy of the incident X-ray photon and W is a work function of the spectrometer. The electrons, that can escape the sample without energy loss, contribute to the element-specific peaks in the XPS spectrum [30, 31]. Electrons, who lost their kinetic energy due to inelastic scattering, will contribute to the formation of the background and to the so-called $shake - up$ features [30–32]. The presence of these satellites along with the positions of the main XPS peaks, their relative intensities and width can provide an insight into the electronic configuration of the studied group of atoms [33–35].

Due to the large interaction cross-section and a small mean free-path length, only electrons from the top few tens of nanometers layer can escape the sample, which makes the technique surface sensitive [30]. Because photoelectrons can be collected and detected efficiently, weak X-ray sources are sufficient. On the other hand, it also means, that experiments have to be conducted in ultra-high vacuum, which adds extra requirements when working with liquid samples.

Like XAS, XPS can provide valuable information about the chemical state of the atomic species under study, by investigating shifts of the binding energies of the core electrons [22]. The chemical shift depends on the electron density on the absorbing atom, which makes it possible to find out which kinds of bonds this atom forms. For example, the formation of the C-O bond in a organic molecule increases the binding energy of the $1s$ electron of carbon by 1.6 eV, compared to the methylene carbon. Bonds C=O or O-C-O result in an almost doubled value of the chemical shift of 2.9 eV [30]. In general, blueshift of a XPS peak is proportional to the number of bonds with more electronegative atoms. This is illustrated by the CF, CF_2 and CF_3 series with the chemical shifts of 2.9 eV, 5.9 eV and 7.7 eV, correspondingly [30]. However, XPS probes mostly the ground electronic state of the atom, because the final state is in the continuum. Some information about the valence electrons can be extracted from the satellites of the main XPS peaks, or the multiplet splitting, which can occur if there are unpaired electrons in

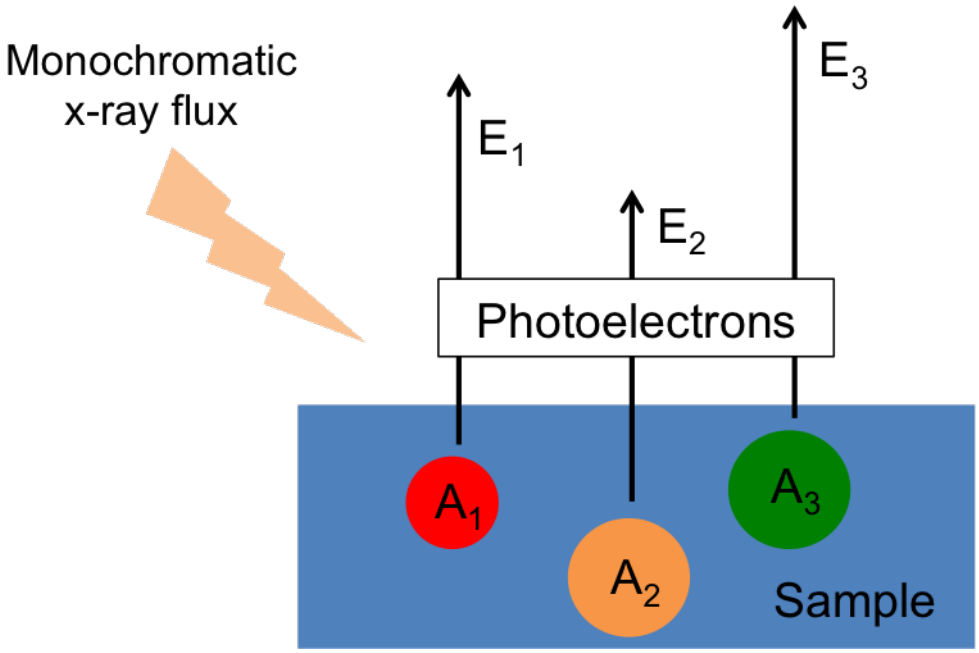

Figure 2.13: Emission of the photoelectrons from the studied sample under illumination with the monochromatic X-rays in the XPS experiment. The kinetic energy of each photoelectron uniquely characterizes the atom, from which it was emitted.

the valence band [36, 37]. Chemical shifts that correspond to the formation of chemical bonds by other chemical elements with each other are usually lower, than those for the CO or CF series and are ranging from a fraction of electron volt up to several electron volts. Along with the linewidth of the incident beam on the order of 0.6 eV - 0.9 eV, this means that physically meaningful data processing is needed in order to deconvolute spectra and obtain maximum information, especially if many atoms of the same kind in different chemical environments are present in the sample [38]. The number of peaks, their relative intensities and linewidths in the mathematical model used for the fitting must reflect stoichiometry of the sample.
There are different kinds of peaks that can be observed in the XPS spectrum, that emerge due to different physical processes [30, 31]:

- Photoelectron peaks. They are formed by the photoelectrons, that escaped the sample without energy loss. They contain information about the ground state of the atom and its chemical environment.

- Auger peaks. Auger peaks emerge due to Auger ionization process. These peaks remain constant in kinetic energy plot independent of the energy of the incident photon.

- Shake-up lines. Shake-up satellites occur when the outgoing photoelectron is inter-

acting with the valence band electron and promotes it to a higher lying level. The difference in energies between the main XPS peak and the satellite gives the energy of the valence excitation. Shake-up satellites are mostly common for the transitions from the $2p$ states or $\pi \rightarrow \pi*$ transition in molecules.

- Multiplet splitting. Multiplet splitting is a final-state effect and can occur if an atom has a non-zero spin in the ground state (unpaired electrons in the valence band). In this case, core hole can be formed with different spin orientations and corresponding splitting of the main peak is observed. Multiplet splitting can also occur for the transitions from p levels, resulting in either assymetry of the lines, or the change in the separation of the $2p_{1/2}$ and $2p_{3/2}$ lines.

Apart from the chemical state information, XPS can be used to determine element composition of the sample. The area under each peak in the spectrum is given by:

$$I = nS(E) \tag{2.37}$$

where n is the concentration of the atoms in a unit volume, and the factor $S(E)$:

$$S(E) = f\sigma\lambda K \tag{2.38}$$

includes the incident X-ray flux f, the photoionization cross-section σ, the electron attenuation length λ and the spectrometer efficiency K. The general expression for the atomic percentage of any constituent requires the peak areas and the sensitivity factors for all peaks in the spectrum [31]:

$$C_x = \frac{n_x}{\sum n_i} = \frac{I_x/S_x}{\sum I_i/S_i} \tag{2.39}$$

or, when concentrations of two components are compared:

$$\frac{n_1}{n_2} = \frac{I_1/S_1}{I_2/S_2} \tag{2.40}$$

If shake-up satelites are present, then for more accurate results their peak areas also have to be included. In that case, if the studied sample contains, for example, Cu(II) and Cu(I) or Cu(0) and their relative fraction has to be estimated, shake-up satelites can be used [31]. First, main peak/shake-up peak area ratio R has to be determined from a pure Cu(II) sample. Then, Cu(I):Cu(II) ratio can be calculated for the unknown sample

$$C_{Cu(I)} = \frac{A - RB}{A + B} \tag{2.41}$$

where A and B are the total main peak and the shake-up areas, respectively.

2.3.3 VUV Raman spectroscopy

Vacuum Ultraviolet (VUV) Raman spectroscopy is a powerful spectroscopic tool that can be utilized to study different types of elementary excitations in, for example, strongly correlated systems like manganites or cuprates, or charge transfer processes in bio-inorganic molecules with metal centers [39, 40]. VUV Raman is a photon-in photon-out process in which the change in energy and momentum of the incident photon during the scattering process is investigated. The technique is element and orbital specific when it is in resonance with an atomic absorption edge by inducing specific orbital transitions of the element of interest. At the same time, such a tuning of the incident energy may result in a great enhancement of the scattering cross-section due to resonant nature of the scattering process [41]. Unlike conventional Raman scattering, VUV Raman allows to study elementary excitations as a function of the momentum transfer. For instance, at a photon energy of Cu M_1 edge of 122 eV, and a lattice constant of 6 Å, maximum momentum transfer relative to the size of Brillouin zone would be:

$$\frac{\Delta k_{ph,max}}{k_{Brillouin}} = \frac{2E_{ph}a}{hc} * 100\% \approx 12\% \tag{2.42}$$

where E_{ph} is the photon energy and a is the lattice constant. Orbital and element selectivity arises from the fact, that the photon energy can be tuned to a certain absorption edge of a chemical element. This allows not only to confine studies to one specific type of atoms in the complex system, but also allows to probe electronic structure by selecting different absorption edges of the same element. For example, it was shown in recent studies of the superconducting spin-ladder copper compounds [40], that different electronic and spin excitations can be triggered by tuning the incident photon energy to either M_1 (Cu $3s \rightarrow 4p$) or M_3 (Cu $3p \rightarrow 3d$) edges of Cu. While at the M_1 edge, the excitations were of phonon nature, excitation at the M_3 edge yields one and two magnon spectra, due to the hybridization of the Cu and O orbitals and the corresponding electron hopping with a spin-flip from Cu to O.

The momentum dependence implies, that the nature and the symmetry of the elementary excitation can be studied through polarization analysis. Like the *Resonant Inelastic X-ray Scattering* (RIXS), VUV Raman is a two-step process and the first part of it is naturally related to XAS [39]. Therefore, it is crucial to measure the absorption spectra in the soft X-ray regime before measuring VUV Raman, in order to know the exact edge energies for the compound of interest. The second step of the VUV Raman process can be related to X-ray emission spectroscopy with a clause, that the incident photon energy is tuned to a resonance and does not promote an electron to continuum.

The microscopic picture of the scattering process consists of two possible cases: direct and indirect one (fig. 2.14) [39]. In the direct process, the electron is promoted to an empty state in the valence band, and another electron is subsequently decaying to fill

the core hole. The net result of such process is defined by the energy and momentum conservation laws:

$$\begin{cases} \omega_s = \omega_i - \omega' \\ k_s = k_i - k' \end{cases} \tag{2.43}$$

where ω_i, ω_s, k_i, k_s are correspondingly the frequencies of the incident and scattered photon, and ω' and k' are the frequency and the wavevector of the electron-hole excitation left in the system.

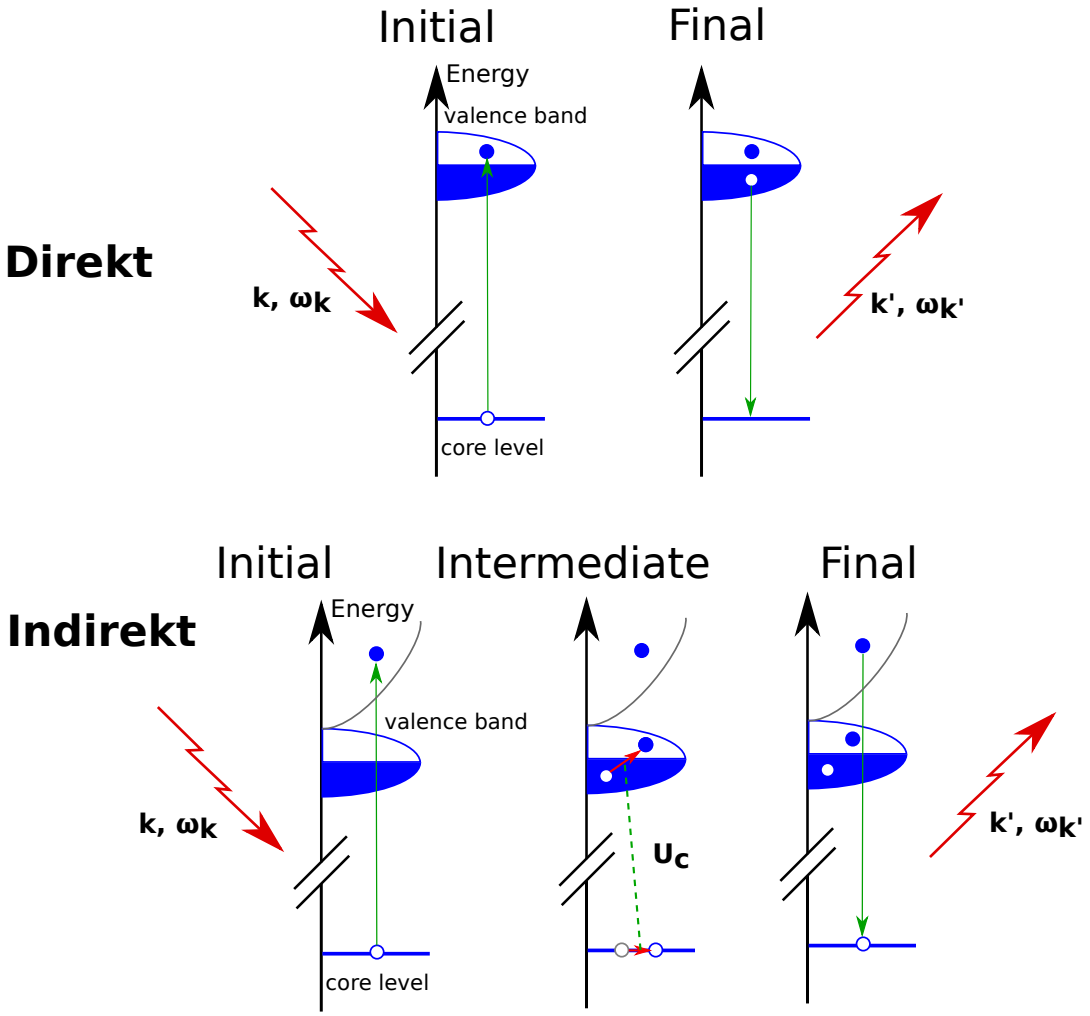

Figure 2.14: Schematic representation of the direct and indirect processes of the inelastic scattering of X-rays. The figure is adapted from [39].

In order for the direct scattering channel to be dominating, both absorption and emission transitions must be allowed. If one of these transitions appears to be weak or forbidden, then the indirect channel is dominating. The microscopic picture of the indirect process resembles that for the shake-up excitations in XPS. The inelastic scattering appears due to interaction of the intermediate state core-hole exciton with the valence electrons. When an electron is promoted to a higher lying energy level and a core hole is left behind,

electrons from the valence band tend to screen it. This can lead to the formation of an exciton, that is left in the system after the radiative decay of the initially excited electron.

Chapter 3

Experimental techniques

This chapter provides the information on the experimental techniques and setups, used to perform the research on bio-inorganic transition metal complexes. First section highlights the equipment, used to perform optical Raman scattering experiments. Second and third ones focus on the instrumentation at the large-scale facilities PETRA III and FLASH. The fourth section gives the information about the equipment, used to collect the XPS data.

3.1 Optical Raman spectroscopy

The measurements of the inelastic light scattering in the UV-Near Infrared wavelengths range were performed in the Optics laboratory in the Center for Free-Electron Laser science. A general overview of the experimental setup for the inelastic light scattering experiments is shown in fig. 3.1. As a light source, two mode-locked Tsunami laser systems from Spectra Physics, equipped with frequency doubling/tripling units are used. They are capable of providing emission wavelength in the range 240 nm (3ω) – 1060 nm (fundamental) [42]. A small fraction of the output of each laser is coupled into a autocorrelation unit, in order to measure the pulse duration. The laser light is further coupled to a spatial filter and then focused on the sample. The spatial filter consists of two lenses and a pinhole in the point, where foci of both lenses overlap. It allows to cut unwanted spatial frequencies and expand the laser beam in order to achieve the smallest possible focus spot on the sample. The pinhole sizes used in the experiments are 25 µm, 50 µm and 100 µm, depending on the type of measurement. The focal distances of lenses are 20 mm and 150 mm. Both lenses and the pinhole are mounted on independent XYZ translation stages in order to align the beam parallel to the optical axis of the entrance objective of the Raman spectrometer. After the spatial filter, the light is incident on the two flat mirrors guiding it to the first on-axis parabolic mirror of the entrance objective, that was used for both focusing and collecting light from the sample. The collected light

was analysed by a custom designed McPherson UT-3 Raman spectrometer with a liquid nitrogen cooled CCD camera [43]. The ratio of the focal distance of the first parabolic mirror $F_{parabola}$ to the focal distance of the second lens of the spatial filter F_{lens} gives the magnification ratio with which the pinhole of the spatial filter is reimaged on the sample:

$$k = \frac{F_{parabola}}{F_{lens}} = \frac{25}{15} \approx 1.67 \tag{3.1}$$

This ratio allows to estimate the size of the focal spot on the sample and the incident power density.

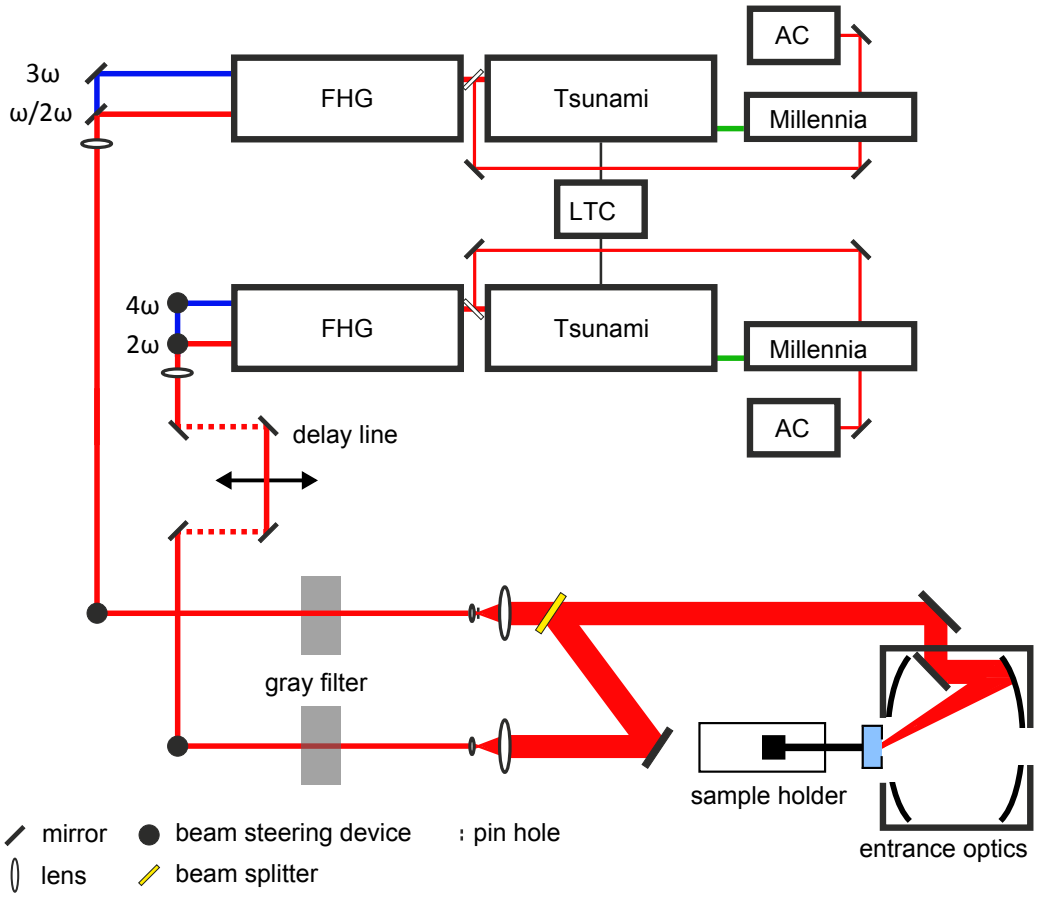

Figure 3.1: Optical scheme of coupling the light from the Tsunami laser to the sample. The shown scheme can be used for pump-probe experiments. Radiation from the Tsunami laser can optionally be doubled/tripled in frequency and afterwards attenuated to the desired power level. After the attenuation by a gray filter, a telescope with an intermediate pinhole expands the beam and then both beams are mixed by a beamsplitter and directed onto the mirror of the entrance objective, that focuses the light on the sample. The figure is taken from [44].

For the pump-probe measurements either a pair formed out of $\omega/2\omega/3\omega$ beams of one

laser, or a combination of the outputs of both Tsunamis can be used. In the second case, lock-to-clock unit must be used to synchronize the repetition rates of both lasers. The delay between the pump and the probe laser pulses is controlled by a motorized delay line unit. The calibration of the delay is performed by measuring the difference between the arrival times of both pulses at the sample position. For this purpose, a custom UPD-30 avalanche photodiode from ALPHALAS is used. The plot of the delay between pulses as a function of the delay line position is fitted with a line function. The slope of the line fit, that must be equal to twice the speed of light, can be used as a criterion of the validity of the calibration.

3.1.1 Tsunami laser system

Tsunami from Spectra physics is a pulsed solid state laser, based on a Titanium-doped sapphire crystal [42]. The emission wavelength can be tuned within 690-1080 nm. This wavelength range is spilt into 5 overlapping regions in order to achieve a stable performance with a high output. These regions are:

- *Standard*: 720-850 nm
- *Long*: 840-1000 nm
- *Extra*: long: 970-1080 nm
- *Blue*: 690-790 nm
- *Mid-range*: 780-900 nm

For each of these regions corresponding set of mirrors is provided. The lasers in the optics lab are equipped with the *Standard* and *Long* mirror sets, allowing asymmetric operation and broad range of wavelengths achievable without a need to exchange the mirror sets. Typical output power is within the range from 1.3 W to 1.7 W, depending on the emission wavelength. The pulse duration is 2-4 ps [42]. This provides good compromise between the time resolution and the spectral width of the pulse. Because of the high absorption of the active medium in the blue and green, pumping is performed by the green CW diode laser running at 532 nm.
The repetition rate of the laser is defined by the optical length of the cavity, for Tsunami laser system it equals to 80 MHz. Active mode-locking is performed by the acousto-optical modulator (AOM). AOM is controlled by a feedback signal from the fast photoiode, located inside the cavity and modulates losses inside the cavity with half the repetition rate frequency. For the *ps* option of the Tsunami laser, group velocity dispersion compensation is performed by a Gires-Tournois Interferometer (GTI), that is similar to a Fabri-Perot Interferometer apart from the fact that one side of GTI has reflectivity close

Table 3.1: Available wavelengths for the fundamental (ω) and its second (2ω) and the third (3ω) harmonics for each Tsunami laser.

Frequency	Tsunami1	Tsunami2
ω	720-850 nm	840-1000 nm
2 ω	360-425 nm	420-500 nm
3 ω	240-283 nm	280-330 nm

to 1. The GTI is installed instead of the high reflector in the cavity and can provide a large and linear negative group velocity dispersion in a narrow wavelength range. The wavelength selection of the Tsunami is done with a birefringent filter. This filter changes the linear polarization of the incident light to elliptical, and only for a certain wavelength there is a 180° phase shift, and the wave will preserve its linear polarization and will not suffer additional losses in the cavity upon reflections from the Brewster surfaces.
In order to synchronize both Tsunami lasers for the pump-probe experiments, one of the lasers is equipped with a piezo-electric mirror that is controlled by the lock-to-clock unit and is used to adjust the repetition rate of the *slave* laser to the frequency of the *master*. Lock-to-clock allows to get repetition rates of both lasers to be equal with a precision of about 100 Hz.
Each laser is followed by a harmonic generation unit, that allows to generate 2ω beam by doubling the fundamental frequency, or 3ω by mixing the fundamental and the frequency doubled beams [45]. Typical output of the 2ω beam is up to 200 mW, and up to 100 mW for 3ω.

3.1.2 UT3 Spectrometer

Light, scattered from the sample, is collected and analyzed by a custom produced fully reflective Raman spectrometer with a Cassegrain-type entrance objective [43]. The design of the spectrometer and the entrance objective utilizes on and off-axis parabolic mirrors, as well as spherical and elliptical ones, in order to ensure aberration-free imaging on the optical axis with high stray-light rejection and signal to noise ratio (fig. 3.2).
The entrance objective consists of four on-axis parabolic mirrors, with a total magnification of 5.8. The M1 mirror collects and collimates the scattered light and directs it onto the mirror M2. M2 creates the intermediate focus and illuminates mirror M3, that collimates the light and creates a section for installation of the analyser crystal. Mirror M4 further focuses light onto the entrance slit of the spectrometer. The focusing of light on the sample is performed by the M1 mirror, that ensures wavelength-independent focus

position. Direct reflection from the sample is blocked with a beam block.
The UT3 Raman spectrometer consists of the premonochromator and the spectrograph stage. The premonochromator is formed by the Mono1, the relay stage and the Mono2. Mono1 disperses the light onto the slit plane of the relay stage, which is then further re-imaged onto its exit slit. After relay stage, dispersed light is collapsed by the Mono2 into one beam, focused on the entrance slit of the Mono3. Mono2 is a mirrored copy of the Mono1 and is subtractively coupled to it. Such a geometry implies that the premonochromator acts like a bandpass filter, that efficiently cuts all wavelengths, except those in the region of interest. Both the Mono1 and the Mono2 as well as the relay stage use off-axis parabolic mirrors to create the aberration-free focus spots, which along with the relay stage offers strong rejection of the stray light. Mono3 consists of one elliptical, one spherical mirror and a diffraction grating. The elliptical mirror focuses the light after the diffraction grating on the liquid Nitrogen cooled CCD chip.
The spectrometer is equipped with revolving grating mounts and can operate in the wavelength range 165-1000 nm. Depending on the wavelength range either a set of visible or UV gratings must be used.

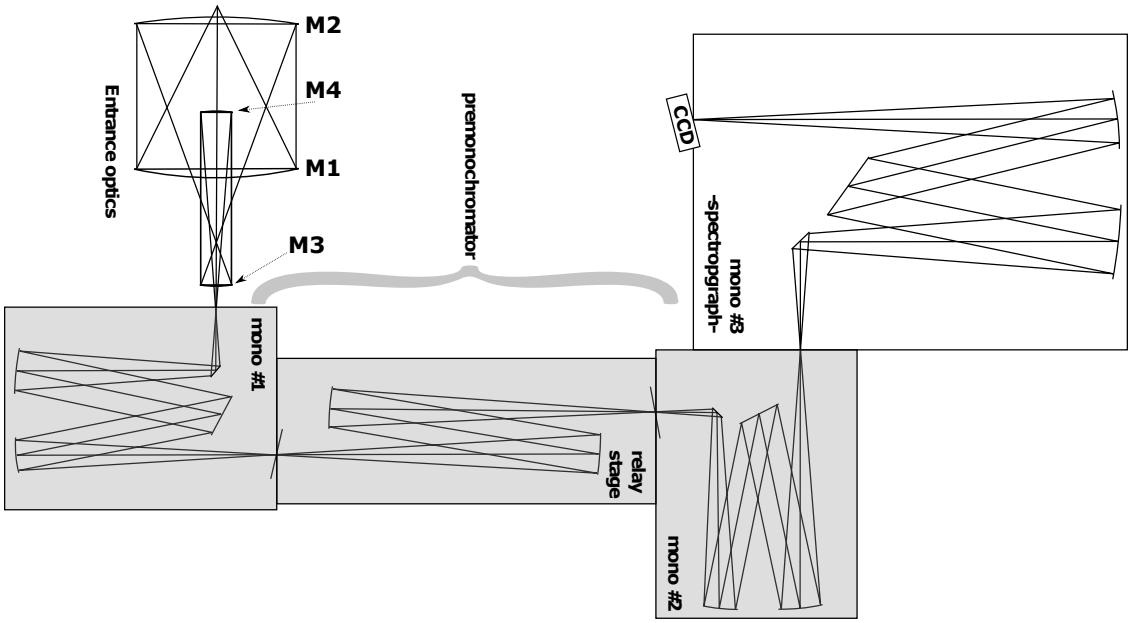

Figure 3.2: Optical scheme of the UT-3 triple stage Raman spectrometer together with the entrance optics. The first and the second monochromator together with the relay stage can be used either in subtractive or additive mode. In the subtractive mode they act like a premonochromator for the Mono3, effectively cutting the desired energy range from the spectrum of light, emitted from the sample. Mono 3 always acts as a spectrograph stage. The figure is taken from [43].

3.1.3 Calibration

The calibration of the spectrometer is performed in two steps. Because of the bandpass-like action of the premonochromator, the entire working range of the spectrometer is split into a continuous set of regions, called windows, and it is important that both monochromators are fully subtractively coupled in each window. In order to make sure that this is the case, the central wavelength of the window is coarsely defined by observing that the scattered laser beam is passing through all spectrometer stages. Afterwards, with the help of a whitelight source with a continuous emission spectrum, positions of the gratings in Mono1 and Mono2 are optimized until almost flat distribution of intensity on the CCD chip for the current window is obtained. This means that all wavelength within the window are transmitted with the same transmission coefficient. After the window has been defined, gratings in Mono1 and Mono2 are rotated for the same angle and this change is followed by the grating in the Mono3. In this way a continuous set of windows for all operation wavelengths is defined.
A precise calibration of the CCD pixel versus wavelength is performed with the help of He, Ne, Xe and crypton high-precision calibration lamps. The dispersion of the spectrometer within each window is fitted with a linear function:

$$\lambda = a * px + b \tag{3.2}$$

where, px is the pixel position on the CCD chip, λ is the actual photon wavelength in nanometers and a, b are the fitting coefficients.
In order to get the real cross-section values for a certain Raman mode as a function of the excitation wavelength, the spectral sensitivity of the spectrometer has to be measured. The readout of each pixel of the spectrometer is related to the real intensity values of the emitted light through the following relation:

$$I_{measured}(\lambda) = I_{\lambda}^{real}(\lambda) S(\lambda) \Delta\lambda(\lambda) \tag{3.3}$$

where, λ is a central wavelength of the given pixel, I_{λ}^{real} are the real values of the intensity of the emitted light, $S(\lambda)$ is a wavelength and polarization-dependent sensitivity factor that reflects response of the spectrometer to photons of a given energy and $\Delta\lambda$ is the spectral width of the pixel. The sensitivity factor $S(\lambda)$ was extracted by measuring the spectra of the broadband whitelight source with the calibrated emission spectrum. This yields the final formula for the normalization of the Raman spectra:

$$I_{\lambda}^{real}(\lambda) = \frac{I_{measured}(\lambda) I_{\lambda,\, lamp}^{real}(\lambda)}{I_{measured,\, lamp}(\lambda)} \tag{3.4}$$

with $I_{\lambda,\, lamp}^{real}(\lambda)$ being a spectral density of the light emitted from the calibration source and $I_{measured,\, lamp}(\lambda)$ being the measured values of the intensity of the calibration source

by the spectrometer. If spectral density in frequency coordinates is needed, then the following relation has to be used:

$$I_\nu(\nu)d\nu = I_\lambda(\lambda)d\lambda \tag{3.5}$$

3.2 VUV Raman spectroscopy

Experiments on the inelastic scattering of light were performed at the VUV Raman spectrometer, permanently installed at the PG1 beamline of the Vacuum Ultraviolet Free-Electron laser FLASH in Hamburg, Germany. This section describes basic operation principle of FLASH, the optical layout and the capabilities of the PG1 beamline and the VUV Raman spectrometer.

3.2.1 Free-Electron laser FLASH

FLASH is a high gain, single pass free electron laser with superconducting cavities. It is capable of producing ultrashort (10-50 fs) pulses with a fundamental wavelength ranging from 6.9 to 47 nm and a peak brilliance up to 10^{30} photons/s/mrad^2/mm^2/0.1%BW at a 10 Hz repetition rate of a pulse burst [46]. FLASH facility has been recently upgraded, and now FLASH-2 experimental hall is available for user experiments. Both FLASH-1 and FLASH-2 share the same accelerator part, but FLASH-2 has its own variable gap undulator, that allows for easier tuning of the energy of the VUV photons. The schematic layout of FLASH-1 is shown in fig. 3.3. Electron bunches are generated when a femtosecond laser pulse from a seeding laser hits the target. The electrons are further accelerated to relativistic speed in a linear superconducting accelerator. At certain stages of the accelerator bunches are being longitudinally compressed to reach the peak current needed for FEL operation. After leaving the accelerator, electrons enter the undulator, that is a sequence of dipole magnets with alternating polarities, that force electron bunch to travel in a sine curve. During this motion electrons emit synchrotron radiation, that travels faster than the electron bunch and modulates charge density in it. This leads to a formation of micro-bunches within one bunch and to an exponential increase in the intensity of the emitted photons and their coherence. This process starts from shot noise and takes place on a single pass through the undulator. It is called a *Self-Amplified Spontaneous Emission* (SASE) [47, 48]. After the undulator, electrons are directed to a electron beam dump by the special magnets. The VUV radiation travels further to the beamlines.

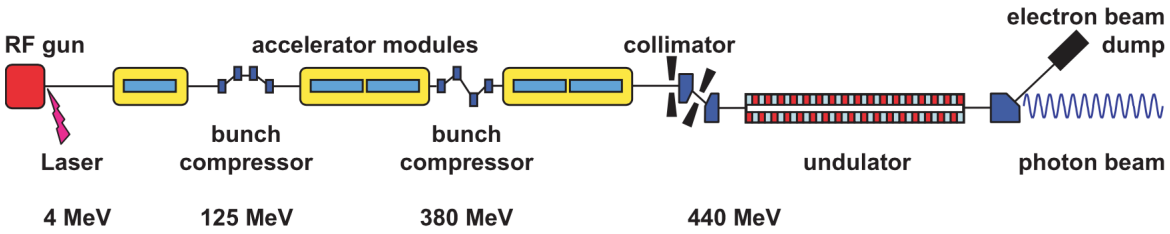

Figure 3.3: Schematic view of the free-electron laser FLASH. The figure is taken from [49].

3.2.2 PG1 beamline

Experiments on the inelastic light scattering put high demands on the bandwidth of the excitation radiation, since the spectrum of the inelasticly scattered light is convoluted with the spectrum of the excitation pulse, which can limit the spectral resolution. A typical bandwidth of FLASH is 0.5-1% of the central photon energy [46]. At Cu M_3 edge this results in a bandwidth of the emitted radiation of 730 meV - far above theoretical resolution of the VUV Raman spectrometer at this energy of 4 meV. On the other hand, slitless spectrometer design means, that the resolution can be limited by the source size, which in our case is the size of the FEL focus spot on the sample. Both these requirements: narrow bandwidth of the incident radiation and the small focus size, are fulfilled by the plane grating monochromator (PG) beamline. An overview of the beamline is shown in fig. 3.4.

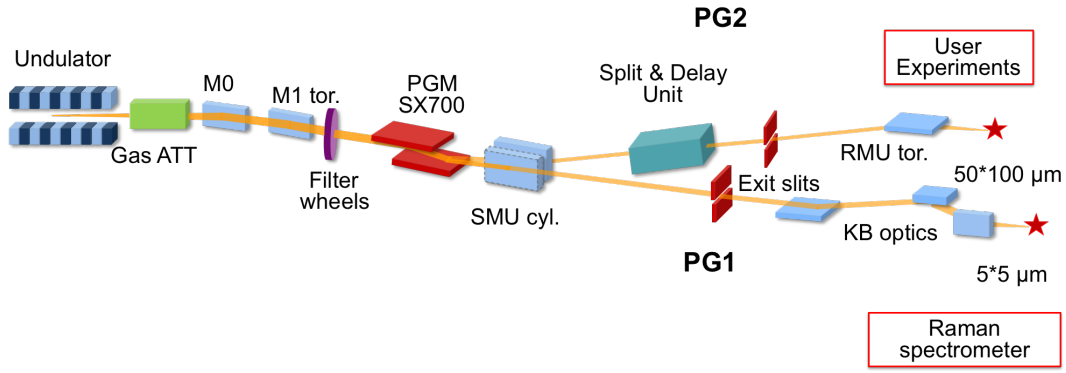

Figure 3.4: Schematic view of the PG beamline of the free-electron laser FLASH. The VUV Raman spectrometer is installed as a permanent end-station at the PG1 branch. The figure is taken from [50].

After leaving the undulator, VUV radiation passes through the gas attenuator and is then deflected by a plane mirror M0. The toroidal mirror M1 collimates the light vertically and focuses it horizontally. The light is dispersed by a plane grating monochromator and refocused by a cylindrical SMU mirror onto the plane of the exit slit. The width

of the slit defines the range of energies of the FEL beam that will pass trough. The plane mirror M6 directs the FEL beam onto a Kirpatric-Baez (KB) pair of focusing mirrors, that create a microfocus inside the experimental chamber of the size of 5x10 μm [50].

3.2.3 VUV Raman spectrometer

The high-resolution double stage VUV Raman spectrometer is a permanent end-station of the PG1 branch of the plane grating monochromator beamline at FLASH [46, 50, 51]. This instrument has been developed at the University of Hamburg in collaboration with DESY for inelastic scattering (Raman) experiments in the soft X-ray spectral region from 20 to 200 eV. The instrument is intended to provide an unprecedented spectral resolution of 2-15 meV and superior stray light suppression, which allows studies of low energy quasiparticles in various solid samples. The spectrometer design is based on a confocal additive arrangement of two high-resolution monochromator stages, shown in fig. 3.5 [40, 52]. In brief, the sample is located in the sample chamber and emits under illumination with the FEL radiation elastically and inelastically scattered photons. Both types of photons are collected by the first monochromator stage. This stage acts also effectively as an entrance objective that collects a relatively large solid angle and reduces the stray-light by several orders of magnitude by predispersing the light and separating the elastic and inelastic contributions. A slit mechanism situated between the monochromators allows only photons into the second stage that are inelastically scattered. The second stage is the spectrograph stage that disperses the light further onto the detector plane, where the spectrum is recorded by an intensified charged coupled camera (ICCD). Each monochromator chamber, shown in fig. 3.5 as SP1 and SP2 houses two off-axis parabolic mirrors for light collimation and focusing and a grating bench that can hold up to 4 optical gratings.The schematic layout of the monochromator is depicted in fig. 3.5.

The sample S is located in the focal point of the first off-axis parabolic (OAP) mirror M1. The scattered light is collimated and directed onto the grating unit G1. Note, that in both monochromator stages the parabolic mirrors deflect the beam perpendicular to the dispersion plane. Thus, the light is focused along the short axis of the parabola (sagittal focusing). This reduces the influence of optic slope errors. The maximum acceptance angle of M1 is 37 x 82.6 mrad (v x h). G1 works in inside order orientation. The vertically dispersed photons are collected and focused onto the intermediate slit (labelled “MS” in fig. 3.5.) by the second OAP mirror M2. As said before, the light transmitted through the intermediate slit is then collected and further dispersed by the second monochromator stage in a similar fashion. The Raman spectrometer works with a constant included angle of 162°, thus the mirror positions are fixed, only the gratings have to be rotated in order

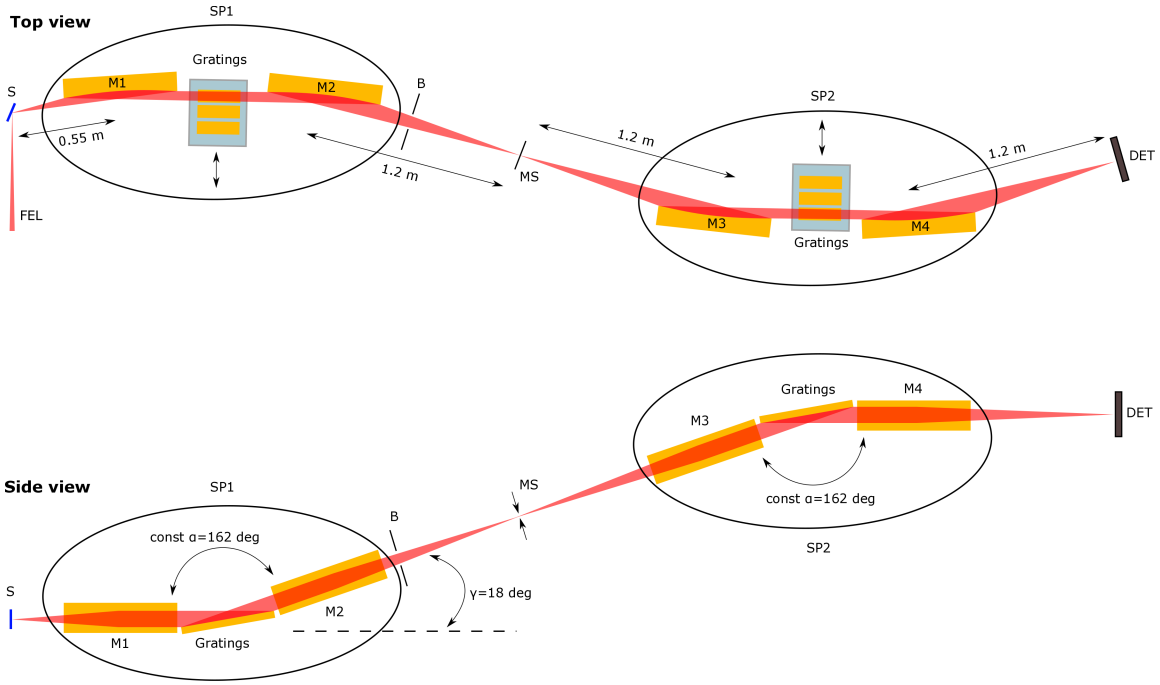

Figure 3.5: Optical scheme of the VUV Raman spectrometer. M1-M4 off-axis parabolic mirrors, MS middle slit, B baffle system, S sample, DET detector camera. SP1, SP2 monochromator chambers.

to choose or scan the wavelength. By using the gratings in zeroth order, any wavelength can be focused. This property is used in the alignment process of the instrument. The grating unit of the first monochromator stage hosts two diffraction gratings: G1-3 and G1-4 with a groove density of 576 lines/mm and 1120 lines/mm, covering the spectral energy range of 35-210 eV,correspondingly. Gratings are switched between each other by moving them transversely to the beam in horizontal plane (see fig. 3.5). In addition, a plane mirror is installed and can be used instead of the diffraction grating in case a higher throughput is needed.

3.3 X-ray absorption spectroscopy

Pump-probe experiments on X-ray absorption spectroscopy were performed at the P11 beamline of the PETRA III (Positron Electron Tandem Ring Accelerator) third generation synchrotron light source in Hamburg, Germany. PETRA was built in 1976 as an electron-positron collider. Later on it served as a pre-accelerator for the HERA collider project. In 2007 PETRA was rebuilt and became worlds most brilliant light source in its photon energy range.

3.3.1 PETRA III synchrotron source

PETRA III is a ring accelerator, which means that charged particles (electrons) circulate inside the ring on a closed orbit. This closed orbit is formed by straight parts and bending magnets between them, that force the electrons to change the direction of their movement to enter the next straight part. A schematic view of the PETRA III synchrotron is presented in fig. 3.6. Creation of a bunch takes place in the electron gun, after which electrons enter the linear accelerator (LINAC). Inside LINAC electrons are accelerated to a kinetic energy of several hundreds of MeV and are afterwards injected into the booster ring. Inside the booster ring their energy is further increased to $\sim$ GeV level and they can be injected into the main PETRA storage ring, where, depending on the operation mode of the synchrotron, they circulate up to 8 hours [53].

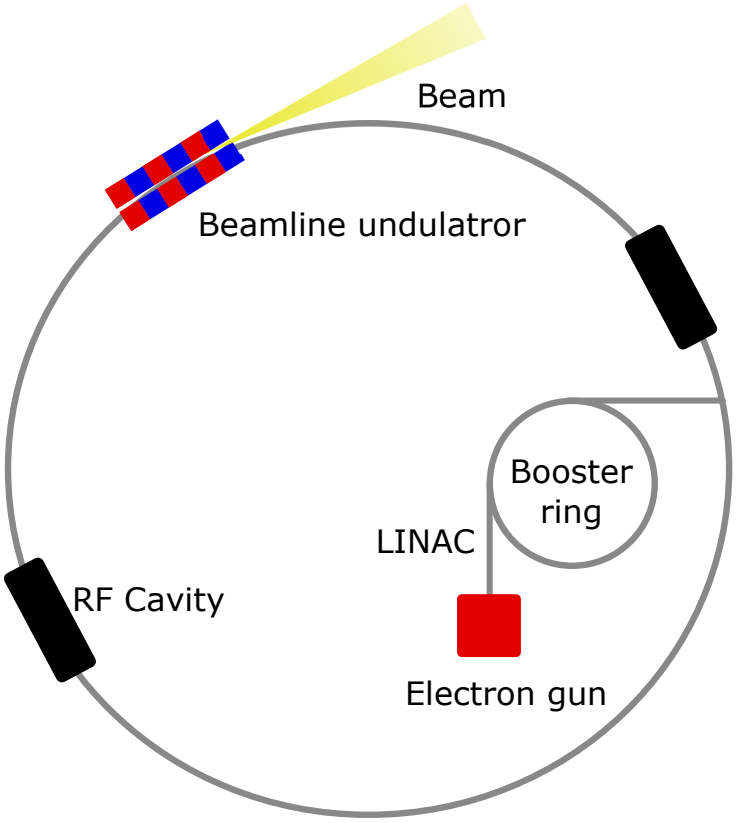

Figure 3.6: Scheme of the PETRA III third-generation synchrotron. Electron bunches are generated by the electron gun and preaccelerated by the LINAC and the booster ring. Synchrotron radiation is generated when the electron bunch passes through the undulator section.

Each time when the electrons inside the storage ring move with acceleration, the synchrotron radiation (SR) is emitted. Depending on the character of the electrons acceleration and its trajectory, different characteristics of the SR can be obtained, and this is utilized in the so-called insertion devices (ID). In first generation of synchrotrons, there

were no insertion devices, and the SR was emitted when electrons were forced to change their trajectory due to bend magnets. The spectrum of this radiation was broad and the radiation was emitted in a fairly large solid angle in the plane of the ring, with a vertical divergence on the order of $m_e c^2/E$, where m_e is the mass of the electron, c is the speed of light and E is the kinetic energy of the electron. This was considered as a rather parasitic effect. In second and third generation of synchrotrons, they started to be used as a source of X-rays, and insertion devices were incorporated into the storage rings. There are two types of insertion devices: wiggler and undulator. Both of them consist of pairs of magnets with alternating polarities, stacked after each other with a gap between them. When an electron travels inside the undulator, alternating magnetic field forces it to travel in a sine curve, therefore emitting X-ray photons. The difference between a wiggler and an undulator is in the deflection parameter:

$$K = \frac{eB_0 L}{2\pi m_e c} = 0.934 L B_0 \tag{3.6}$$

where e and m_e are the charge and the mass of the electron, B_0 is the strength of the magnetic field, L is the period of the undulator and c is the speed of light. A insertion device is called an undulator, when K<<1 and a wiggler, when K>>1. In a wiggler, deflection of the electron beam is fairly large, compared to the angular divergence of the emitted X-rays. All emitted X-ray sum incoherently, leading to a broad spectrum with N times higher intensity, compared to a single bending magnet. Here N is the number of pairs of magnets in the insertion device. In the undulator, deflection of the electron orbit is small and all electrons in the bunch emit light coherently, which results in the N^2 increase in the intensity of the emitted radiation. The emission spectrum has the energy width on the order of 1% of the energy of the electron beam.

As can be seen, synchrotrons are pulsed radiation sources by nature. Upon emission of the SR, the electron looses a part of its energy. This energy loss is compensated by the radio frequency (RF) cavity of the synchrotron. RF cavity creates an oscillating electromagnetic field with potential wells that are propagating along the synchrotron ring and in which electrons can be filled. These packages of electrons are called buckets. The revolution frequency of an electron, that moves with the speed, almost equal to the speed of light is defined by the circumference of the storage ring $l_{circumf}$, which in case of PETRA is 2304 m. This results in a revolution frequency of:

$$f_{rev} = \frac{c}{l_{circumf}} \approx 130 \text{ kHz} \tag{3.7}$$

With a fundamental frequency of the radio cavity f_{RF} of 500 MHz, total number of the available buckets is:

$$N = \frac{f_{RF}}{f_{rev}} = 3840 \tag{3.8}$$

A bucket, filled with electrons is called a bunch. PETRA III can operate in 40, 60, 240 and 960 bunch modes. In 40-bunch mode, time between the neighbouring bunches

is 192 ns [54]. This limits the maximum lifetime of the process, that can be studied in this bunch mode. In the top-up operation mode of the synchrotron, electrons are being periodically injected into the storage ring, so that the ring current remains on the level of 100 mA with 1% precision. This ensures highly stable operation, needed for the time-resolved experiments.

3.3.2 P11 beamline

The P11 beamline of the PETRA III synchrotron is equipped with a double crystal monochromator and an advanced KB focusing mirror system, that allows for high energy resolution and microfocusing properties [55]. The beamline is mostly dedicated to X-ray crystallography experiments, but due to the flexibility of the focusing optics can also host pump-probe XAS experiments. A schematic view of the beamline, prepared for the laser pump and X-ray probe experiment is shown in fig. 3.7.

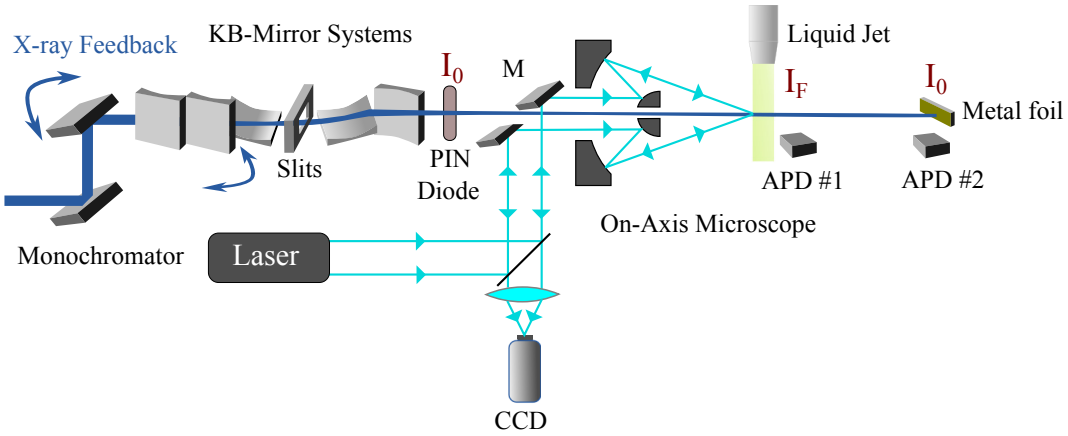

Figure 3.7: Schematic view on the P11 beamline of the PETRA III synchrotron. The synchrotron radiation enters the monochromator which cuts the desired range of energies from it. Focusing of X-rays is performed by the KB-mirrors. The on-axis microscope is used to observe the sample and to couple the pump laser beam to it. The signal from the sample is acquired by the APD1 and the signal from the reference metal foil is acquired by the APD2. X-ray feedback is used to stabilize the position of the X-ray beam on the sample. The figure is adapted from [55].

X-ray radiation from the undulator is passing through a liquid nitrogen cooled double crystal monochromator and is being focused by a first KB mirror system onto the intermediate slit plane. This slit can be used to cut down the size of the intermediate focus to allow to create a focal spot of a size of 1x1 um at the sample position possible. After the intermediate slit the second KB mirror system further demagnifies the X-ray spot size and focuses it on the sample. Between the second KB pair and the sample, there is

additional photodiode, used to measure the X-ray flux, and the on-axis microscope that is used for observation of the pump and probe beams and for focusing of the UV pump beam on the sample. The on-axis microscope has a drilled hole directly in the center, to allow X-rays to pass through it without any losses. 90° flat mirror couples the light from the objective onto a lens, that creates an image of the sample on the CCD camera. The additional beamsplitter (fig. 3.8) is used to couple the light from the pump laser to the on-axis microscope, which focused it on the sample. This configuration allows to focus both pump and probe beams on the sample with no angle between them, which simplifies calulation of the excited state fraction afterwards.

Pump pulses were initially generated by the commercial femtosecond laser system PHAROS from Light Conversion. PHAROS is a solid-state mode-locked laser based on the Chirped Pulse amplification (CPA) technique. The active medium is Yb:KGW with a emission wavelength of 1030 nm. Pump pulses are further frequency tripled by the harmonic generation unit HIRO, resulting in a wavelength of 343 nm. The maximum output power of PHAROS is 6 W and 30% efficiency can be reached in 3rd harmonic generation. During our experiment, CW power of the pump beam was on the order of 50-300 mW on the sample, depending on the sample and the size of the pump laser focus. The repetition rate of the pump laser system is 65 kHz and this frequency was synchronized to the PETRA III bunch clock. After the harmonic generation unit, collimated pump laser light was coupled to the on-axis microscope through the above mentioned beamsplitter and focused on the sample (fig. 3.8).

The sample was delivered by a liquid jet system. A sapphire flat-jet nozzle was attached to a motorized XYZ jet tower, which allowed precise control over the position of the liquid jet. The thickness of the liquid jet, created by the nozzle was 100 µm. The sample solution was stored in a glass vial and pumped from it by a high-precision peristalctic pump. In order to avoid clogging of the sapphire nozzle, porous metal filter was attached to the end of the tube, through which the studied solution was pumped from the glass vial. In addition, the jet tower was equipped with a Ce:YAG crystal, that could be placed to the focal spot instead of the sample and allowed visualization of the pump laser and probe X-ray beams simultaneously on it, to prove their spatial overlap.

Abosorption spectra were measured in a fluorescence yield mode by two avalanche photoiodes (APD's), installed under 90° angle with respect to the X-ray beam. The first photodiode measures the X-ray fluorescence from the studied solution, while the second one collects the signal from the metal foil, located downstream the beam. This allows making shot-to-shot intensity calibration. The metal foil was always selected to be Z-1 with respect to the target atom from the solution, which allows to consider energy-independent X-ray scattering of the metal film, within the range of energies of interest.

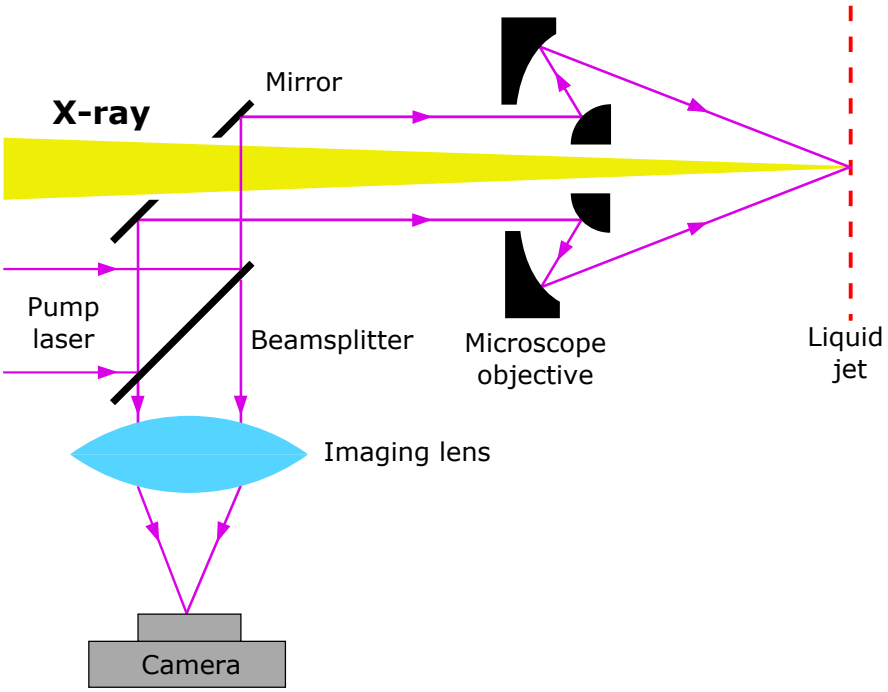

Figure 3.8: Coupling of the X-ray and the pump laser beams on the sample. The microscope objective is used to couple the pump laser beam on the sample and to collect the light from the sample for online imaging purposes. Microscope objective and the imaging lens form the image of the liquid jet on the CCD camera. The formed image is magnified $f_{microsope}/f_{lens}$ times.

3.3.3 Data acquisition and synchronization

Within the data acquisition and processing scheme there are two main circuits: one for the collection of the signal from the avalanche photodiodes, and one for the collection of the data from the PIN diode for the intensity calibration [55]. Within the first circuit, scattered X-ray photons hit the active area of the APD's, with a subsequent photoionisation and formation of a electron avalanche. This results in the internal amplification of the signal by more than two orders of magnitude. After that, the signal, that is directly proportional to the number of the detected events is collected by the pulse processing unit (PPU) and guided further into the fast digitizer unit (model ADQ412AC, 12bit, 2/4GS) from SP devices. The purpose of the fast digitizer is to integrate signals from the APD's, that arrive within defined time regions (gates) with respect to the reference signal. As a reference, signal from the RF cavity of the synchrotron is used. In addition to the reference signal from the RF cavity, digitizer is connected to the 65 kHz reference signal from the laser, in order to distinguish the signal from the pumped and unpumped data channels. The gate delay and the gate width of the digitizer are adjusted so, that the same bunch is always picked for the signals measurements in the pumped and unpumped

channels. The gate selection and timing scheme is presented in fig. 3.9.

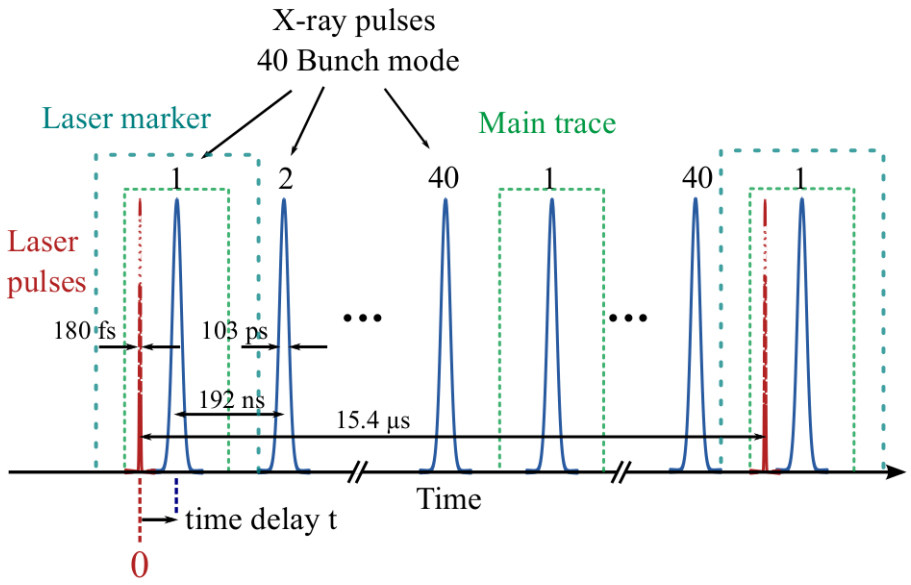

Figure 3.9: Temporal structure of the pump-probe measurement scheme. The repetition rate of the laser is half the revolution frequency of the synchrotron. The figure is taken from [55].

Due to the fact that the repetition rate of the laser is half the revolution frequency of PETRA III, measurement loop in a 40 bunch mode can be described as follows:

- opening of the gate

  arrival of the pump laser pulse

  arrival of the X-ray pulse (Pumped)

- closing of the gate
- skipping of the next 39 bunches
- opening of the gate

  arrival of the X-ray pulse (Unpumped)

- closing of the gate
- skipping of the next 39 bunches

Measurements of the arrival times of the pump and probe pulses were performed by a fast photodiode, temporally installed at the sample position. The active area of the photodiode is sensitive to both UV and X-ray photons. The photodiode was connected to a fast oscilloscope, on which the pump and probe pulses were visualized. The initial temporal

overlap of both pulses was achieved by adjusting the Pockels cell inside the regenerative amplifier of the pump laser. The fine tuning was performed by phase shifting electronics. The gates were selected accordingly. Ideal zero-delay was defined by performing a X-ray delay scan at a fixed beamline energy. The maximum of the transient signal was considered to be the zero-delay point. In the second circuit, the current from the PIN diode was amplified and converted into voltage. This voltage was averaged by a gated analog to digital converter with the same principle as for the first channel. This signal was used for the I_0 intensity calibration.

3.4 X-ray photoelectron spectroscopy

The X-ray photoelectron spectroscopy measurements were performed at the DESY Nanolab, University of Hamburg, Hamburg, Germany. The experimental setup is a commercially available XPS spectrometer from the company *SPECS* [56, 57]. It consists of two main components: a light source with the monochromator, and analyzing and detection unit, that will be further discussed in more detail. All elements work in UHV conditions. This is needed in order to prevent adhesion of the gas atoms or molecules onto the surface of the sample and also to prevent scattering of the photoelectrons by the gas molecules, especially of those with a small kinetic energy.

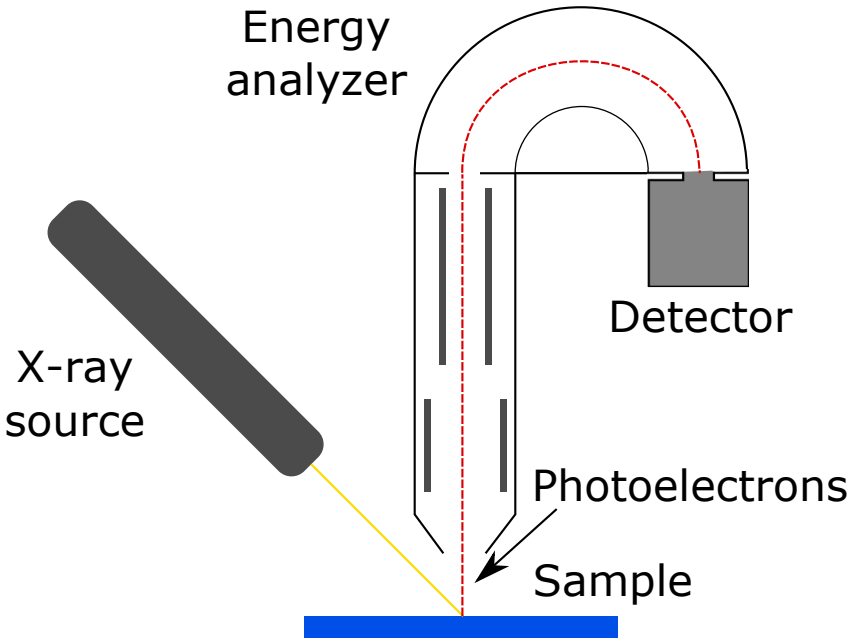

Figure 3.10: Schematic view on the XPS setup. The sample is irradiated with a monochromatic X-ray flux and the kinetic energy of the emitted phototelectrons is analysed.

Table 3.2: The energy and the width of the Kα X-ray emission lines of Mg and Al anodes [30].

Transition	Energy [eV]	FWHM [eV]
Mg Kα	1253.6	0.7
Al Kα	1486.6	0.9

3.4.1 Light source

The most commonly used radiation source in XPS setups, is a twin anode, capable of emitting Al Kα and Mg Kα lines [30]. The experimental setup descried here is also equipped with a twin anode source. X-rays are generated when the anode is bombarded by a high-energy electrons. The electrons are emitted from the electrically heated cathode and are accelerated by a electric field to a energy of several keV before they hit the anode. At a given electron energy, X-ray flux is proportional to the electron current. The anode material defines the X-ray transition that will be excited. Al Kα and Mg Kα transitions have the properties shown in table 3.2.
The energy of the transition defines the maximum energy of the XPS peak in the spectrum, that can be measured with particular type of a source. For Al Kα, Mg $1s$ is the deepest s-level that can be ionized. In order to get high resolution spectra and avoid broadening of the XPS peaks due to the width of the excitation line, experimental setup is equipped with a crystal monochromator. This monochromator allows to cut down the width of the emitted spectrum and also removes the X-ray satellites and the bremmsstrallung. Additionally, the crystal of the monochromator is curved and it provides not only monochromatization, but also a focusing of the X-rays on the sample.
As the measured inorganic compounds are non-conducting, they would get statically charged due to photoionization. Static charging would result in a continuous shift of the XPS peak during the experiment, because additional charge on the surface affects kinetic energy of the photoelectrons. If the charging is not uniform, XPS peaks can also broaden. Therefore, charge compensation was performed with an electron gun, that continuously bombarded the samples surface with low-energy electrons. A series of short survey spectra were recorded in order to select a proper flux of the electron gun and make sure that no static charging effects are present.

3.4.2 Analyser and detector

As a analyser, hemispherical sector analyser (HSA) was used. It consists of two hemispherical electrodes with some gap between them. Voltage is apllied to these electrodes in a way, that the outer electrode with the bigger radius is more negative than the inner

one. If the radii of both electrodes are R_1 and R_2 and the applied voltage is ΔV, then only the electrons with kinetic energy E [30]:

$$E = e\Delta V(\frac{R_1 R_2}{R_2^2 - R_1^2}) \tag{3.9}$$

that pass trough the entrance slit of the analyser, tangentially to the electrodes, will reach the exit slit and hit the detector. Electrons with a smaller kinetic energy will hit the exit slit plane closer to the inner sphere, electrons with a higher kinetic energy will hit the exit slit plane closer to the outer sphere. The above equation can be rewritten as

$$E = ke\Delta V \tag{3.10}$$

with k being the spectrometer constant, defined only by the design of the analyser. Energy scanning is performed by changing the ΔV. If the exit slit of the analyser is replaced by a radially installed multichannel detector, than simultaneous detection of the electrons of different kinetic energies at the same ΔV of the analyser is possible. This can decrease the needed measurement time.

Usually, kinetic energy of the electrons is too high for the analyser, so the electrons have to be retarded. This is performed by the electron lens, that also serves as a collection and collimation objective. There are two possible operation modes: constant analyser energy (CAE) and constant retard ratio (CRR) [30]. The difference between these two modes is the way the electrons are retarded or accelerated and further analyzed. In the CAE mode electrons are accelerated or retarded to some user-defined energy. This results in a constant transmission and absolute value of the resolution in the entire measurement region. In the CRR mode, the electrons are retarded to a fraction of their kinetic energy. In this mode the relative resolution $\Delta E/E$ remains constant. The transmission in this mode increases with the increase in the kinetic energy of the electrons. Our experiments were performed under the CAE mode.

Chapter 4

Results and discussion

In this section results of the application of the soft- and hard- X-ray as well as the optical spectroscopy techniques to the bio-inorganic compounds are presented. The studied bio-inorganic compounds have different organization of the central metal core, surrounded by various ligand environments, which results in peculiar chemical, electronic and optical properties of these compounds. The compounds $Cu(TMGqu)_2$ and $Cu(DMGqu)_2$ have single copper atom in the center of the molecule and are a subject to the entatic state concept. Oxygenated form of the [Cu(btmgp)]I and $[Cu(TMG_2tol)]_2$ complexes has two copper atoms in the center and they are a model complexes for the tyrosinase and hemocyanine metaloproteins, capable of reversible oxygen binding and catalysis of special chemical reactions. The iron-based $Fe(Pz_2Py)_2$ compound possesses spin crossover phenomenon upon optical excitation. All these features will be discussed in the following sections. The chapter begins with the results of the advanced alignment of the VUV Raman spectrometer, aimed on studying quasiparticle excitations in the above mentioned class of material systems at their L and M absorption edges.

4.1 Alignment of the VUV Raman spectromter

As has already been discussed in section 3.2.3, each spectrometer stage of the VUV Raman spectrometer works according to the Cherny-Turner optical scheme and enables aberration-free spectral imaging on the optical axis. The design capacitate to achieve superior resolution and stray light rejection, however requires special care in the alignment of the instrument. Three different techniques were combined in order to align the optical components and verify their aligned state. As the main alignment technique optical laser interferometry was employed. It allows to evaluate the quality of the laser wavefront behind different optical elements of the monochromator with the precision on the order of the wavelength of light used (here 632 nm). Complementary, wavefront sensing was used and the results, obtained by the wavefront sensor were cross-checked with the ones from

the optical laser interferometry studies. Finally, the alignment quality of the monochromator was validated by employing an off-line X-ray source which has been adapted to provide soft X-ray photons and by that could be used to perform systematic performance tests in the energy region of interest and independent of the FEL availability. Prior to alignment of the VUV Raman spectrometer, which is a large scale setup, a model setup was built and applicability of the interferometric alignment concept to it was demonstrated. Additionally, the model setup allowed to define key degrees of freedom of each optical element, that need to be adjusted, as well as the tolerances of these adjustments.

4.1.1 Verification of the alignment concept with a model setup

In order to demonstrate applicability of the interferometric alignment approach to the VUV Raman spectrometer and to obtain experience in interpretation of the interference patterns and corrections of the corresponding aberrations, a model setup was constructed. The model setup consists of a Laser Unequal Path Interferometer (LUPI), three 90° off-axis parabolic mirrors (OAP) with parental focal distance of 75 mm and two flat optical mirrors, all mounted on a common optical breadboard. The optical scheme of the test setup along with a picture of it are presented in fig. 4.1. The SP1 monochromator is represented by two off-axis parabolic mirrors (OAP 2 and OAP3) and OF between them. Two OAPs correspond to mirrors M1 and M2 of the SP1 monochromator and OF represents the blank mirror or the diffraction grating of the SP1 in 0^{th} order. The first parabolic mirror OAP1 focuses the light in the test arm of LUPI to create a source point for OAP2.

The alignment of the model setup starts with the LUPI and OAP1. The goal of the first alignment step is to make optical axes of OAP1 and LUPI test arms collinear, to achieve aberration free focal spot behind OAP1. For this, beam from LUPI is directed on the OAP1 and focusing quality is checked by installing a white screen in the focal point of OAP1. The shape of the focal spot must be improved to the smallest and most circular one by adjusting pitch, roll or yaw angles of the OAP1. When this is achieved, the screen is replaced with the OF and residual aberrations are further minimized by judging on the LUPI interference pattern. At the next step OF must be moved behind OAP2 to provide backreflection on it. Here, foci of the OAP1 and OAP2 must be overlapped to achieve a proper collimation of the beam behind OAP2. Finally, OAP3 (M2) is aligned. This step is essentially the same as step 1, as it requires adjusting the pitch, roll and yaw angles of the OAP mirror.

Based on experience obtained with the model setup, it was concluded that judging immediately on the interference pattern at step two might be not straightforward, because strong aberrations might still be present in the system and these aberrations contribute to the formation of the combined interference pattern, that is hard to interpret. There-

fore, the alignment of the OAP2 (and M1 in the real setup) must be performed first with retroreflection cube and only then with high-quality optical flat mirror. The procedure of the OAP2 alignment was split into three steps: 1) prealignemnt with a retroreflector cube and imaging lens 2) interferometric alignment with a retroreflector cube 3) final interferometric alignment with OF. In addition, the conclusion was made that for the SP1 monochromator it is more efficient to bring the source point of LUPI to the M1 focus, instead of moving either mirror M1 or the entire monochromator chamber to the LUPI source point. Therefore, for the SP1 alignment LUPI was mounted on a common platform with the OAP1, and this platform was installed on a hexapod that allowed precise control over the position of the source point and its efficient correction. All alignment steps applied to the SP1 monochromator are described in the following section.

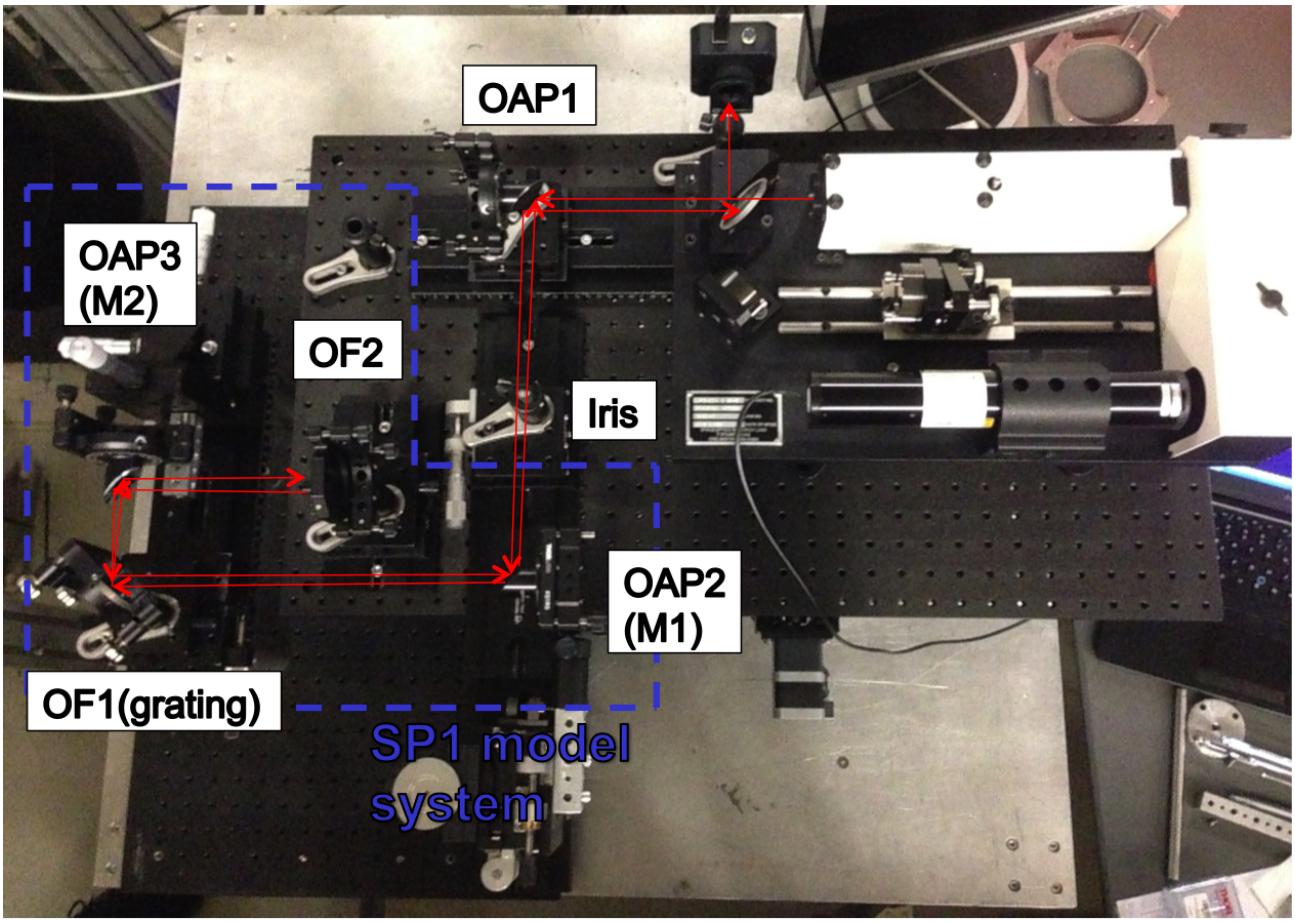

Figure 4.1: Photo of the SP1 model setup. The propagation of the laser beam from the LUPI interferometer is shown with red arrows

4.1.2 Optical alignment

In this section the procedure and the results of the internal optics alignment of the single VUV Raman monochromator (SP1) are presented. The optical alignment approach was

based on using a Laser Unequal Path Interferometer (LUPI) from Space Optics Research Lab, coupled with a 90° off-axis focusing parabolic mirror (FP), to provide a source point for the VUV Raman monochromator (fig. 4.2). A single mode He-Ne laser with central wavelength of 635 nm is used to provide the laser beam for the interferometric alignment procedure. LUPI and FP were mounted as one unit on a common laser breadboard, installed on a hexapod from Physik Instrumente (PI, model number H-850.H2). This allowed precise control over the source point position and its fine-tuning. Complementary, the evaluation of the alignment quality was performed via wavefront-sensing measurements [58].

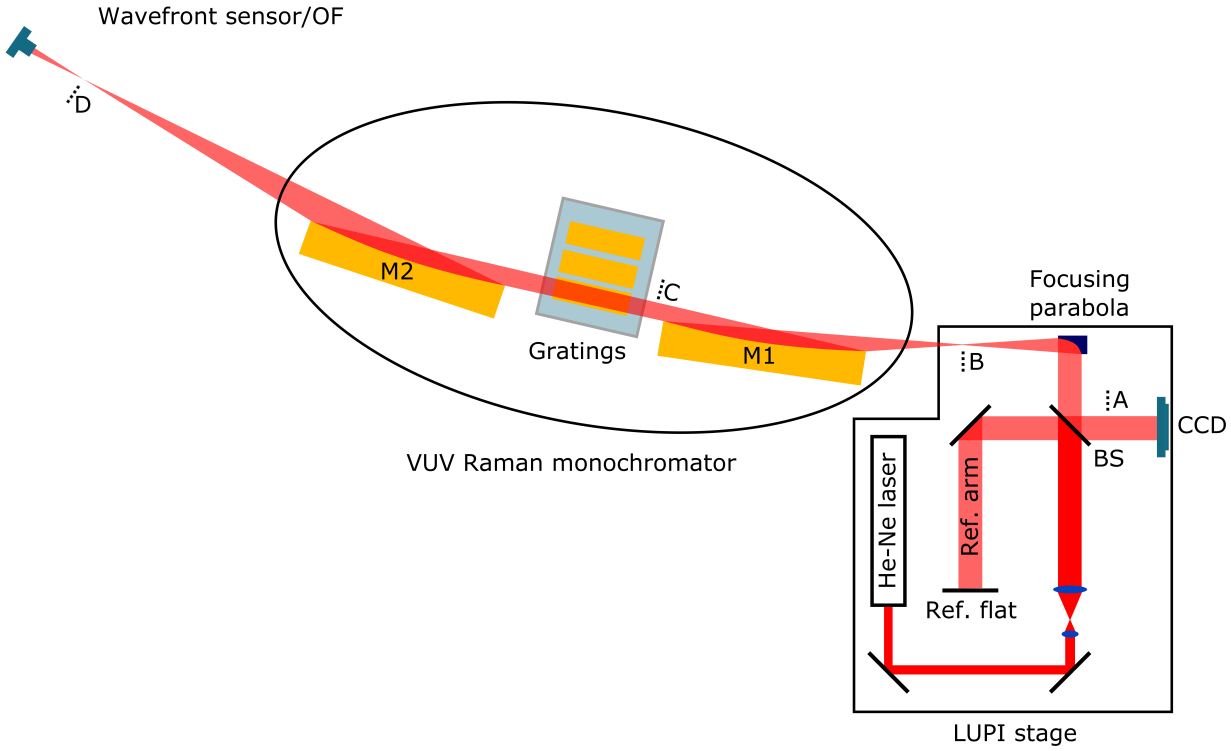

Figure 4.2: Optical scheme of the LUPI stage, coupled to the VUV Raman monochromator chamber. The beamspliter splits the beam from the single mode He-Ne laser into reference and test arms and recombines them again on the CCD. The beam in the test arm is focused by the FP to create a source point for the M1 mirror of the monochromator. During different stages of the alignment process, optical flat mirror (OF) has to be placed at points B, C, or D. An imaging lens can be placed at position A for pre-alignment purposes. A retroreflector was used at position C

Interferometer preparation

At a first alignment step, the laser beam in the test arm of the LUPI spectrometer has to be focused to create a source point for the first mirror M1 of the VUV Raman

spectrometer. Considering the numerical aperture of the OAP mirror M1 and the need to fold the laser beam due to space constraints in the FLASH experimental hall, a 90° OAP mirror with parental focal distance of 75 mm was used. The surface quality for the OAP mirror is $\lambda/4$. The mirror is 1 inch in diameter, which corresponds to an f-number of 5.91. Given the smaller f-number of the focusing parabola, compared to that of M1, means that the mirror M1 is over illuminated by the FP. Thus, only the central part of the wavefront with the highest quality, provided by the FP, will illuminate M1 and participate in the formation of the interference pattern. The FP is placed in a kinematic mount which allows pitch, roll and yaw adjustments. The alignment was performed according to the scheme depicted in fig. 4.2. A high quality ($\lambda/20$) optical flat mirror (OF) was placed in the focal point of the FP (position B) and the pairs of degrees of freedom pitch/yaw of the focusing parabola and tip/tilt of the OF were altered together to achieve parallel and uniformly distributed fringes in the interferogram.

Alignment of the interferometer to mirror M1

In order to bring the source point of the LUPI close enough to the focus of mirror M1 and to obtain a visually resolvable interference pattern which then could be further corrected, a prealignment step is needed [59, 60]. For this purpose, a retroreflector prism ($\lambda/10$ quality) was placed behind M1 at a distance of approximately 10 cm (fig. 4.2, point C). The beam in the reference arm was blocked and an imaging lens was put into the test arm in front of the CCD camera such that the camera is in the focus of the lens (fig. 4.2, point A). This allowed the observation of the return spot from the test arm, focused on the CCD (see fig. 4.3). The goal of this pre-alignment step was to achieve the best possible focusing of the return spot. As a retroreflector always provides back reflection, only adjustments of the hexapod in X, Y and Z coordinates were needed. The initially obtained shape of the return spot was a skewed line. Vertical adjustment of the hexapod (fig.4.3 (a)-(c)) corrected the angle of the line towards the horizontal, thus removing the XY component of the observed astigmatism. Continuous horizontal adjustment (fig. 4.3 (d)-(f)) allowed focusing of the return beam to the smallest possible round-shaped spot, meaning that this pre-alignment step is complete. After finishing the pre-alignment, the retroreflectror was replaced with the high quality optical flat mirror, the imaging lens was removed and the beam in the reference arm was unblocked, thus revealing an interference pattern on the CCD chip. Further and therefore more precise alignment is achieved by adjusting the horizontal/vertical position of the source point followed by a tip/tilt correction of the OF.

A sequence of interferograms, showing progressive vertical and horizontal alignment is presented in fig. 4.4. The obtained pattern is cross-like with an additional tilt, indicating both Y^2-X^2 and XY astigmatism, according to Zernike theory [61]. Such a pattern appears

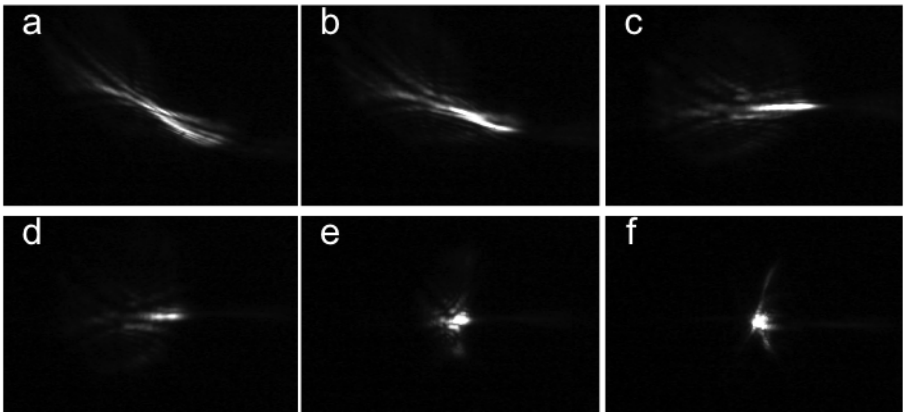

Figure 4.3: Return spot from M1, focused on the CCD chip. (a)-(c) correction of the vertical error. (d)-(e) shrinking of the line profile into a spot by gradual correction of the horizontal error.

due to a wrong height and off-axis distance (OAD) of the source point with respect to mirror M1. The correction of the vertical offset (fig. 4.4 (a)-(c)) results in a gradual rotation of the "cross" such that it is symmetric with respect to the center horizontal and vertical lines. This adjustment removes the XY components of the astigmatic aberration. As soon as this is achieved, the OAD needs to be corrected. A shift of the source into the correct direction results in the enlargement of the cross and finally in its transformation into set of concentric circles (fig. 4.4 (d)-(g)). The next alignment step is adjusting the source to the correct focal distance. Again, a shift in the correct direction along the M1 optical axis enlarges the circles and increases the period of the interference pattern.

Finally, a uniform intensity distribution (piston) can theoretically be achieved, meaning that two plane parallel waves interfere. Vibrations in the experimental hall and air turbulences can obscure the interference pattern and residual aberrations, which makes further improvements challenging in particular when the source point is very close to the M1 focus and the observed fringes period is such that not more than 1-2 fringes are visible. Therefore, after obtaining a piston-like pattern, a tilt was introduced to the system deliberately. This was achieved by tipping/tilting the reference flat to observe five to seven horizontal and vertical lines in the pattern, respectively. The goal was to make them symmetric around the imaginary line that goes through the middle of the interference pattern, perpendicular to the fringes (fig. 4.5). This would mean that the reflected wavefront in the reference arm is flat and the source point is in the focus of M1. First, the reference flat mirror of the LUPI was tilted to obtain vertical lines in the pattern. The vertical position of the source point was adjusted together with the tip of the OF to achieve the required symmetry condition (fig. 4.5 (a)-(c)). After that, the reference flat was adjusted to observe horizontal fringes. OAD of the source point and

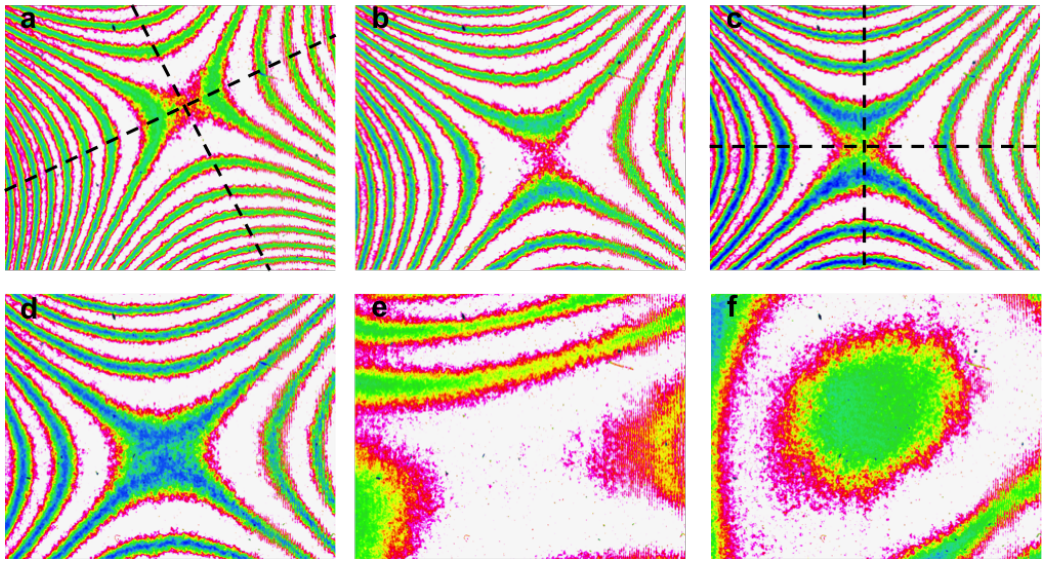

Figure 4.4: Interferograms showing alignment of the LUPI to the M1 mirror. OF was used to povide backreflection on M1. (a)-(c) progressive vertical alignment leads to the rotation of the astigmatic „cross“ pattern. (d)-(f) good vertical and progressive horizontal alignment. Some residual vertical misalignemnt becomes visible on image (f).

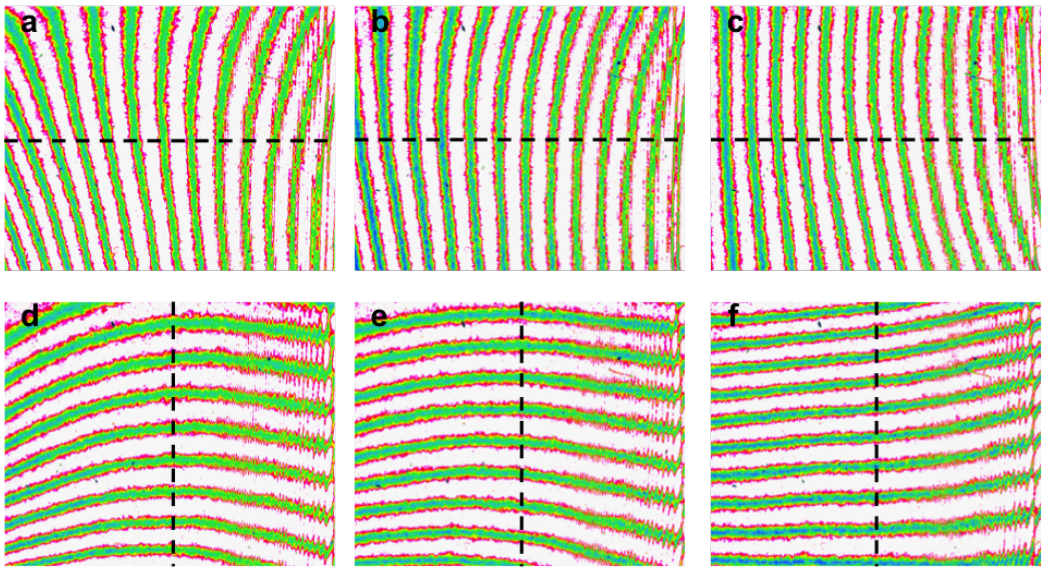

Figure 4.5: Introduction of the tilt into the system for visualisation of the residual aberrations and their consequent correction. (a)-(c) correction of the vertical error. (e)-(f) correction of the horizontal error. (c) and (f) are the final interference patterns.

tilt of the OF were optimized to form parallel and straight fringes (fig. 4.5 (e)-(f)). Fig. 4.5(c),(f) show the final optimized patterns. After having aligned the LUPI system to M1, the optical flat mirror was removed and the spectrometer grating bench was rotated into a 90° configuration perpendicular to the optical axis of M1, in order to provide back-reflection of the collimated light on M1. This configuration allowed to align all gratings installed to have identical interference patterns and by that ensuring that the imaging properties of the spectrometer as well as its resolution will not depend on the grating that is being used. The obtained interferograms of the installed gratings and the mirror blank are compared in fig. 4.6.

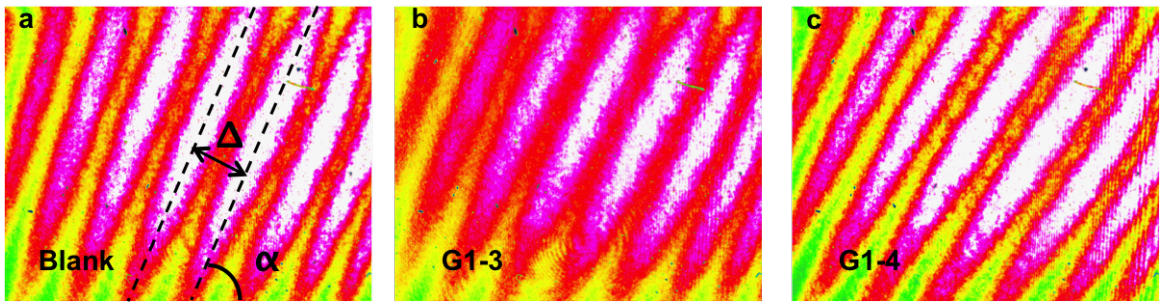

Figure 4.6: Tilt fringes, showing resulting alignment of the blank mirror (a) and the installed diffraction gratings (b), (c). The patterns are obtained, by placing the abovementioned optical elements (diffraction gratings, blank mirror) in the 90-degrees orientation, to provide backreflection on M1. The identical tilt of the fringes and their equal periods confirm their proper alignment with respect to each other and to the M1 mirror.

Alignment of the mirror M2

After having aligned the LUPI-M1-gratings systems, the grating bench was returned to its nominal 0^{th} order diffraction position of 9° relative to the optical axis of M1 and the OF was placed on a high-precision translation stage in the focus of the parabolic mirror M2 (see fig. 4.2, point D). The interference pattern showed presence of both Y^2-X^2 and XY astigmatism contributions. The latter could be corrected by either changing the pitch of the grating bench or the Yaw angle of the mirror M2. The correction of the XY astigmatism was achieved by small adjustment of the 0^{th} order angle of the grating bench by less than 2 mrad. In order to obtain a full quantitative analysis of the remaining aberrations we switched from interference pattern measurements to wavefront sensor measurements. A direct measurement of the wavefront eliminates the issue of low contrast in the interference pattern due to intensity attenuation of the light in the test arm of the LUPI, compared to its reference arm. The reason for the low intensity is because of six additional reflections from M1-blank mirror-M2 upon forward and backward light

propagation, considering that the mirror diamond-like carbon coating is optimized for VUV photons.

Wavefront measurements were carried out using a Hartmann-Shack wavefront sensor from Laser-Labratorium Göttingen e.V (LOT). It is sensitive in the wavelength range of 350 nm — 1100 nm and consists of a 12 mm x 12 mm microlens array in a focal distance of 3.6 mm to the CCD camera. The lenses are 150 µm x 150 µm in size. The 12 bit CCD camera has a resolution of 1280 x 1040 pixels with a field of view of 8.25 mm (h) x 6.6 mm (v). The absolute accuracy at 633 nm is between $\lambda/50$ to $\lambda/150$, with a relative sensitivity up to $\lambda/10000$.

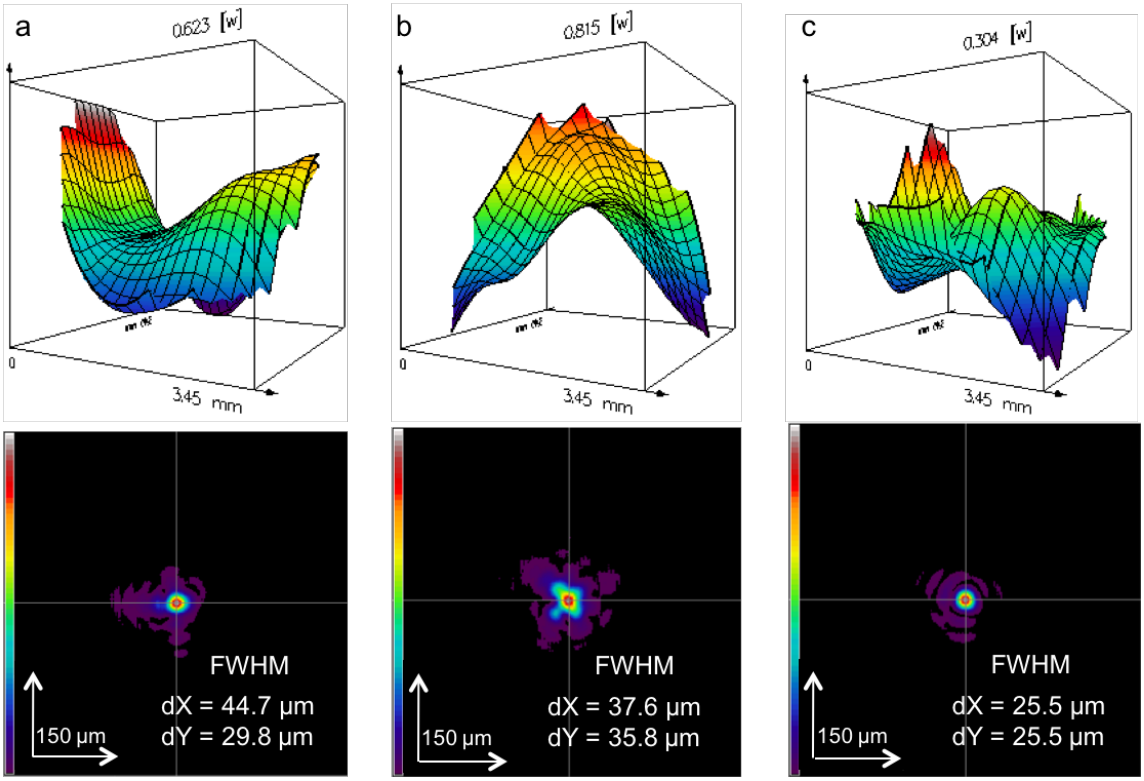

Figure 4.7: In the upper row measured wavefronts behind the mirror M2 are shown at the position of the wavefront sensor. The inital wavefront shows dominant presence of astigmatic contributions (a), wavefront after pitch optimization of M2 (b) and the final wavefront after alignment of roll and x of M2 (c). The peak-to-valley value for each wavefront is given in λ and could be reduced to about half of the initial value. The lower row shows the intensity profiles at the focus position of M2. They were retrieved by Fresnel back-propagation of the intensity profile measured at the position of the wavefront sensor. The focus size in x and y direction is given in fwhm for the cross marked positions. The focus size could significantly be reduced to a round shape of about 25.5 µm each in x and y direction.

Table 4.1: Zernike aberrations, corresponding to the wavefronts of fig. 4.7 for λ=633 nm.

Zernike aberrations	(a)	(b)	(c)
Astigmatism Y^2-X^2	0.237 λ	0.115 λ	0.021 λ
Astigmatism XY	0.079 λ	0.375 λ	0.002 λ
Coma X	0.109 λ	0.071 λ	0.077 λ
Coma Y	0.009 λ	0.032 λ	0.000 λ
Triangular coma	0.051 λ	0.019 λ	0.049 λ
Quadratic astigmatism	0.008 λ	0.038 λ	0.017 λ
Spher. aberration	0.008 λ	0.046 λ	0.016 λ

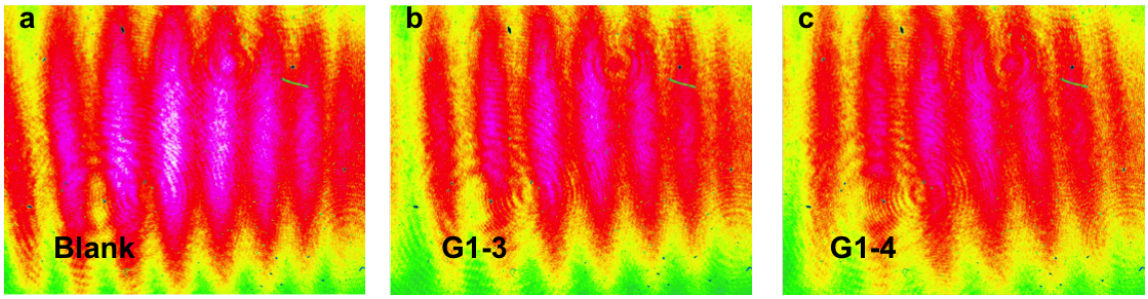

Figure 4.8: The interference fringes, showing the final alignment of the blank mirror (a) and diffraction gratings (b), (c). The patterns were obtained after M2 alignment with OF placed in M2 focus. The identical tilt of the fringes and their equal periods indicate interference of two plane waves thus confirming proper alignment of the optical elements with respect to each other as well as to the mirrors M1 and M2.

Wavefronts, showing the alignment procedure of the M2 mirror together with the focal spots retrieved by Fresnel back-propagation of the measured intensity distribution are presented in fig. 4.7. The first Zernike aberrations for each wavefront were calculated using the Arizona-Fringe notation with 37 polynomials and are summarized in table 4.1 (Laser Beam Profiler MrBeam 1997-2017). In the upper row of fig. 4.7 the measured wavefronts behind the mirror M2 are shown at the position of the wavefront sensor which was installed approximately 30 cm behind the focus position of M2. In fig. 4.7 (a) the initial wavefront behind the mirror M2 prior to correction of the 0^{th} order angle of the grating bench is dominated by the Y^2-X^2 astigmatic contribution, in agreement with the interferometric measurements. Optimization of the M2 pitch angle corrects the Y^2-X^2 component of the astigmatism (fig. 4.7(b)), leaving the XY one. Finally, correction of roll and x of the M2 mirror eliminates the remaining aberrations and yields to the final wavefront, shown in fig. 4.7(c). The peak-to-valley value for each wavefront is given in

λ and could be reduced to about half of the initial value. The size of the focus could significantly be reduced to a round shape of about 25.5 µm each in x and y direction. After completion of the M2 alignment, OF was returned to the focus of M2 and gratings bench was scanned, yielding final interference patterns of the aligned SP1 optical elements (fig. 4.8) with different gratings of the monochromator chamber, installed in the beam and confirming proper alignment of the system. The best straightness and parallel nature of the interference pattern can be obtained for the blank and grating G1-3, whereas G1-4 shows a slightly increased tilting of the interference fringes.

4.1.3 Offline X-ray measurements

After completion of the interferometric alignment with visible photons, the performance of the spectrometer was characterized in the soft X-ray range utilizing a special X-ray tube, the so called "Manson's source" McPherson Light source, model 642, depicted in fig. 4.9. The source is equipped with a 200 µm pinhole rigidly mounted in front of the photon emitting anode at the distance of 16 mm (see fig. 4.9). For spectrometer performance characterization, the photon emission at the $L_{2,3}$-edges of the Al edge of the Al-Mn anode was investigated.

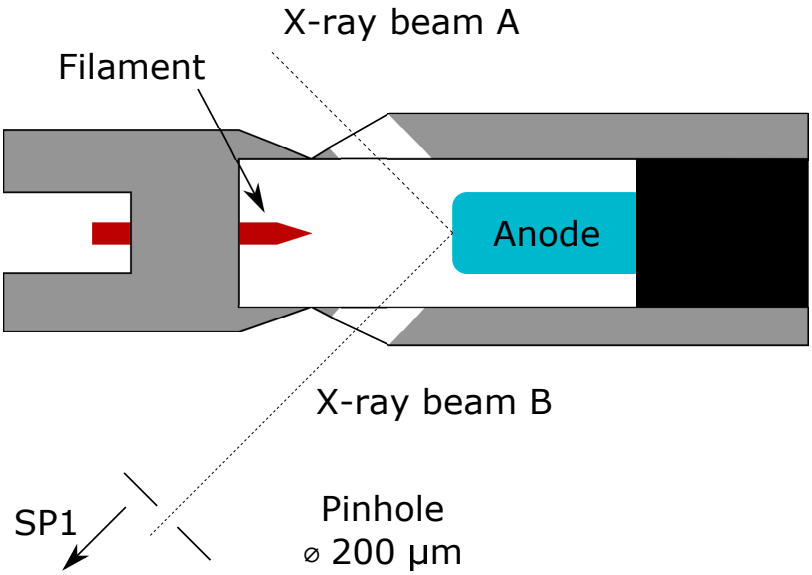

Figure 4.9: Schematic drawing of the X-ray source, used in verification of the spectrometer performance. The pinhole is located 16 mm away from the anodes surface.

The chamber with the X-ray tube was mounted on the hexapod instead of the LUPI interferometer and the pinhole was brought to the M1 focus. Both, the Manson's source pinhole and the LUPI pinhole were fiducialised in advance. The replacement of the LUPI with Manson's source was performed under surveying with approx. 300 µm precision. The wavefront sensor (fig. 4.2) was replaced by an ICCD camera from Princeton Instruments

(PIXIS-XO 2048B), attached to the spectrometer chamber via the metal bellows and placed in the nominal focal position. The mounting platform below the ICCD camera is motorized and allows moving the camera along the optical axis of M2. The entire system, consisting of the monochromator and the ICCD camera acts like a one-stage spectrometer. A 3D scan of the source position combined with a longitudinal scan of the ICCD position was performed with spectrometer in 0^{th} order (imaging mode) to bring the X-ray source exactly to the M1 focus with an accuracy of 50 µm. An optimized pinhole image was obtained at the position of the ICCD camera x_0=125 mm in our coordinate system.

The spectrometer performance in the soft X-ray range was tested in terms of imaging properties in 0^{th} diffraction order, in terms of spectrally resolving properties in 1^{st} and 2^{nd} diffraction orders as well as simulations were done for a comparison. These verification steps will be discussed in more detail in the following sections.

Comparison of the SHADOW simulations with X-ray source experiment

Prior to performing the alignment procedure and experimental studies with the Manson's source, the first monochromator stage and the source have been extensively studied in terms of possible effects of optics and source point misalignments via ray tracing using SHADOW software package [62]. The ray tracing was performed by Siarhei Dziarzhytski and results of the ray tracing are summarized here. The source for the ray tracing has an uniform photon energy distribution from 73.1 eV to 61.1 eV to mimic the 12 eV energy width of the Al $L_{2,3}$ emission line [63–65], circular shape with radius of 0.3 mm, and a uniform divergence of 14 mrad in fwhm.

Specifications and slope errors of the optical elements of the first monochromator used for the ray tracing can be found in [66]. Here, the only difference is that an additional circular pinhole with 0.1 mm radius is placed at a distance of 550 mm in front of the first parabolic mirror M1, i.e. in its focus. The source is placed at a distance of 566 mm from the mirror M1, which corresponds to the actual distance of 16 mm between the anode surface and the limiting pinhole.

As the spectrometer disperses the collected light in the vertical plane, the vertical source size and its spectral bandwidth defines the spectral resolution of the spectrometer to a large extend. The calculated highest spectral resolution of the spectrometer at 73 eV photon energy presuming a vertical source size of 200 µm is 220 meV for the grating G1-3 (576 l/mm groove density) and 90 meV for G1-4 (1120 l/mm groove density), respectively, both working in the 1^{st} diffraction order. The resolution of the spectrometer with G1-3 grating in 2^{nd} diffraction order at the same photon energy is 85 meV.

Ray tracing results for the spectrometer imaging properties in 1^{st} diffraction order along the beam caustic in comparison with experimentally recorded images of the pinhole are

shown in fig. 4.10. The detector plane has been shifted upstream and downstream by 35 mm relative to the nominal focal position (see fig. 4.10 (a), (b) and (c)). A change of the slope of the high energy flank (right side) along the caustic is observed in both simulations and experiment. The line is added as an eye guide in the figures. Such a change of the flank leads to a decrease of the spectrometer resolution due to smearing out the sharp L_3 rising edge and L_2 peak while binning. This criterion was used in the measurements with the X-ray tube to define the focal position of the SP1 monochromator unit.

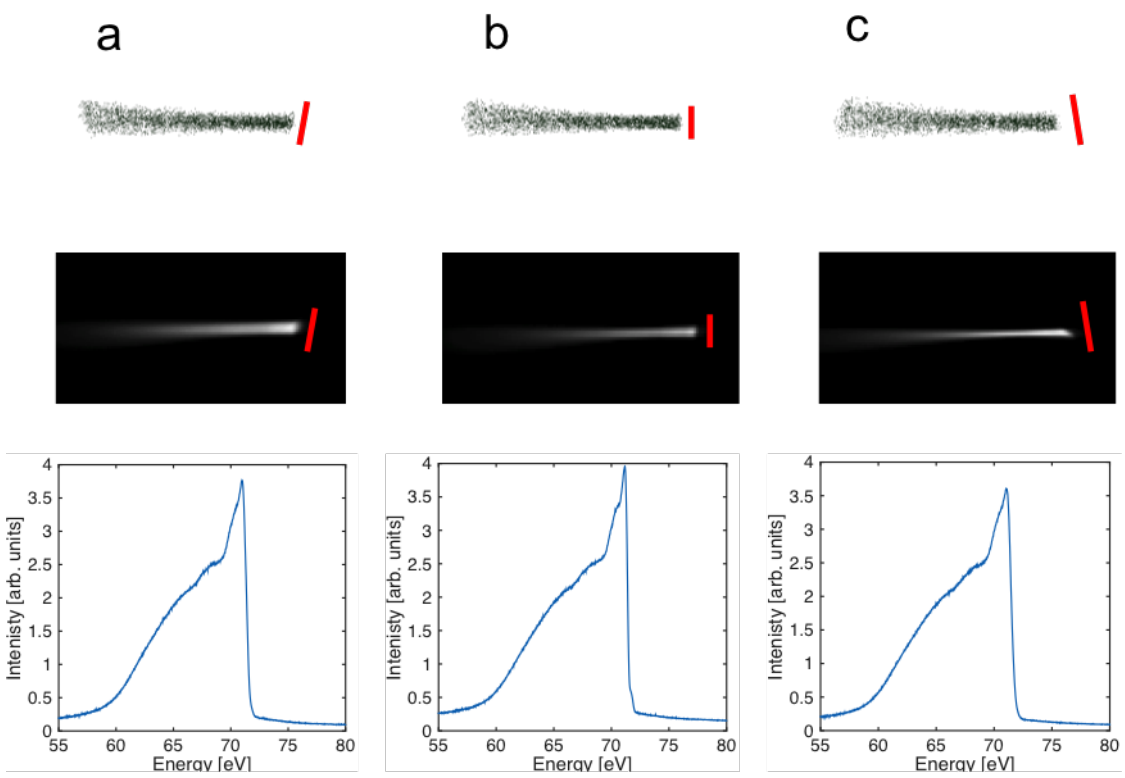

Figure 4.10: Simulated (top row) and measured (middle row) 2D images of the Al $L_{2,3}$ band as well as projected intensity profiles (bottom) for different longitudinal positions of the detector: -35 mm from the nominal focus (a), in focus (b) and +35 mm from the focus (c)). Change of the slope of the high energy flank (right side) along caustic is observed in both simulations and experiment. The line is added as an eye guide. Energy is increasing from left to right.

Determination of the focal position

Aberrations lead to the distortion of the image in the 1st order, resulting in a decrease of the slope of the rising edge of the Al L_3 emission peak and smearing out spin-orbit

coupling, thus providing a good criterion for the position of the focal plane of the spectrometer and its resolution. This criterion is especially applicable, because Al L_3 edge has a sharp rising edge near the Fermi energy E_f, which is mostly broadened due to instrument response function [63–65]. The longitudinal position of the ICCD camera was scanned within ±35 mm range from the position, where the best 0^{th} order image was found. The recorded spectral intensity distribution at each detector position was background corrected and integrated within the region of interest, yielding the Al $L_{2,3}$ X-ray fluorescence spectrum (fig. 4.10, bottom, fig. 4.12 (a)). The slope of the rising edge of

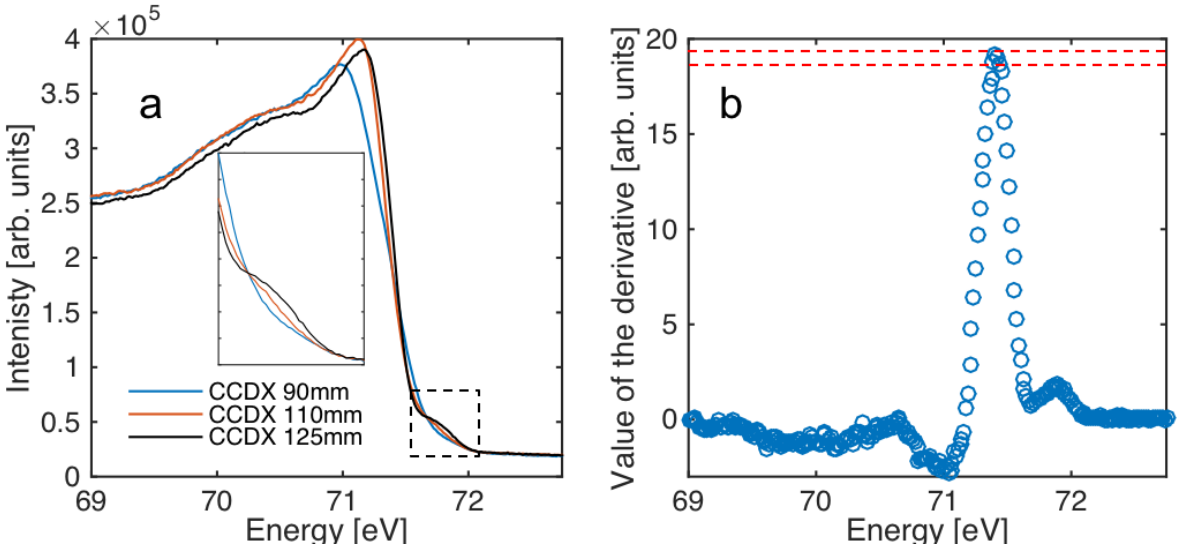

Figure 4.11: (a) Formation of the pre-edge feature at 71.8 eV and decrease in the slope of the rising edge of the Al $L_{2,3}$ spectrum upon approaching to the CCDX=125 mm position. (b) Example of the derivative used for the slope analysis (first derivative of the spectrum, measured with the G1-3 grating in 1^{st} diffraction order at CCDX=125 mm). Red lines indicate the borders of the range, within which the average value of the derivative and the error bar are calculated.

each spectrum was calculated as the average of 5 highest values of the 1^{st} derivative of the measured spectrum in the vicinity of the rising edge (see fig. 4.11(a), (b)). Error bars were calculated from these 5 points. Slope dependencies for each grating were normalized to 1. Measurements were performed for grating G1-3 in 1^{st} and 2^{nd} diffraction orders, mimicking different photon energies, and for G1-4 in 1^{st} diffraction order. The results of the analysis are presented in fig. 4.12, and are summarized in table 4.2. As one can see, the maxima for all scans are within the range of 123.2-125.3 mm, whereas the optimum 0^{th} order image was found to be at 125 mm. This confirms that the position of the focal plane for both gratings does not change within the measurement precision when going from 0^{th} diffraction order to 73 eV for G1-4 grating and 73 eV and 36.5 eV energies for G1-3 grating, respectively. This ensures that the spectrum after the first monochromator

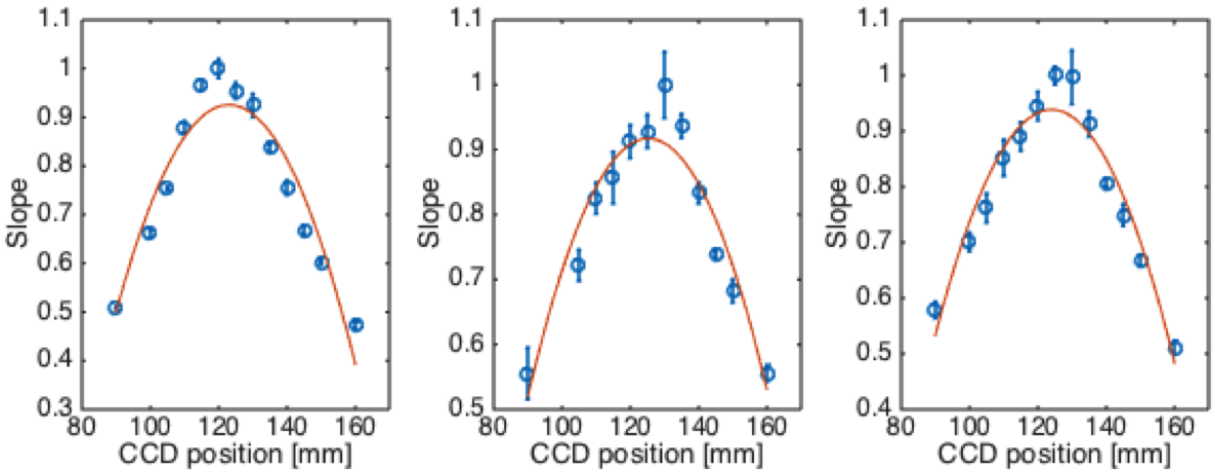

Figure 4.12: Increase in the slope of the rising edge of the Al $L_{2,3}$ X-ray fluorescence spectrum for G1-3 grating in 1st order (left), G1-3 in 2nd diffraction order (middle) and G1-4 in first diffraction order (right) upon approach of the CCD position to 125 mm. Red line is the fit of the parabolic function to the data.

stage will always be projected onto the fixed intermediate slit plane, most efficiently suppressing the stray light and coupling the desired energy window correctly into the second monochromator.

Table 4.2: Positions of the maximum of the parabolic fit with 0.9 confidence bounds to the experimentally measured dependencies of the slope of the rising edge of the Al $L_{2,3}$ X-ray fluorescence. Optimum 0th order position is at 125.0 mm.

G1-3 1st order	G1-3 2nd order	G1-4 1st order
123.2±3.2 mm	125.3±3.5 mm	123.9±3 mm

Table 4.3: Comparison of the spectrometer resolution measured with Manson's source and calculated in SHADOW.

Grating	G1-3	G1-3	G1-4
Photon energy	73 eV	36.5 eV	73 eV
Experiment	239±24 meV	102±10.2 meV	200±20 meV
Theory	220 meV	85 meV	90 meV

A zoom to the rising edge region of the Al $L_{2,3}$ spectrum, confirming the improvement

of the resolution and formation of the L_2 pre-edge (inset) upon correction of the ICCD longitudinal position is presented in fig. 4.11(a). Estimated width of the L_3 edge as a measure of the spectrometer resolution recorded with different gratings and diffraction orders is compared with the theoretical ones obtained in the ray-tracing, are summarized in table 4.3. It can be seen, that for grating G1-3, both, first and second order resolutions determined from the experiment match the ray tracing results. Grating G1-4, however, shows a resolution which is about a factor of two off. This might be connected to a number of factors indicating a worse quality of G1-4 such as grating inhomogeneities, which are difficult to address through a ray-traycing simulation. Furthermore , as already discussed, the interference fringes in fig. 4.8 for grating G1-4 do not show the same quality of the straightness and are not as parallel to each other as compared to grating G1-3. Together this can explain in the reduced resolution of grating G1-4.

4.1.4 Conclusions

An advanced alignment concept was applied to the VUV Raman monochromator. Optical laser interferometry measurements together with wavefront measurements were used to align the monochromator. Both methods qualitatively and quantitatively verify the alignment. The aligned state of the instrument was further confirmed in the VUV energy range by investigating the X-ray fluorescence at the Al $L_{2,3}$ edge with the help of an off-line X-ray source compared with SHADOW ray-tracing results. Taking into account that the investigated effective energy range covers almost the entire working range of grating G1-3 and the identical interferometric alignment of both gratings, it can be concluded that the spectrometer performs within its design specifications.

4.2 Photoinduced structural changes in the $Cu(TMGqu)_2$ complex

This section focuses on investigation of the electronic and structural properties of the $Cu(TMGqu)_2$ complex [67], as well as on its characterisitc relaxation timescales. The oxidation state of the central copper atom can be changed from +1 to +2 via metal to ligand charge transfer process. This transition is facilitated by the entatic state of the complex. The experimental data was obtained by performing pump-probe XAS measurements at the Cu K-edge on the solvated sample. The results shown here are based on the results already published in [68] as well as on the original data analysis. Both XANES and EXAFS energy regions of the measured X-ray absorption spectra are considered in the analysis. The $[Cu(TMGqu)_2]^+$ compound will be referred within this section as Cu(I) and $[Cu(TMGqu)_2]^{2+}$ will correspondingly be referred to as Cu(II).

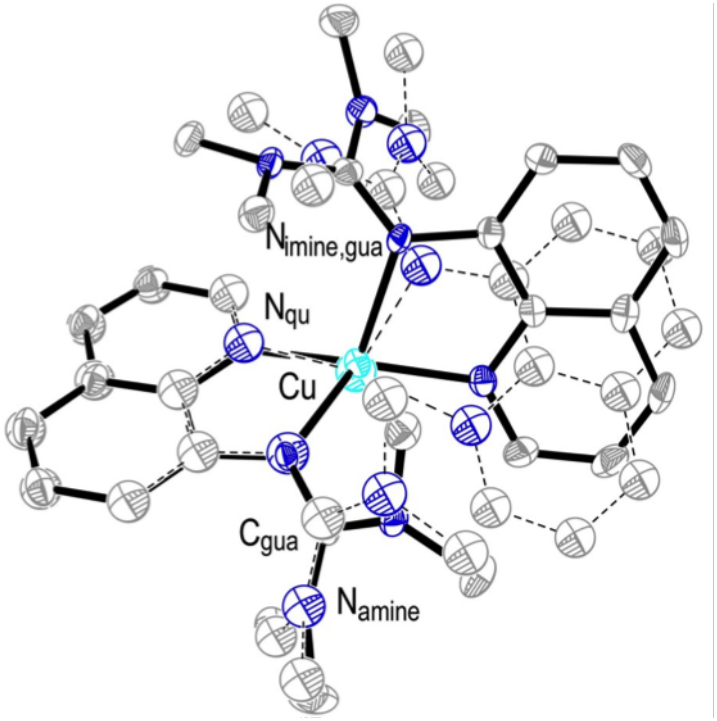

Figure 4.13: Schematic representation of the molecular structure of the $Cu(TMGqu)_2$ complex with the oxidation state of the central copper atom of +1 and +2. Dashed bonds correspond to the Cu(II) molecule and solid bonds correspond to the Cu(I). The figure is taken from [11].

4.2.1 Ground and excited state spectra

X-ray absorption measurements at the Cu K-edge can provide valuable information about the oxidation state and the geometrical environment around the Cu atom. The availability of the ground state $Cu(TMGqu)_2$ compounds with the oxidation state of the Cu atom of +1 and +2 allows to confirm in a pump-probe experiment that metal-to-ligand charge transfer takes place and to estimate its dynamics. Normalized XANES spectra for the ground state (GS) of the Cu(I) and Cu(II) (further referred to as $Cu(I)_{GS}$ and $Cu(II)_{GS}$ correspondingly) and the optically excited state (ES) of the Cu(I) (further referred to as $Cu(I)_{ES}$) are presented in fig. 4.14.

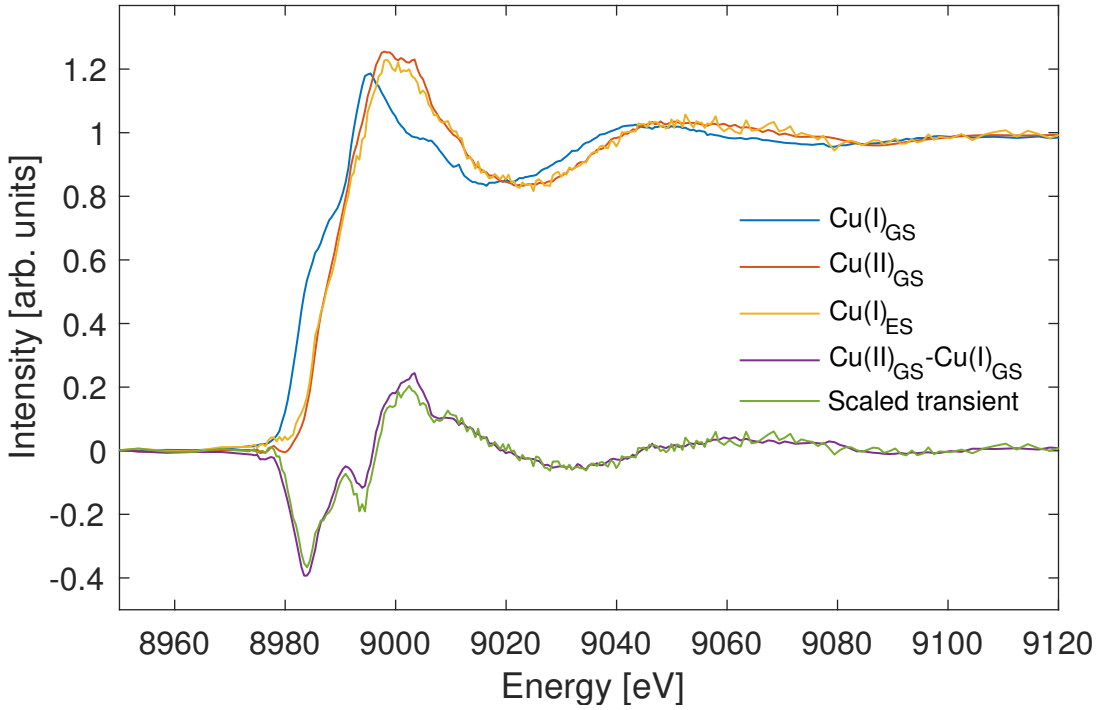

Figure 4.14: Normalized XANES spectra of the ground state of the Cu(I), Cu(II) and the optically excited state of the Cu(I) compounds together with the ground state difference spectrum Cu(II)-Cu(I) and the scaled experimental transient between the laser pumped (not shown here) and the ground state spectrum of Cu(I). The excitation wavelength is 343 nm. The experimental transient was scaled to best match the difference spectrum.

The spectrum for the excited state is calculated from the ground state spectrum and the experimental transient according to the equation [69]:

$$Cu(I)_{ES} = Cu(I)_{GS} + \frac{tr}{f} \tag{4.1}$$

where tr is the transient difference between the pumped and the ground state spectra and f is the fraction of the optically excited molecules in the pumped spectrum. The

value of the excited state fraction f is estimated by scaling the experimental transient to the theoretical one calculated as a difference between the ground state spectra of the Cu(II) and Cu(I):

$$tr_{theor,100\%} = Cu(II)_{GS} - Cu(I)_{GS} \tag{4.2}$$

The theoretical transient spectrum represents the case, where all molecules are switched from the Cu(I) to the Cu(II) oxidation state and the excited state fraction value is equal to 1. The quality parameter χ^2, that describes discrepancy between the theoretical and the experimental transients is defined as:

$$\chi^2 = \left(tr_{theor,100\%} - \frac{tr}{f}\right)^2 \tag{4.3}$$

The dependence of the χ^2 parameter, plotted as a function of the excited state fraction is presented in fig. 4.15. From this dependence we find that the excited state fraction is ~ 0.1.

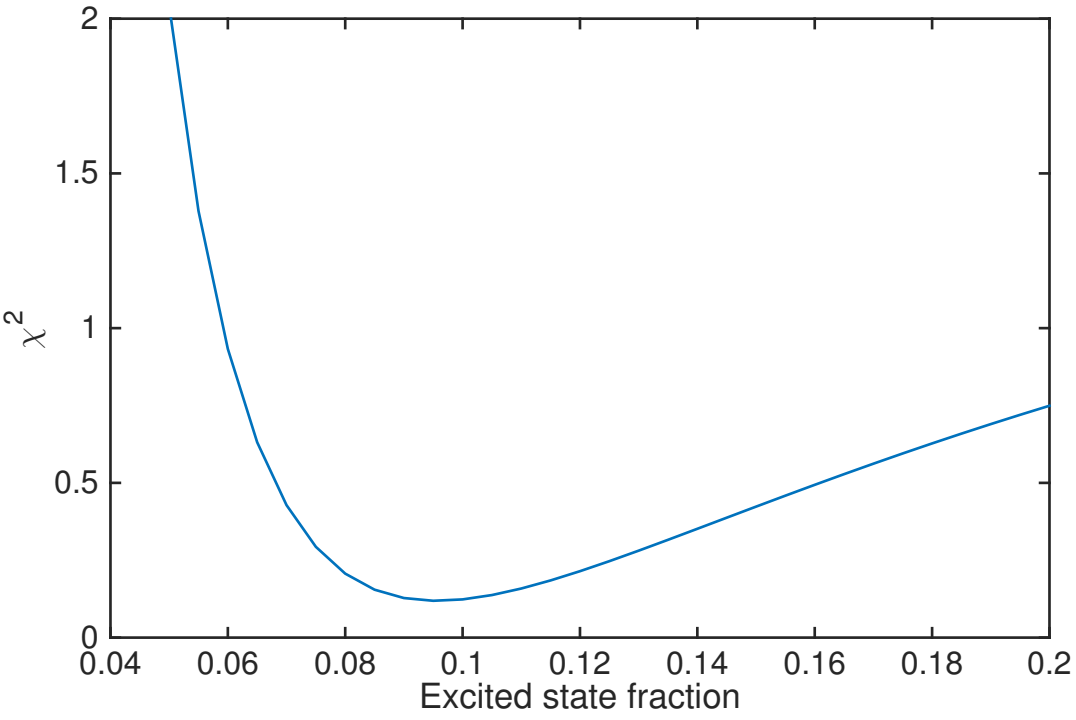

Figure 4.15: Extraction of the excited state fraction, at which the best agreement between the theoretical 100% transient and a scaled experimental one is obtained. The quality parameter χ^2 is calculated according to the equation 4.3.

As can be seen from fig. 4.14 and fig. 4.15, correct scaling of the experimental transient makes it almost perfectly equal to the theoretical one, thus confirming a strong structural and electronic similarity between the Cu(II) and the optically excited Cu(I) complexes.

The absorption edge for both species is shifted by approximately 2.5 eV towards higher energies with respect to the ground state Cu(I) spectrum. Both spectra show 8978 eV peak, which is associated with the $1s \rightarrow 3d + 4p$ transitions [1], that are partially allowed due to mixing of the $3d$ and $4p$ orbitals. All this confirms the oxidation state of the central Cu atom being +1 with $3d^{10}$ configuration for the Cu(I) reactant and +2 with $3d^9$ configuration for the Cu(II) and excited Cu(I).

4.2.2 Natoli's rule

The post-edge region of the spectra in fig. 4.14 shows a blue shift of the first maximum of the EXAFS oscillations. This is associated with the change in the coordination around the Cu atom and can provide an insight onto Cu-N bond distances in the ground and excited states. As discussed in section 2.3, EXAFS oscillations arise when a interference of the outgoing and back reflected electron waves takes place. The difference in energy between the maximum of the EXAFS peak and the absorption edge reflects the distance from the absorber atom to its neighbours from which the photoelectron was back reflected. A rule that allows to quantify this was proposed by Natoli [70, 71]. According to this rule, energy difference between the EXAFS peak position E_r and the abosrption edge E_0 multiplied by the square of the radius of the corresponding coordination shell is constant:

$$(E_r - E_0) * R^2 = const \tag{4.4}$$

For our case of two compounds Natoli's rule can be written as:

$$(E_{r,Cu(I)_{GS}} - E_{0,Cu(I)_{GS}}) * R^2_{Cu(I)_{GS}} = (E_{r,Cu(I)_{ES}} - E_{0,Cu(I)_{ES}}) * R^2_{Cu(I)_{ES}} \tag{4.5}$$

For the $\mathrm{Cu(I)_{GS}}$ spectrum, E_r was defined as the maximum of the resonance peak. For the $\mathrm{Cu(I)_{ES}}$ the maximum of the resonance peak can be defined with a huge uncertainty and this will affect the estimation of the Cu-N bond length. Therefore, the approach was to calculate the energy difference ΔE between both resonance peaks and use the relation:

$$E_{r,Cu(I)_{ES}} = E_{r,Cu(I)_{GS}} + \Delta E \tag{4.6}$$

In order to calculate the energy difference ΔE, a series of the blueshifted $\mathrm{Cu(I)_{GS}}$ spectra with a varying amount of the energy shift were generated and the quality of their spectral overlap with the $\mathrm{Cu(I)_{ES}}$ in the region of the EXAFS resonance peak was estimated. The quality of the spectral overlap χ^2 for each value of the energy shift of the $\mathrm{Cu(I)_{ES}}$ spectrum is calculated as:

$$\chi^2 = \Big(Cu(I)_{ES} - Cu(I)_{GS}\Big)^2 \tag{4.7}$$

The results of the application of this procedure are presented in fig. 4.16. The ideal overlap between both spectra is obtained at ΔE=4 eV and this value was taken for further

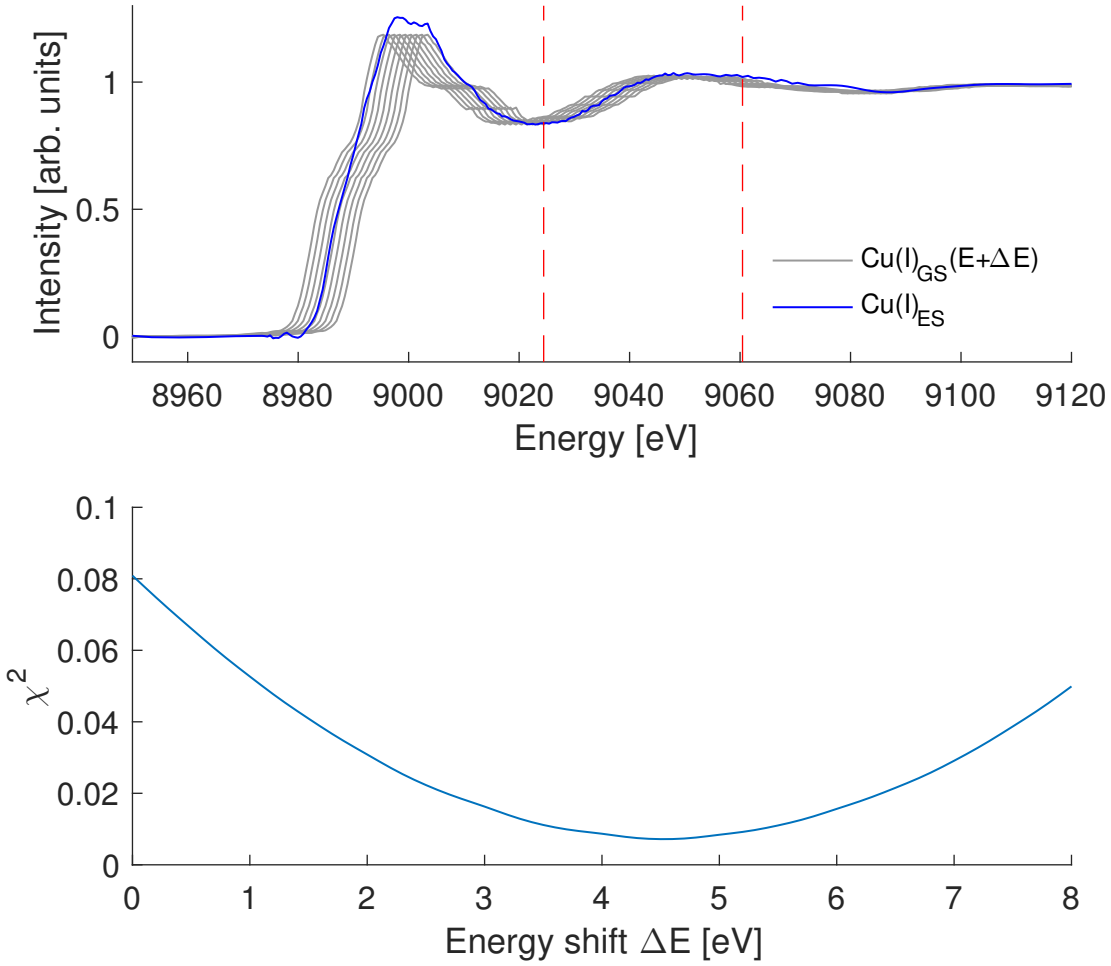

Figure 4.16: (top) Graphical representation of the calculation algorithm used to evaluate the difference in energy ΔE between the first maxima of the EXAFS oscillations between the $Cu(I)_{GS}$ and the $Cu(I)_{ES}$ compounds. A series of the blueshifted $Cu(I)_{GS}$ spectra with a varying amount of the energy shift were generated and the quality of the spectral overlap between each shifted $Cu(I)_{GS}$ spectrum and the $Cu(I)_{ES}$ spectrum is estimated. (bottom) Minimum in the dependence of the χ^2 parameter that describes discrepancy between the $Cu(I)_{GS}$ and the $Cu(I)_{ES}$ spectra in the energy region between the dashed vertical lines from the top figure.

calculations. The edge energies $E_{0,Cu(I)_{GS}}$ and $E_{0,Cu(I)_{ES}}$ were taken as the maxima of the first derivative of the corresponding absorption spectrum.

By applying Natoli's rule (4.5), we get 1.7% shortening of the Cu-N bond in the excited state, with an absolute value of the contraction of 0.032 Å if a crystallographic value for the Cu-N bond length of 2.017 Å for the ground state of Cu(I) is assumed [11]. According to density functional theory (DFT), HOMO of the ground state Cu(I) complex has an

anti-bonding character and the excitation of the electron to the π^* orbital of the quinoline ligand should increase the Cu-N bond strength and lead to a bond contraction. A more precise evaluation of the bond length change is done with the EXAFS fitting in the following section.

Table 4.4: Comparison of the averaged Cu-N bond length in the ground and optically excited state of the Cu(I) molecule. The ground state bond length is obtained from X-ray diffraction measurements [11]. The bond length in the excited state is extracted by applying Natoli's rule.

	E_0 [eV]	E_r [eV]	R_{Cu-N} [Å]
Cu(I) GS	8982.5	9043.5	2.024
Cu(I) ES	8985.0	9048.0	1.992

4.2.3 EXAFS anaylsis

The EXAFS analysis of the ground state and the optically excited Cu(I) spectra was performed with the Artemis software [72, 73], that includes the FEFF package [74]. As an input for the FEFF calculation, crystallographic structures for the Cu(I) and the Cu(II) species were used. The Artemis fitting model for the ground state Cu(I) includes all scattering paths with the effective length $R_{eff} < 4.9\,\text{Å}$, and the excited Cu(I) model includes all paths with $R_{eff} < 3.4\,\text{Å}$. The scattering paths are grouped according to their R_{eff}. The first coordination shell includes four nearest N atoms, that coordinate the central Cu atom. The second coordination shell includes carbon atoms with $R < 3.0\,\text{Å}$. The third shell includes all atoms with $3.0 < R < 4.0\,\text{Å}$. For the ground state Cu(I) model, a fourth shell is added with paths that have $R_{eff} > 4.0\,\text{Å}$. Each shell is assigned with its own Debye-Waller factor σ and the correction to the shell radius ΔR. Other parameters, that are common for all paths in the fitting model are the amplitude scaling factor S_0 and the energy shift ΔE. The wavevector range in k-space for the Fourier transform is set to $2\,\text{Å}^{-1} - 8\,\text{Å}^{-1}$. The amount of the independent fitting parameters for this wavevector range, allowed by the software is limited by nine, which is less than what is required for the GS Cu(I) model that includes relatively long scattering paths. Therefore, the amplitude scaling factor for this model was manually assigned with different values ranging from 0.8 to 1 and in the end was fixed to 1, yielding the best fit result.
The results of the fit are shown in fig. 4.17 and main fitting parameters are summarized in table 4.5. As can be seen, fits for both species show good agreement to the experimental data in both k and R space. The pronounced shoulders in the EXAFS function $\chi(k)$ for the GS Cu(I) molecule, located at approximately $4.5\,\text{Å}^{-1}$ and $5.5\,\text{Å}^{-1}$ are reproduced, as

well as the peaks of the pseudo radial distribution functions for both compounds.

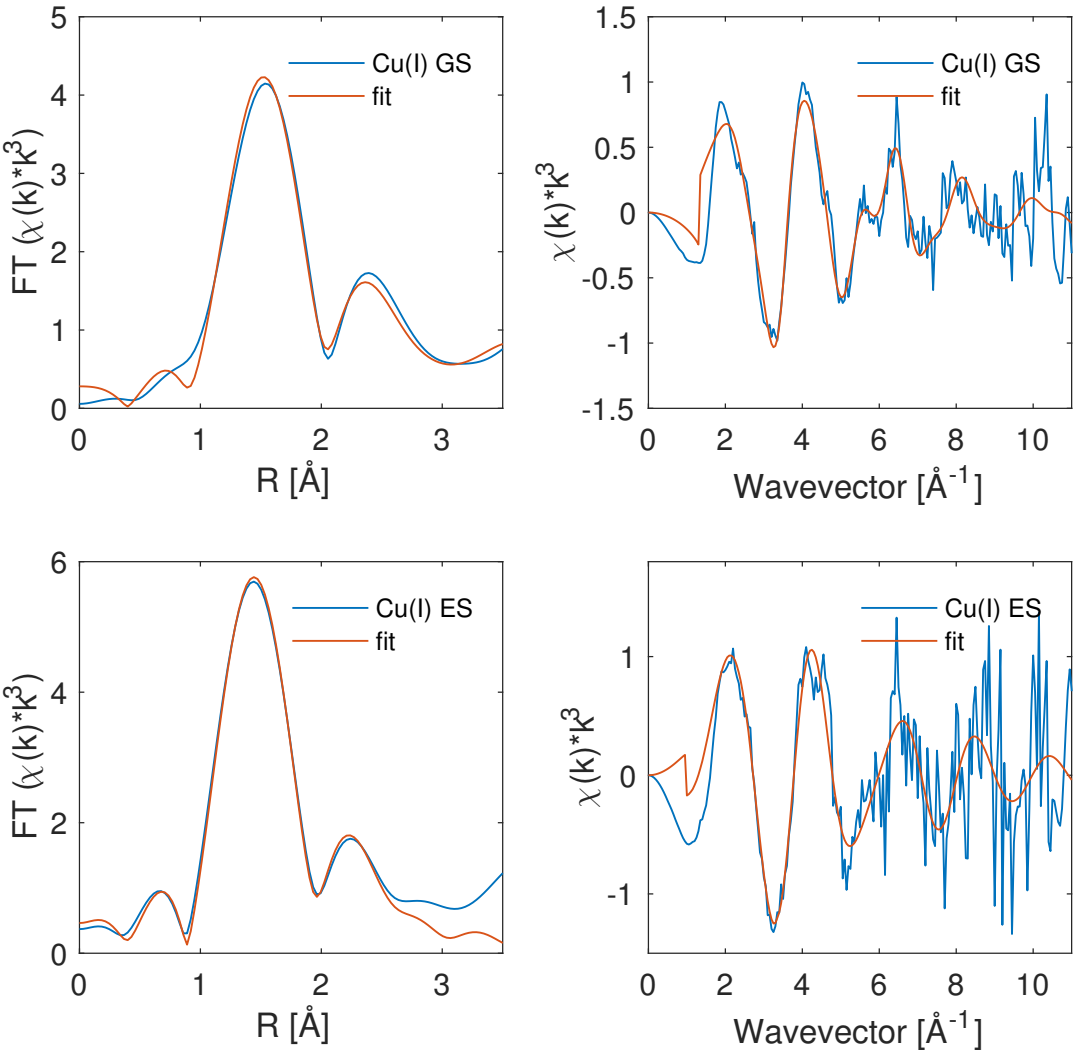

Figure 4.17: Comparison of the EXAFS fitting results of the ground state of the Cu(I) molecule (top row) and its optically excited state (bottom row). The fitting is performed in R-space within the range from $3\,\text{Å}^{-1}$ to $8\,\text{Å}^{-1}$. The figure is adapted from [68].

All values of the structural and non-structural parameters from the EXAFS fitting are in the physically meaningful range and a good agreement between the Debye-Waller factors for both species is obtained. The obtained values for the correction of the first coordination shell radius yield 0.07 Å bond length contraction for the excited state with respect to the ground state of the Cu(I) complex. The value of the bond length contraction is in good agreement with the DFT calculation that suggest averaged Cu-N distance contraction of 0.085 Å [68]. In addition, general fact that the excited Cu(I) spectrum can be

fit with the crystallographic structure of the Cu(II) molecule again confirms the MLCT character of the optically generated Cu(I) excited state.

Table 4.5: Summary of the main structural and non-structural parameters for the EXAFS fitting of the ground and the optically excited state of the Cu(I) molecule.

	S_0	ΔE [eV]	ΔR_1 [Å]	σ_1 [Å^2]
Cu(I) GS	1	6.56	-0.015	0.0063
Cu(I) ES	1	3.73	-0.015	0.0054

It is worth pointing out that the Artemis fitting algorithm does not consider the experimental errorbars for individual data points in the $\chi(k)$ spectrum when evaluating the fit quality parameter χ^2. Even if the measurements are performed in a way that the data quality is the same for all data points, k^2 or k^3 weighting of the EXAFS function $\chi(k)$ results in the same weighting of the error bars and makes them increase as a quadratic or cubic function of the wavevector k. This can be seen in fig. 4.17, where the noise in the region of high k-values is drastically higher compared to the noise in the region of low k-values. A solution to this would be to modify the fitting algorithm so that it performs a proper weighting and accounts for the noise of the individual data point.

4.2.4 Relaxation dynamics

The temporal resolution of the time-resolved experiment at the PETRA III synchrotron is limited by the X-ray pulse duration, which is on the order of 100 ps. This makes only the relatively long-lived excited states of the Cu(I) molecule accessible at PETRA III. Therefore, time-dependent X-ray fluorescence data can be used complementary to other measurement techniques like time-resolved optical fluorescence or pump-probe UV/VIS spectroscopy to proof and more carefully interpret their results.
The relaxation dynamics of the XAS transient signal has been measured at the energy of 8984 eV, at which the intensity of the transient signal is the highest. According to the theoretical predictions by the DFT and to UV/VIS and Infrared (IR) absorption spectroscopy measurements [68], 343 nm laser excitation of the Cu(I) complex brings it to a high-energy singlet state, which relaxate through a sequence of intermediate states to a lower lying triplet ^{3}MLCT state with a quantum yield of about 0.5. The relaxation to the triplet state takes place within less than 20 ps and this state is directly accessed by the K-edge XAS. Theory suggests two further decay channels from the triplet state: first one is the direct relaxation to the singlet ground state S_0 and the second one is the the formation of the solvent exciplex, which subsequently decays to the ground state S_0

with a larger time constant than the ^{3}MLCT state. The above described energy scheme is presented in fig. 4.18. According to the energy scheme and under the assumption that $\tau_{4a} << \tau_{4b}$, τ_5 a decay model for a transient signal can be written as [68]:

$$tr(t) = a_1 e^{-t/\tau_{4a}} + a_2 \frac{\tau_{4a}}{\tau_{4b}} (e^{-t/\tau_5} - e^{-t/\tau_{4a}}) \tag{4.8}$$

where τ_{4a}, τ_{4b} and τ_5 are the decay components, shown in fig. 4.18, and a_1 and a_2 are their amplitudes.

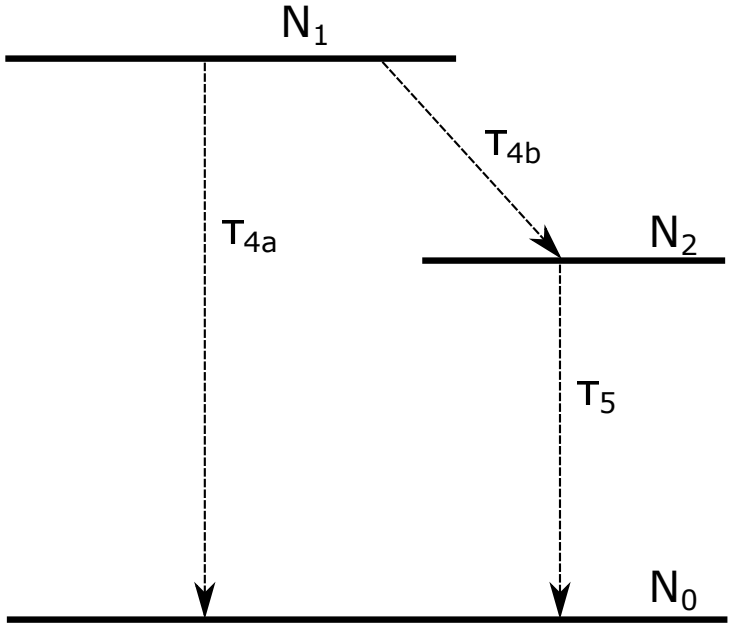

Figure 4.18: Schematic representation of the decay channels from the triplet state to the singlet ground state of the Cu(I) molecule, after the optical pumping into the MLCT band. N_1, N_2 and N_0 are the populations of the triplet, exciplex and the ground state, respectively. Either a direct decay from the triplet to the ground state or a decay thorugh the intermediate exciplex state is possible. The figure is adapted from [68].

The decay model contains five fitting parameters and given the size of the errorbar of the time-dependent XAS data, equally good fits could be produced for different combinations of the fitting parameters. Therefore, a decision was made to fix the τ_{4a} component to be equal to 120 ps, as suggested by the transient UV/VIS and IR absorption measurements. Further deconvolution was performed using the transient fluorescense data, collected at 510 nm emission, as it essentially describes the same process as XAS, but provides better signal/noise ratio and guarantees that no radiation damage can be made to the sample due to low incident laser flux used to excite the fluorescence. The overlap of the transient XAS and time-resolved fluorescence signals is shown in fig. 4.19 and the decay constants obtained from the fitting routine are summarized in table 4.6.

As can be seen, there is a very good agreement between the transient XAS and fluorescence data, especially in the range up to 1 ns. For the delay times above 1 ns, transient XAS shows slightly higher transient values compared to luminescence, which can be assigned to radiation damage effects by either intense laser pump beam or the probe X-ray beam itself.

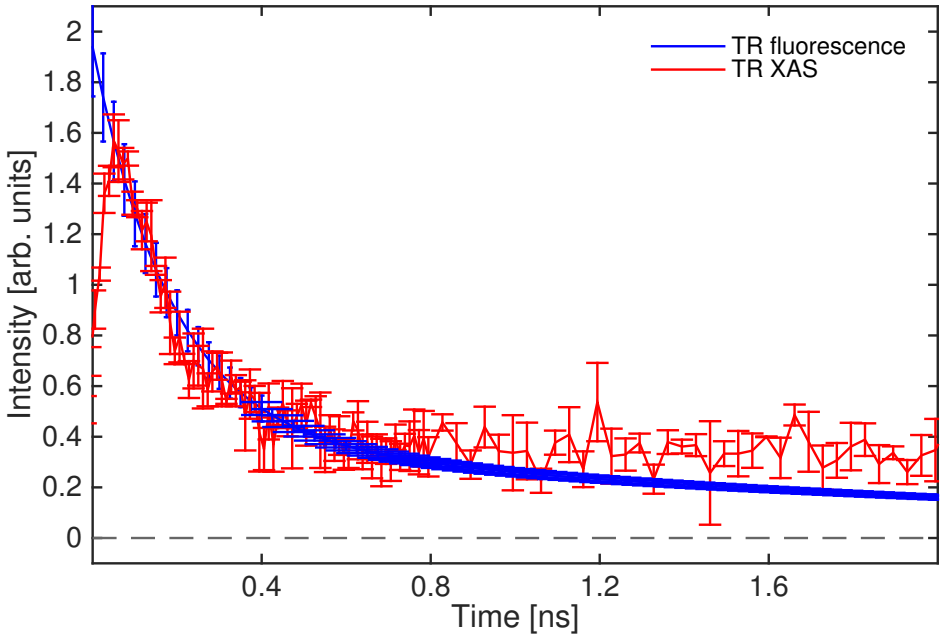

Figure 4.19: Time dependencies of the transient signals, obtained from the XAS and fluorescence measurements. The XAS transient signal was measured at 8984 eV under laser excitation at 343 nm. The transient fluorescence measurements were performed at 510 nm emission wavelength and under 410 nm excitation. The figure is adapted from [68].

Table 4.6: Summary of the time constants, obtained from the deconvolution of the time-resolved fluorescence measurements at 510 nm emission wavelength and 410 nm pump wavelength. The value of the τ_{4a} was set to 120 ps during the fit routine, suggested by the transient UV/VIS and IR measurements.

τ_{4a} [ps]	τ_{4b} [ps]	τ_5 [ps]
120	1222±40	1876±76

4.2.5 Conclusions

By using the pump-probe X-ray absorption spectroscopy at the Cu K-edge with optical pumping at 343 nm, we successfully confirmed presence of the metal-to-ligand charge transfer transition with subsequent change in the oxidation state of the copper atom from +1 to +2. By comparison of the experimental and theoretical transient signals it was shown that the optically excited state of the Cu(I) complex is similar to the ground state of the Cu(II). Theoretically predicted structural changes around the copper atom after the optical excitation were confirmed by applying Natoli's rule and performing a EXAFS analysis. The obtained value for the shortening of the Cu-N bond of 0.07 Å matches the theoretically predicted average shortening of this bond of 0.085 Å.

The relaxation dynamics after optical pumping were studied by the decay of the XAS transient signal and compared to the decay of the optical fluorescence signal. The deconvolution with the model with three decay components allowed to extract the characteristic relaxation times for the system that span a range of more than one order of magnitude from 120 ps to 1876 ps.

4.3 Core level electron binding energies of the $Cu(DMEGqu)_2$ complex

In this section the results on the studies on the $Cu(DMEGqu)_2$ complex, that is structurally very similar to $Cu(TMGqu)_2$ are presented. The $Cu(DMEGqu)_2$ samples in a from of polycrystalline powder are stable under vacuum conditions and therefore allow conducting the X-ray photoelectron spectroscopy measurements. Core level electron binding energies from the nitrogen atoms of the complex are the important parameter that may allow to better understand how the charge redistributes within the molecule upon a change in the oxidation state of the central copper atom. In addition, these binding energies are needed to support further planned XAS measurements at K-edge of nitrogen. Within this section the $[Cu(DMEGqu)_2]^+$ will be referred to as Cu(I) and $[Cu(DMEGqu)_2]^{2+}$ will be referred to as Cu(II).
The elementary composition of the Cu(I) and Cu(II) powders is validated via the survey XPS scan in the range of binding energies from 0 to 1200 eV. The survey spectra of both species are presented in fig. 4.20.

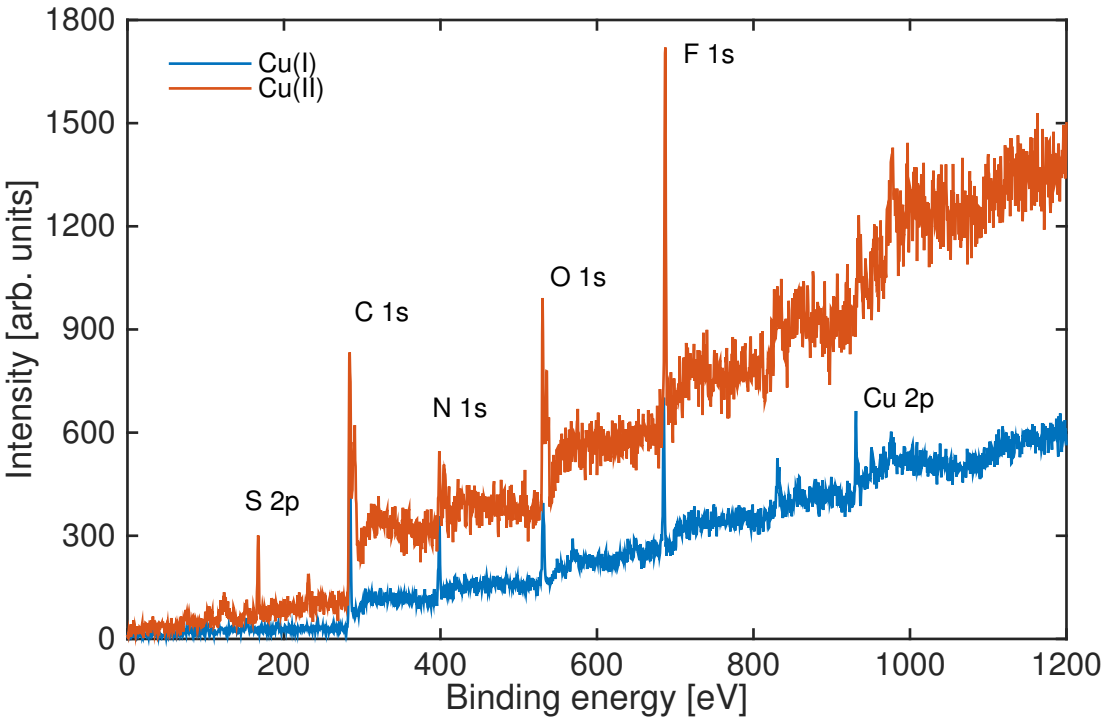

Figure 4.20: Comparison of the survey XPS spectra of the Cu(I) and Cu(II) powders. Al K_α line used for the excitation.

The measurements show intense C 1s, Cu 2p and N 1s as well as O 1s photoelectron peaks, showing dominant presence of carbon, copper, nitrogen and oxygen atoms, in

accordance with the chemical formula of the complex [31, 67]. The oxygen could have adhered to the samples surface during the transfer of the sample to the experimental chamber. After the survey measurement, a more precise measurement of the XPS lines of copper and nitrogen was conducted.

Cu $2p$ XPS spectra of both compounds are presented in fig. 4.21. The positions of the $2p_{1/2}$ and $2p_{3/2}$ lines obtained from the deconvolution of the spectra are given in table 4.7. The individual XPS peak in the deconvolution model is represented by a Gaussian function:

$$f_{G,i}(E, A_i, \sigma, E_{B_i}) = \frac{A_i}{\sigma_i \sqrt{2\pi}} \exp\left(\frac{E - E_{B_i}}{2\sigma_i^2}\right) \tag{4.9}$$

where, A_i and E_{B_i} are the amplitude and the binding energy for the i-th peak and σ_i defines its width.

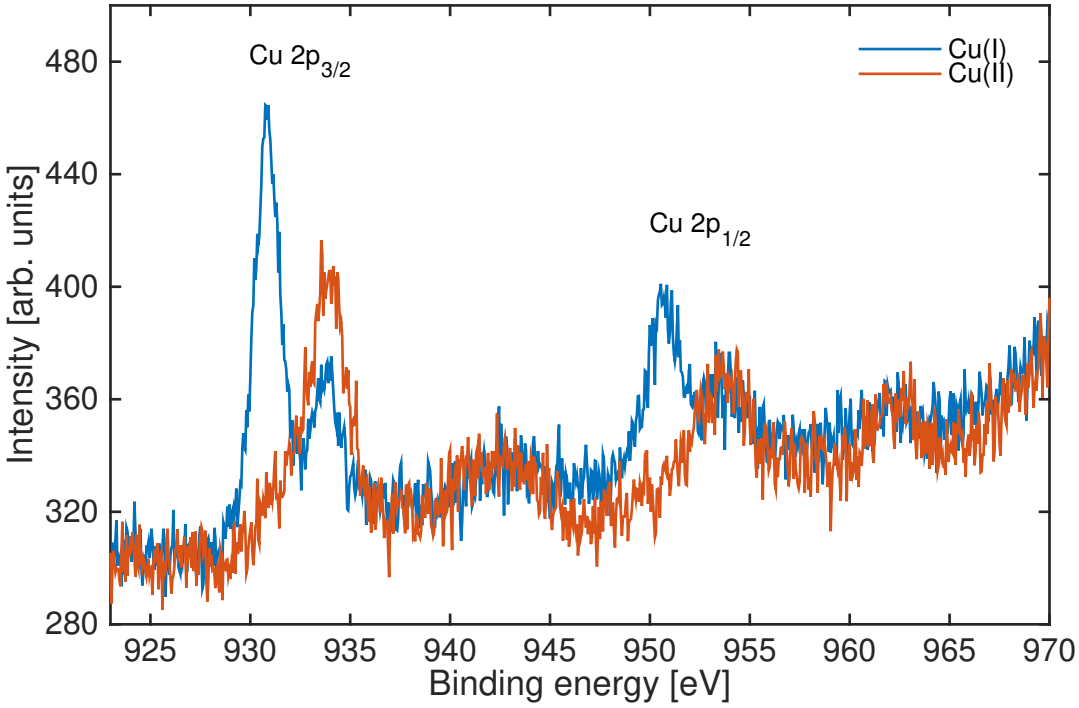

Figure 4.21: Cu $2p$ XPS spectra of the Cu(I) and Cu(II) powders. Appearance of the shake-up satellites as well as the shift of the $2p_{1/2}$ and $2p_{3/2}$ peaks of the Cu(II) sample compared to the Cu(I) indicate different oxidation states of the Cu atom in both compounds.

As can be seen, the Cu(II) spectrum exhibits two main peaks located at the energies of 933.9 eV and 953.9 eV. These peaks emerge due to ionization of the $2p_{3/2}$ and $2p_{1/2}$ energy levels of Cu. Each peak is accompanied by a broad satellite feature on the high binding energy side. The first satellite covers the energy range from approximately 940 eV to 946 eV and the second satellite feature covers the energy range from 960.5 eV to 964.5 eV.

For the Cu(I) complex, the $2p_{1/2}$ and $2p_{3/2}$ lines are located at lower binding energies, confirming lower oxidation state of the central Cu atom in this complex [37]. In addition, comparison of the Cu(I) and the Cu(II) spectra (fig. 4.21) shows that Cu(I) compound has Cu(II) inclusion, probably due to oxidation during transfer of the sample to the XPS spectrometer. Cu(II), in its turn, is more stable in the oxygen environment and is unlikely to further change its oxidation state to the Cu(III).

Table 4.7: Peak positions of the Cu $2p_{1/2}$ and Cu $2p_{3/2}$ lines of the Cu(I) and the Cu(II) samples obtained from the deconvolution of the spectra.

	$2p_{3/2}$ [eV]	$2p_{1/2}$ [eV]
Cu(I)	930.8	950.6
Cu(II)	933.9	953.9

The FWHM of the Cu $2p$ photoelectron peaks, obtained from the deconvolution is 1.6 eV for the Cu(I) complex and 2.4 eV for the Cu(II) complex, also confirming different oxidation states of copper in both complexes. The difference in FWHM can be explained if a multiplet splitting in the final state after the photionization is considered [33, 34]. Cu(I) has a $3d^{10}$ electron configuration in the ground state, which corresponds to the $^1S_0$ spectroscopic term in atomic notation. Upon ionization of the $2p$ electron, electron configuration changes to $2p^5 3d^{10}$ and two distinct final states of the atom are possible: $^2P_{1/2}$ and $^2P_{3/2}$, depending on whether $2p_{1/2}$ or $2p_{3/2}$ electron level is ionized. The kinetic energy of the emitted photoelectron equals to the difference in energies of the initial and final relaxed state of the ion. Under the "final relaxed state" the following is meant: immediately after photoionization the state of the system is not the eigenstate of the Hamiltonian of the newly formed ion. Remaining electrons have to adjust to the new core potential and collapse towards the core hole. Additional energy, that is released is imparted to the outgoing photoelectron. The situation is different with the Cu(II) that is paramagnetic and has incomplete $3d$ shell with $3d^9$ electron configuration. Upon photoemission, $2p^5 3d^9$ configuration is formed and it gives rise to a series of terms of different multiplicity, depending on the relative alignment of the spins of the core and $3d$ holes. These states have different energies, and the energy difference between them (magnitude of the multiplet splitting) is proportional to the interaction between the magnetic momenta of $2p$ and $3d$ electrons. The multiplet splitting is considered to be a reason for the broadening of the $2p$ peaks of the Cu(II) atom, compared to the Cu(I) [34].
Another distinct evidence of the presence of unpaired electrons in the valence shell is the formation of the shake-up satellites. As mentioned above, the rest of the energy that is released when electrons screen a newly formed core hole, can be imparted to the outgoing photoelectron. Another option is to use this energy to promote one of the valence

electrons to a higher energy level. Such a transition should obey momentum conservation rules with $\Delta L = \Delta S = 0$, meaning that total angular and spin momenta of the ion should be conserved [33]. Under the asumption of a weak interaction of the valence electrons with the core hole, this rule can be relaxed to [33]:

$$\Delta L_V = \Delta S_V = 0 \tag{4.10}$$

where L_V and S_V correspond to the valence shell only. Applying this rule we see that there are no transitions that can fulfill it if there are only paired electrons in the valence shell. For the Cu(II) with $3d^9$ electronic configuration and $t_2^6e^3$ ground state in an octahedral ligand field, transitions $t_2^6e^3 \rightarrow t_2^6e^2 4s$ could become partially allowed, giving rise to the shake-up peaks in the XPS spectrum [33].
In order to deconvolute the N $1s$ XPS spectra of the studied compound, a proper mathematical model is needed, because there are chemically inequivalent nitrogen sites within the molecule. According to the molecular structure, there are two identical ligands per each Cu(DMEGqu)$_2$ molecule [67]. Each ligand contains two chemically identical outer *Amine* nitrogen atoms (N_{amine}) and two nitrogen atoms (*Quinoline* and *Guanidine*), that coordinate copper atom: N_{qui} and N_{gua}. In addition, Cu(II) powder contains extra solvent molecule CH_3CN per each sample molecule. The resulting physical model for the deconvolution of the nitrogen $1s$ XPS spectra of the studied compounds consist of three gaussian peaks with intensity ratios 4:2:2 for the Cu(I), reflecting the stoichiometry $N_{amine} : N_{qui} : N_{gua}$. For the Cu(II), the model has an extra peak, representing the nitrogen atom from the solvent N_{solv}. The intensity ratios are 4:2:2:1 for $N_{amine} : N_{qui} : N_{gua} : N_{solv}$. The gaussian function for individual peak is written in the form of equation (4.9). All gaussian components of a given molecule have the same FWHM. The presence of the Cu(II) in Cu(I) powder is also taken into account. This is done by adding the Cu(II)-related peaks to the fit model of the Cu(I) compound with the intensity ratio, defined from the Cu $2p$ spectrum. In summary, the deconvolution procedure consists of the following steps:

- Deconvolution of the Cu $2p_{3/2}$ XPS spectrum of the Cu(I) complex (fig. 4.21) and extraction of the surface areas of the peaks, related to the Cu(I) and Cu(II) components ($S(2p_{3/2,\mathrm{Cu(I)}})$ and $S(2p_{3/2,\mathrm{Cu(II)}})$ correspondingly). The Cu(II)/Cu(I) inclusion ratio R in the Cu(I) sample is estimated as $S(2p_{3/2,\mathrm{Cu(II)}})/S(2p_{3/2,\mathrm{Cu(I)}})$.

- Deconvolution of the nitrogen $1s$ XPS spectrum of the Cu(II) complex with a four-peak model: $f_{Cu(II)}(E) = f_{Cu(II),amine} + f_{Cu(II),qui} + f_{Cu(II),gua} + f_{Cu(II),solv}$

- Exclusion of the solvent-related peak from the fit result
$f^{final}_{Cu(II)}(E) = f_{Cu(II),amine} + f_{Cu(II),qui} + f_{Cu(II),gua}$

- Deconvolution of the Nitrogen 1s XPS spectrum of the Cu(I) complex with a model function $f_{Cu(I)}(E) = f_{Cu(I),amine} + f_{Cu(I),qui} + f_{Cu(I),gua} + Rf^{final}_{Cu(II)}(E)$

The value of R is estimated to be 0.36. The deconvoluted spectra of the Cu(I) and Cu(II) compounds are presented in fig. 4.22. The values for the N 1s binding energies, extracted from the fit are summarized in table 4.8.

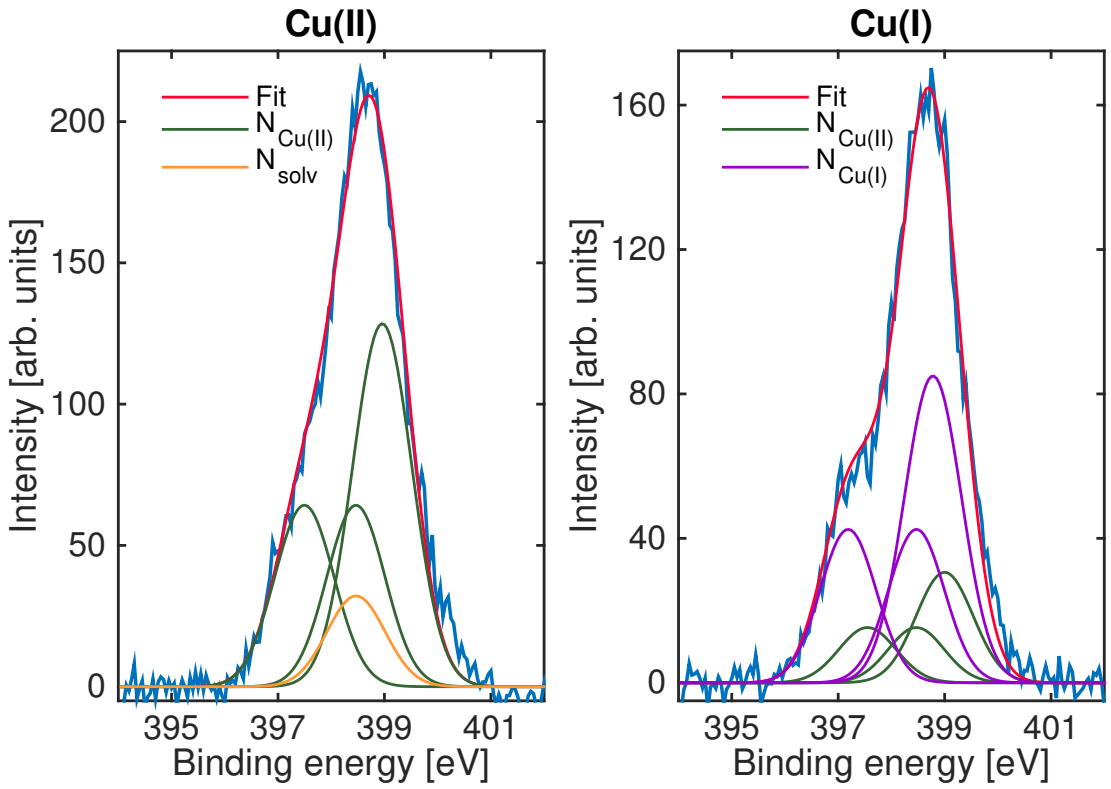

Figure 4.22: Deconvolution of the N 1s XPS spectra of the Cu(I) and Cu(II) compounds. The presence of one additional N atom from the solvent molecule per each Cu(II) molecule and the presence of the admixture of the Cu(II) species in the Cu(I) powder is taken into account.

As can be seen, fitting suggest that the core line peaks of the outer N_{amine} atoms are at higher binding energies, compared to the N_{qui} and N_{gua}, corresponding to the lower electron density on N_{amine}. This might seem contradictory, because each N_{amine} donates three 2p electrons to form a σ-bond with three neighbouring carbon atoms, but its 2s electron pair does not participate in chemical bonding. On the other hand, N_{gua} and N_{qui} donate not only all their 2p electrons, but also 2s pair to form chemical bonds with neighbouring carbon atoms and the central copper atom. Therefore, a lower electron density and correspondingly higher binding energies for N_{qui} and N_{gua} could be expected. The fact that the binding energies of N_{qui} and N_{gua} are lower compared to the N_{amine} suggests that the electron density might be attracted from the entire molecule towards the central

copper atom, leading also to an increase of the electron density on N_{gua} and N_{qui} that coordinate it.

Table 4.8: Comparison of the experimental and theoretical binding energies of $1s$ electrons of the N_{amine}, N_{gua} and N_{qui} atoms of the Cu(I) and Cu(II) species.

	N_{gua} [eV]	N_{qui} [eV]	N_{amine} [eV]
Cu(I) fit	397.2	398.5	398.8
Cu(I) theory	397.1	398.4	398.6
Cu(II) fit	397.5	398.4	399.0
Cu(II) theory	397.6	398.5	399.0

According to the values in table 4.8, when the oxidation state of the central copper atom changes from +1 to +2, N $1s$ peaks shift to higher binding energies, indicating a decreased electron density on the nitrogen atoms. This can be explained by the attraction of the charge from the nitrogen atoms towards the copper to provide a better screening of the more positively charged core. The fit results and values of the binding energies for the nitrogen atoms are also supported by the theoretical calculations from Uwe Gerstmann [75].
As a conclusion, XPS measurements on $[Cu(DMEGqu)_2]^+$ and $[Cu(DMEGqu)_2]^{2+}$ powders allowed to validate the elementary composition and to investigate the electronic properties of these complexes. The width and position of the Cu $2p$ XPS lines as well as the presence of broad satellites of these lines confirms the expected oxidation state of Cu atom in both complexes. With the help of the complex deconvolution routine the $1s$ electron binding energies of all nitrogen atoms in the complex were extracted. The obtained results match well to the theoretical calculations and show the distribution of the electron density on nitrogen atoms and the way it changes, when the oxidation state of the central copper atom is changed. The N $1s$ binding energies will be used to support the planned nitrogen K-edge XAS measurements that can provide more insight onto the electronic structure of the studied entatic state compounds.

4.4 Spin crossover phenomenon in $Fe(Pz_2Py)_2$

This section presents the measurement results and analysis of the pump-probe X-ray absorption spectroscopy experiments, performed at the Fe K-edge at the PETRA III synchrotron on the water solvated $Fe(Pz_2Py)_2$ complex. $Fe(Pz_2Py)_2$ is expected to be switchable from low to high spin state via optical excitation. Density Functional Theory predicts significant elongation of the Fe-N bonds when going to the high-spin state. The ground state structure is known from crystallography measurements as well as from DFT calculations and they agree well with each other. The ground state molecular structure obtained from X-ray diffraction experiment [79] is shown in fig. 4.23. The experimentally determined excited state structure has not been reported before.

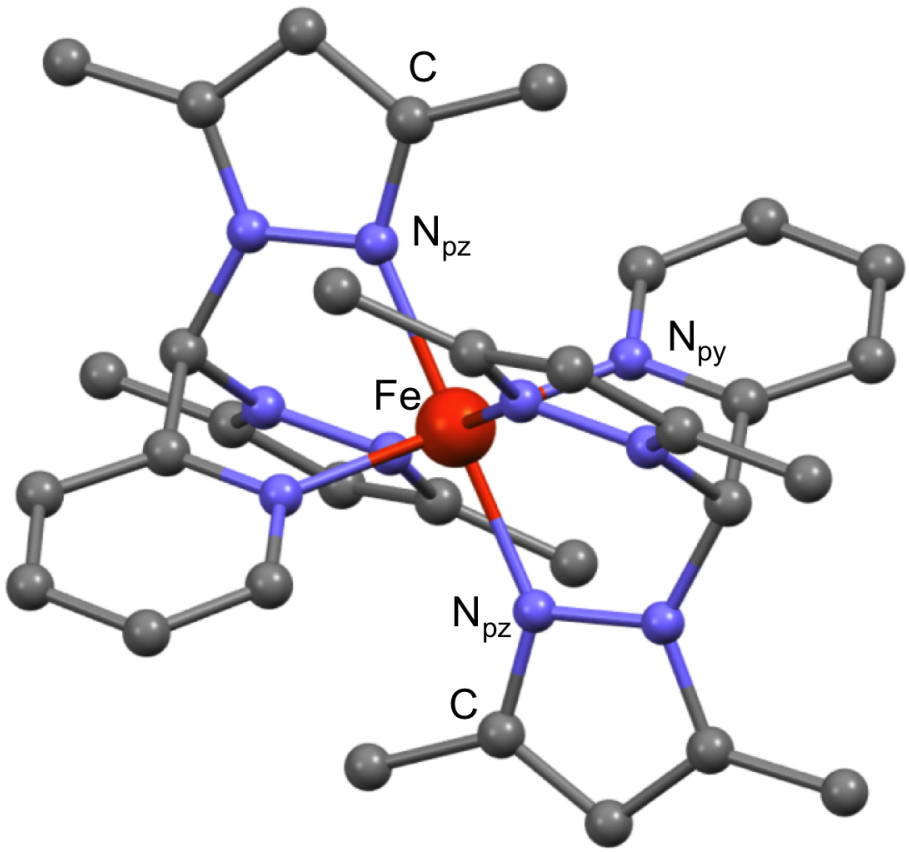

Figure 4.23: Ground state molecular structure of the $Fe(Pz_2Py)_2$ complex, obtained from X-ray diffraction measurements. The central Fe atom is coordinated by two tridentate ligands Pz_2Py.

4.4.1 Transient signal as a function of laser power

At the beginning of the pump-probe XAS experiment dependence of the XAS transient signal on the pump laser power was measured. This dependence is presented in fig. 4.24.

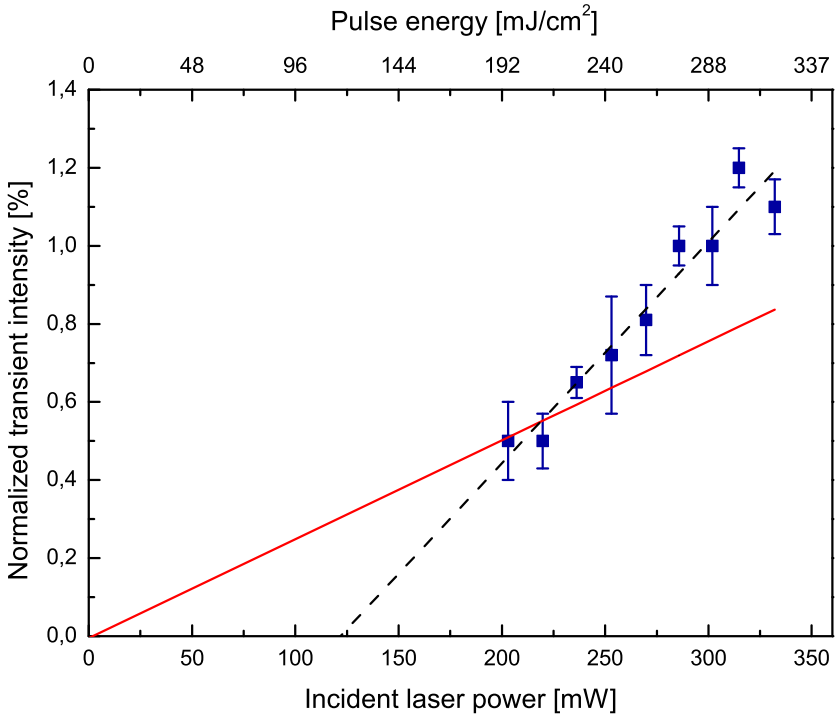

Figure 4.24: Dependence of the intensity of the XAS transient signal, measured at 7124 eV energy and a delay of 50 ps, as a function of the incident laser power. The red solid line is a linear fit to the (0,0) point and first three experimental transient values. The dashed black line is a linear fit to all measured data points. Optical pumping performed at 343 nm.

The laser power was measured with a power meter at the jet position. For each laser power, X-ray fluorescence signals I_{Pumped} and I_{GS} corresponding to the laser ON and the laser OFF states were measured four times each. Afterwards, X-ray transient was defined as:

$$I_{tr} = \frac{I_{Pumped}}{I_{0,Pumped}} - \frac{I_{GS}}{I_{0,GS}} \tag{4.11}$$

where $I_{0,Pumped}$ and $I_{0,GS}$ are the intensities of the incident X-ray beams. The time delay between the pump and the probe pulse was set to 50 ps, the monochromator was set to 7124 eV where the transient intensity is the highest. As can be seen, the intensity of the XAS transient signal can not be fitted with a linear function, that starts at (0,0) point. The line fit to all measured data points (black dashed line on fig. 4.24) intersects the

horizontal axis at 120 mW or 115 mJ/cm^2 correspondingly. There is no clear explanation of the obtained result, but different contributions to it can be considered. First is that a part of the photons incident on the jet will be reflected and scattered, not contributing to the formation of the transient signal and causing a constant offset of the experimental dependence on fig. 4.24 along the horizontal axis. The magnitude of the offset is defined by the optical properties and the surface quality of the jet, as well as the geometry, under which the laser radiation is incident on the jet. However, not more than 10-20% of the incident laser power should be reflected or scattered. The other possible explanation is an overestimation of the incident laser power due to the measurement routine. Prior to the measurement of the transient signal, a power meter was installed at the liquid jet position and the intensity of the output of the laser was increased step wise. The laser power at the jet position was recorded at each output power, allowing to set a correspondence between them. Afterwards, the output power was decreased to the initial value and the liquid jet was turned on, allowing to record the transient signals at different laser powers. If one of the mirrors, that guide the pump laser beam to the liquid jet was damaged by the intense laser beam and lost a part of its reflectivity before the transient signal has been reordered, then the effective laser power at the jet position was less than expected, and this could cause an offset of the data on fig. 4.24. The deviation of the transient signal from the expected linear behavior can also be attributed to either multiphoton absorption processes or thermal damage effects, that result in the dissociation of the molecule or partial evaporation of the liquid jet and causing a higher values of the transient signal.
In order to stay in the range where the responce of the transient signal is linear and multiphoton processes can be excluded, the pump-probe measurements were conducted at the laser fluence of 200 mJ/cm^2.

4.4.2 Data normalization

The initially obtained spectra were normalized to the incident X-ray beam intensity I_0, averaged and rebinned. The rebinning was done so that all data points that are below 7110 eV are averaged in 3 eV windows, points in the region from 7110 eV to 7325 eV are averaged in 1 eV window and all points, that lie above 7325 eV are averaged again in 3 eV window. Afterwards, the ground state and the pumped state spectra were normalized with the Athena software [76]. The normalization procedure consists of the following steps:

- Determination of the threshold energy E_0 as the maximum of the first derivative of the experimental absorption spectrum $\mu(E)$.
- Fitting of a smooth function to the pre-edge and the post-edge regions of the absorption spectrum.

- Normalization of the spectrum to the edge step, defined as the difference between the pre-edge and the post-edge lines at the threshold energy $\Delta\mu(E_0)$. After this step the absorption coefficient is zero in the pre-edge region and oscillates around 1 in the post-edge region.

- Fitting of a cubic spline function to the absorption spectrum, that represents the absorption of an isolated atom $\mu_0(E)$.

- Extraction of the EXAFS oscillation function $\chi(E)$ and transfer to the k-space with a k^n weighting factor, where n=1-3.

After the EXAFS function $\chi(k)$ has been extracted, the structural analysis can be performed. This can be performed either by a direct fitting of the $\chi(k)$ or its Fourier transformation to the R-space and fitting there. Fourier transformation of the $\chi(k)$ is a powerful tool which allows to represent the data in the form of a pseudo radial distribution function $\chi(R)$. Peaks and intensities of $\chi(R)$ correspond with some shift to the average distance from the absorber to the surrounding atoms, their type and quantity. Backward fourier transformation of the selected region of $\chi(R)$ (usually first or first and second coordination shell peaks) yields contribution to the total EXAFS function from these coordination shell only.
The above mentioned steps were applied to the ground state and the pumped state spectra and the results are shown in fig. 4.25. Special care was taken to ensure that both spectra are treated exactly in the same way and no artificial changes will be added to them during the normalization procedure.
A closer look on the near-edge region of the absorption spectrum (fig. 4.25) shows that there are four characteristic features of the spectrum located at energies of 7114 eV, 7124 eV, 7130 eV and 7140 eV as well as the EXAFS peak centered at 7178 eV. The pre-edge feature at 7114 eV is assigned to the dipole-forbidden $1s \rightarrow 3d$ transitions [77].
Indeed, in the octahedral ligand field $3d$ levels are split into two subsets: 3-fold degenerate t_{2g} level with a lowered energy and a 2-fold degenerate e_g level with an increased energy. In the low spin ground state t_{2g} level is fully filled with electrons and e_g level is empty due to the $3d^6$ electron configuration of the Fe(II) ion. Correspondingly, the lowest possible bound-bound transition is $1s \rightarrow 3d(e_g)$ which becomes partially allowed due to orbital mixing of the Fe $3d$ orbitals with ligand $2p$ or Fe $4p$ orbitals. Three other features are usually attributed to multiple scattering effects [78] and therefore they should reflect geometry of the molecule. The transient signal shows that the most prominent changes are taking place at the energy of 7124 eV, where the second spectral feature is located. Additionally, the pumped spectrum shows a shift of the first EXAFS peak towards lower energies, which provides a hint that there is an increase in the radius of the first coordination shell around the Fe atom.

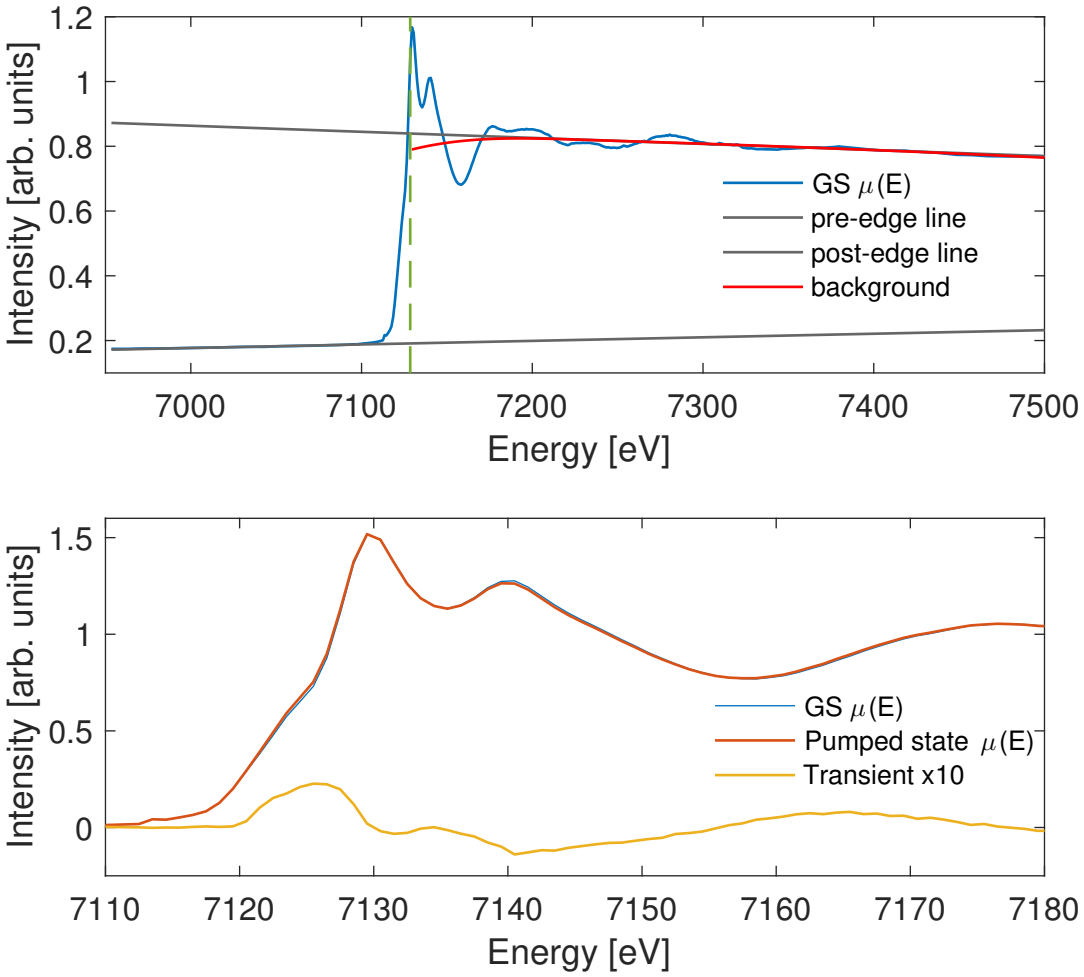

Figure 4.25: (top) Ground state XAS spectrum of the $Fe(Pz_2Py)_2$ compound with the smooth functions, fitted to the pre-edge and the post-edge regions of the spectrum. The red curve represents the simulation of the absorption of an isolated atom. (bottom) A zoom to the XANES region of the ground state and the pumped state spectra of the $Fe(Pz_2Py)_2$ compound together with the scaled experimental transient, calculated as a difference between the pumped and the ground state spectra.

4.4.3 Ground state EXAFS analysis

EXAFS oscillation function contains important structural and non-structural parameters of the studied molecule, and the goal of the fitting is to extract these parameters from experimentally measured data. The fitting is performed by comparison of the experimentally measured EXAFS oscillation function to the theoretical one. The fitting of the ground state spectrum in the present work is performed with the ARTEMIS software which is a part of the IFEFFIT package [72, 73] and includes FEFF code [74]. As discussed in section 2.3, the theoretical EXAFS oscillation function is calculated according

to the following equation:

$$\chi(k) = \frac{S_0^2}{k} \sum_i \frac{N_i e^{(-2\sigma_i^2 k^2)} e^{(-2R_j/\lambda(k))} F_j(k)}{R_j^2} \sin(2kR_j + 2\delta_c + \Phi) \tag{4.12}$$

ARTEMIS software allows convenient parametrization and variation of the structural parameters of the equation, whereas k-dependent scattering amplitudes $F_j(k)$ and phase shifts δ_c are provided by the FEFF calculation and remain constant during the fit. FEFF software requires some initial molecular structure, from which all scattering path from the target atom of the molecule are calculated. As an output, FEFF provides a list of single and multiple scattering paths, ordered according to their effective length. It is then up to the user to select which scattering paths to include in the fit and how to parametrize them, as well as to decide which combination of the parameters from the fit is physically meaningful.

The goal of the ground state fitting is to validate the X-ray diffraction measurements and to extract the Debye-Waller factors σ_i, the amplitude scaling factor S_0 and the overall energy shift of the theoretical spectrum ΔE_0, that will be further used in the simulation of the excited state EXAFS function.

As an input for the FEFF calculation, the molecular structure, obtained from crystallography measurements was used [79]. All scattering paths with effective length below 4.25 Å are taken for the fit. They are split in three groups. The first group represents paths from six coordinating nitrogen atoms, the second group includes all paths with effective length below 3.3 Å and all other paths with $R_{eff} > 3.3$ Å are assigned to the third group. Each group has its own Debye-Waller factor σ and modification of the path length ΔR. The fitting model has eight parameters in total. The fitting is performed in k-space in the range from 2 Å^{-1} to 8 Å^{-1} with a Hanning-type window. The result of the fit is presented in fig. 4.26 and the summary of the fitting parameters is presented in table 4.9. As can be seen, there is a good agreement between the experimental data and the fit, all features of the experimental spectrum are reproduced, though there is some overestimation of the amplitude of the oscillations in the region from 2.5 Å^{-1} to 4.5 Å^{-1}. The amplitude scaling factor matches the values for the other iron-based compounds [80, 81]. In addition, relatively low values of the structural parameters ΔR_1 and ΔR_2 indicate that the the ground state molecular structure obtained from X-ray diffraction experiments matches well to the structural data, obtained from the EXAFS analysis, only the ΔR_3 parameter seems to be slightly overestimated.

The extracted Debye-Waller factors σ_i, the amplitude scaling factor S_0 and the energy shift of the theoretical spectrum ΔE_0 will be further used in the analysis of the excited state spectrum.

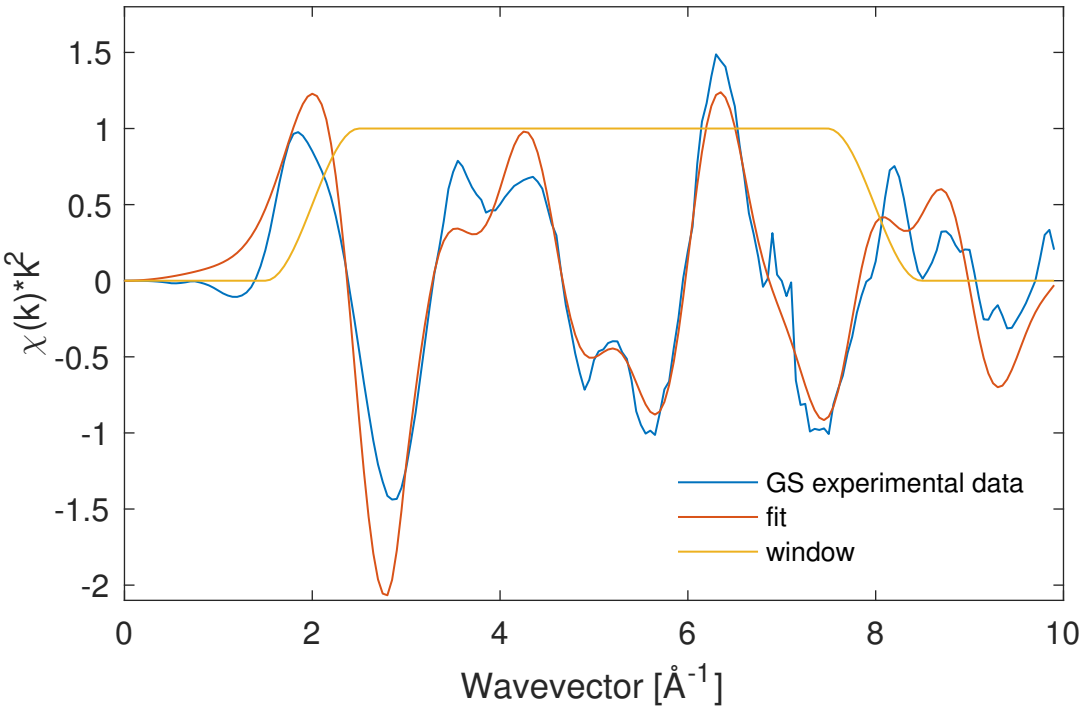

Figure 4.26: Fit of the ground state EXAFS function of the $Fe(Pz_2Py)_2$ molecule. As a starting model for the fit, the structure obtained from X-ray diffraction measurements was used. The yellow box represents the Hanning window that defines the range of the data within which the quality of the fit is estimated during the fitting routine.

Table 4.9: Structural and non-structural parameters, obtained from the fit of the ground state spectrum of the $Fe(Pz_2Py)_2$ molecule. The scattering paths are calculated for the X-ray diffraction structure of the compound. All paths with $R_{eff} < 4.5\,\text{Å}^{-1}$ were included in the fitting model. The value for ΔE is given in eV, the values for all ΔR are given in Å and the values for the Debye-Waller factors are given in Å^2.

S_0	ΔE	ΔR_1	σ_1	ΔR_2	σ_2	ΔR_3	σ_3
0.78	-4.47	-0.014	0.001	-0.029	0.0056	0.051	0.0025

4.4.4 Excited state fraction estimation

In order to reconstruct the XAS spectrum of the excited state, a precise value of the excited state fraction is needed. For a flat jet, the excited state fraction is given by the formula [82]:

$$f = \frac{N_{ph}}{c_{sample} V}\Big(1 - \exp(-c_{sample}\sigma d_{jet})\Big) \tag{4.13}$$

where N_{ph} is the number of photons incident on the jet, V is the volume exposed to laser radiation, c_{sample} is the concentration of the sample, σ is the absorption cross-section at a given wavelength and d_{jet} is the thickness of the jet. The size of the laser spot was measred by a CCD camera, installed at the jet position. The diameter of the laser focus is 45 μm and the laser power, incident on the jet is 192 mW.
A deconvoluted optical absorption spectrum of the $Fe(Pz_2Py)_2$ compound is presented in fig. 4.27.

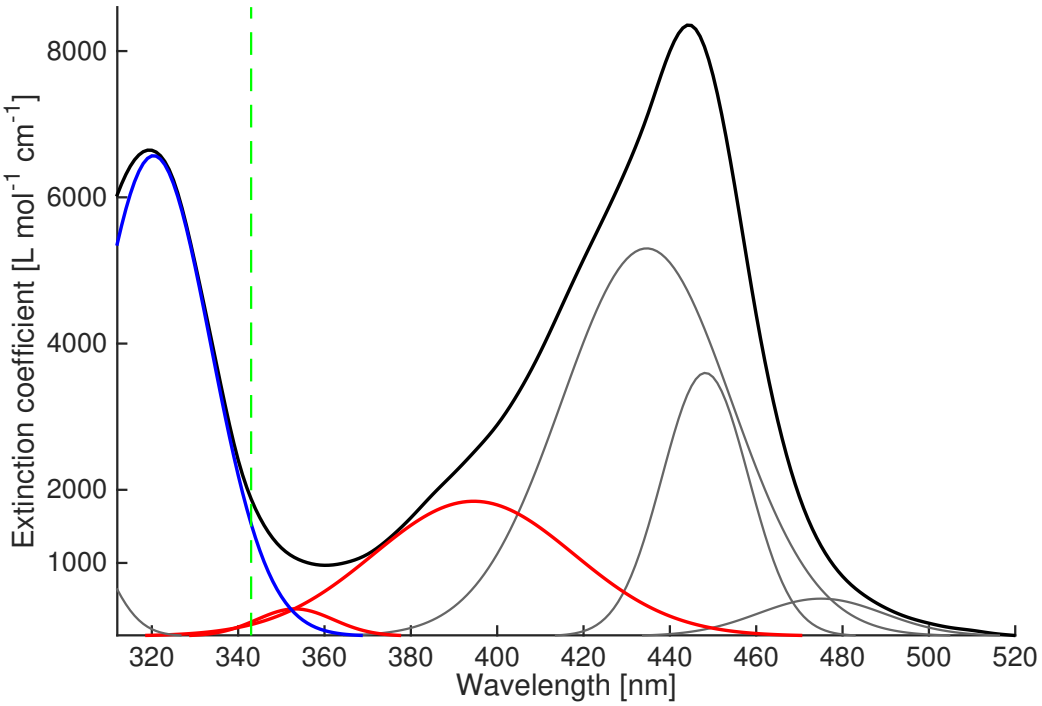

Figure 4.27: UV-Vis absorption spectrum of the $Fe(Pz_2Py)_2$ complex (black) and its deconvolution with a series of the Gaussian functions. The green dashed line shows the pump wavelength of 343 nm. The components of the deconvolution that contribute to the absorption at pump wavelength are marked with blue and red color.

As can be seen, the deconvolution of the spectrum yields three components that contribute to the absorption at the pump wavelength of 343 nm (marked with blue and red colors in the figure). The major contribution (blue line) is the tail of the absorption peak, centered at 320 nm with the value of the absorption of 1550 L mol^{-1} cm^{-1}. The minor contribution of 350 L mol^{-1} cm^{-1} comes from the components of the deconvolution, that are marked with red color. If all three components from the deconvolution of the spectrum are assumed to be coupled to a transition to the high spin state, then the excited state fraction, according to equation (4.13) is 84%. If only the contribution from the red peaks is considered, then the excited state fraction is 15%. Taking into account potential

uncertainties in the estimation of the excited state fraction and in order to exclude effects of these uncertainties on the definition of the molecular structure in the excited state, a decision was made to take the excited state fraction as a fitting parameter. The fitting procedure for the extraction of the excited state molecular structure is presented in the following section.

4.4.5 Excited state EXAFS analysis

The aim of the analysis is to confirm or disprove whether the $Fe(Pz_2Py)_2$ molecule goes to the high-spin quintet state after the optical excitation, as predicted by the theory. An alternative option is the triplet state. The molecular structures of both potential states were calculated by DFT [83]. A summary of the Fe-N bond distances of the first coordination shell for both spin states and comparison to the ground state X-ray diffraction data is given in table 4.10. As can be seen, in the ground state all six coordinating nitrogen

Table 4.10: Comparison of the Fe-N distances for the first coordination shell N atoms of the $Fe(Pz_2Py)_2$ molecule for the singlet ground state and for the excited triplet and quintet states. The ground state data is obtained from X-ray diffraction measurements, the excited state data is obtained from DFT calculations. Bond lengths are given in Å.

	$Fe - N_{py}$	$Fe - N_{pz,1}$	$Fe - N_{pz,2}$
Ground state (X-ray diffraction)	1.976	1.991	1.984
Triplet (DFT)	2.004	2.128	2.228
Quintet (DFT)	2.203	2.184	2.190

atoms are located approximately 2.0 Å from the Fe atom and the first coordination shell is therefore fully symmetric. In the quintet state, DFT suggests uniform elongation of all six Fe-N bonds by approximately 0.2 Å yielding total bond length for the first coordination shell of 2.2 Å. The situation is different in the triplet state. The theory suggests that in the triplet state one (symmetric) pair of $Fe - N_{pz}$ bonds will elongate for 0.137 Å, the second $Fe - N_{pz}$ bond pair will be elongated for 0.244 Å and the $Fe - N_{py}$ bond pair will remain almost unchanged. As there are significant differences in the symmetry of the quintet and triplet states, they must be reflected in the EXAFS functions and can be used to judge which structure matches better to the experimental data.
Because only approximate value of the excited state fraction is known, it is not possible to directly reconstruct the excited state spectrum. Therefore, the excited state fraction is considered to be a fitting parameter. The approach is to calculate theoretical EXAFS function $\chi_{theor}(k)$ for both excited state DFT structures and compare it with possible

experimental EXAFS functions for different excited state fractions. Additionally, the spectra are allowed to shift with respect to each other in k-space to account for possible different value of ΔE_0 in the excited state. In general, the fitting routine consists of the following steps:

- Simulation of the theoretical function $\chi_{theor}(k)$ for the DFT quintet and triplet structure with all non-structural parameters taken from the ground state fit. Export of this function to a Matlab environment.
- Assignment of a value to the excited state fraction from a range 0.02 to 0.33.
- Calculation of the experimental excited state spectrum for this excited state fraction according to equation 4.1.
- Extraction of the experimental EXAFS oscillation function $\chi_{exp}(k)$ from the experimental excited state spectrum
- Generation of a series of shifted EXAFS functions $\chi_{theor}(k + \Delta k)$ and calculation of the parameter $Q = (\chi_{theor} - \chi_{exp})^2/\sigma_{exp}$ for each value of Δk. σ_{exp} is the normalized standard deviation calculated for each data point of χ_{exp} at a given excited state fraction. Inclusion of the σ_{exp} weighting allows to account for the increased uncertainty of the χ_{exp} at high k-values. The range in k-space for evaluation of the parameter Q is $2\,\text{Å}^{-1}$ – $6.5\,\text{Å}^{-1}$.
- Return to step 2 where new excited state fraction is assumed

Simulation of the theoretical EXAFS function $\chi_{theor}(k)$ was performed with the Artemis software. As an input, DFT molecular structure for each excited state was used. For the simulation of the $\chi_{theor}(k)$ of the quintet state, all paths with $R_{eff} < 4.43\,\text{Å}$ were taken, for the triplet state all paths with $R_{eff} < 5\,\text{Å}$ were taken. As mentioned before, values for the Debye-Waller factors, the amplitude scaling factor and the energy shift were taken from the ground state fit and assigned in the same way as for the ground state fit. The experimental excited state XAS spectrum was reconstructed according to equation 4.1. The EXAFS oscillation function $\chi_{exp}(E)$ was then extracted according to its definition:

$$\chi_{exp}(E) = ES(E) - bg(E) \tag{4.14}$$

where $bg(E)$ is the atomic background. The atomic background was the same as for the ground state. Afterwards, $\chi_{exp}(E)$ was transferred to the k-space by the energy-wavevector relation:

$$k = \sqrt{2m(E - E_0)} \tag{4.15}$$

where m is the mass of the electron and E_0 is the edge energy. k^2 weighed spectra were compared.

The graphical representation of the fitting results is presented in fig. 4.28 and the fitting parameters, for which the best agreement is found are summarized in table 4.11.

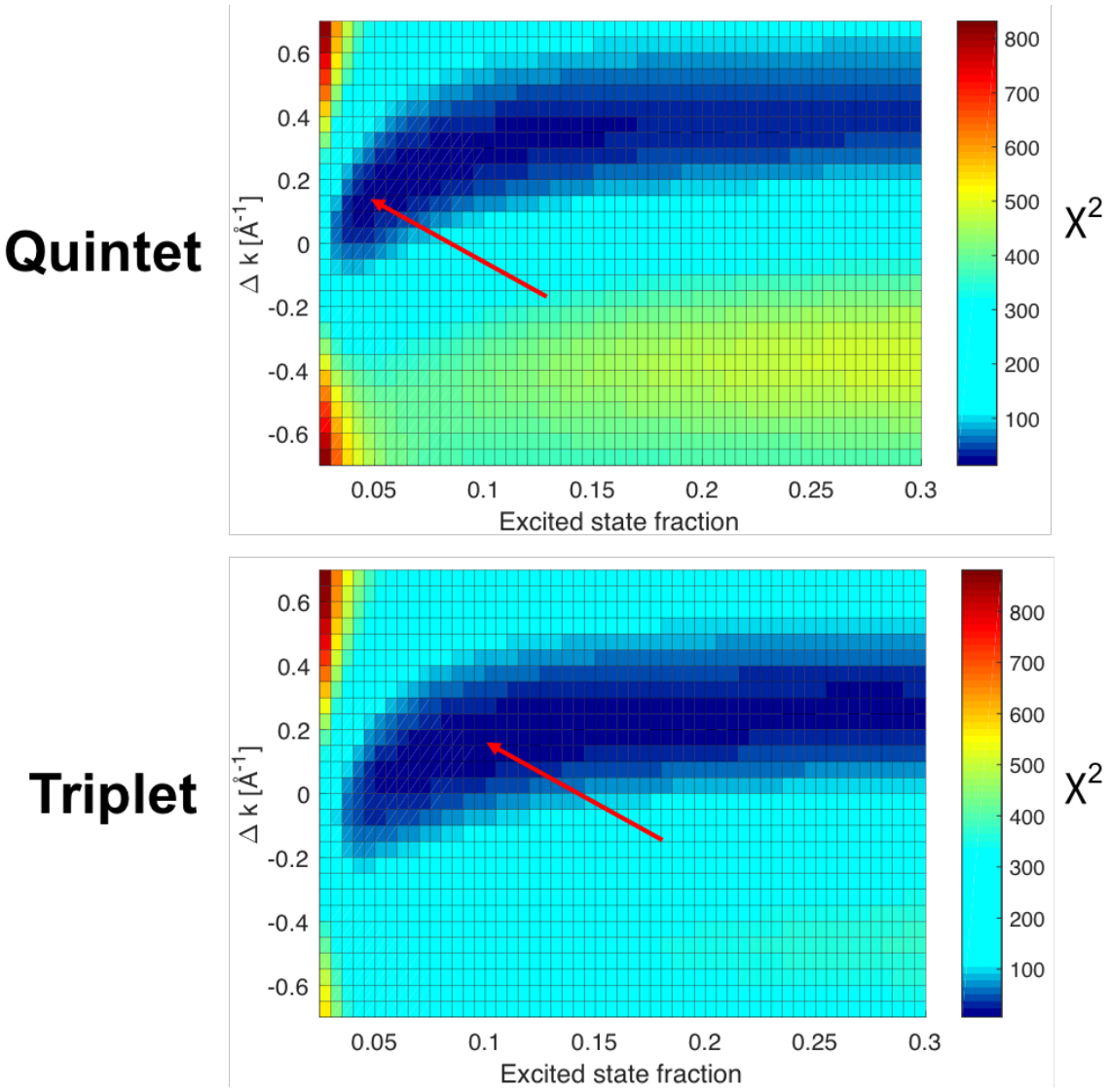

Figure 4.28: Results of the fitting of the theoretical EXAFS functions of the DFT simulated quintet (top) and triplet (bottom) excited states of the $Fe(Pz_2Py)_2$ molecule with the experimental excited state spectra, generated for different excited state fractions and shifts in the wavevector space.

As can be seen, for each structure there is one global minimum within the studied phase space. The minima for both structures are located at $\Delta k = 0.15\,\text{Å}^{-1}$ and the excited state fraction f=0.055 and f=0.1 for the quintet and triplet states correspondingly. Such low value of the excited state fraction matches to the assumption made in the previous section, that only the minor feature extracted from the deconvolution of the absorption spectrum, that contributes to the absorption at 343 nm results in the transition with spin

crossover. A comparison of both 2D plots shows, that the minimum for the quintet state is more defined and localized. Contrary to that, the minimum for the triplet state is rather shallow and valley-like, extending as a function of the excited state fraction. A

Table 4.11: Fitting parameters, for which the best agreement between the theoretical and experimental EXAFS functions for the DFT triplet and quintet states is obtained.

	Excited state fraction	Δk [Å^{-1}]
Triplet	0.1	0.15
Quintet	0.055	0.15

comparison of the theoretical EXAFS functions of the quintet and triplet state to their best matching experimental excited state EXAFS function is shown in fig. 4.29. The best matching experimental EXAFS functions are calculated according to the values in table 4.11 and equation 4.1. As can be seen, neither of the experimental excited state EXAFS functions shows a prefect agreement to the theoretical one in the entire k-range. For both states, feature at 5.2 eV is poorly reproduced. Apart from it, for the quintet state, the overlap is good in the range from 2 Å^{-1} to 6 Å^{-1}, excluding the 5.2 eV feature. For the triplet state, the agreement between the theoretical and experimental EXAFS functions is worse, compared to the quintet state. There is a clear offset in the positions of the peaks, located at 4.0 eV and 6.1 eV.

Low excited state fractions, obtained from the fitting mean that when the XAS spectrum of the excited state is being reconstructed according to equation 4.1, the experimental transient is divided by a small value and is therefore strongly enhanced. Along with the transient signal, noise scales also and this noise is being transferred to the excited state XAS spectrum and inherited by its EXAFS function. This explains the strong noise in the fits in fig. 4.29. This strong noise smears out features in the experimental EXAFS function and makes it harder to distinguish between both potential excited states of the $Fe(Pz_2Py)_2$ molecule.

Taking into account more defined minimum in the fit of the quintet state and better qualitative agreement between the theoretical EXAFS function for this state and its fit, a conclusion can be made that quintet is a more plausible candidate for the excited state, however additional measurements are needed in order to confirm this.

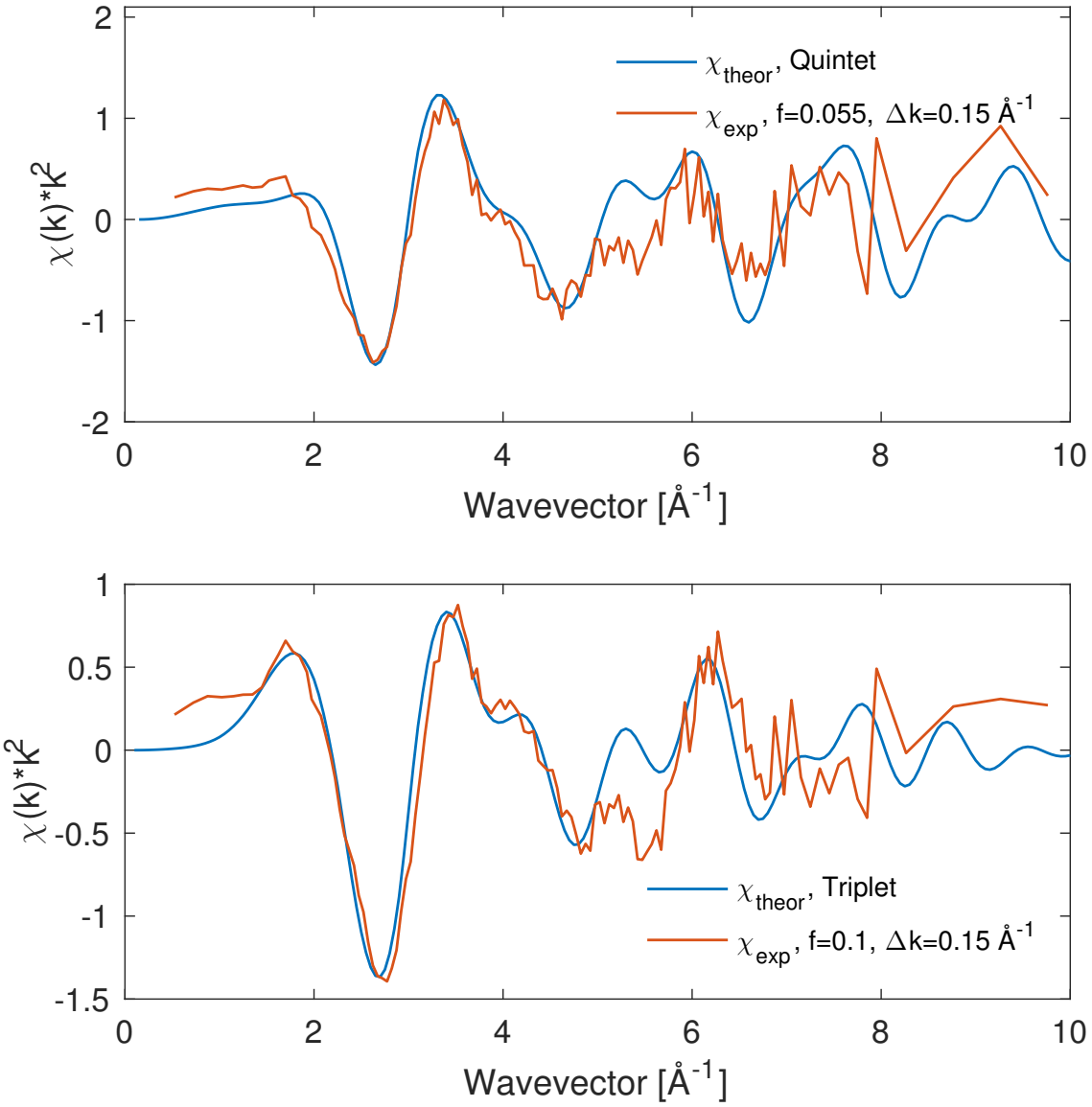

Figure 4.29: Comparison of the theoretical EXAFS functions of the DFT quintet (top) and triplet (bottom) to the best matching experimental excited state EXAFS functions. The experimental excited state EXAFS functions are calculated according to the values in table 4.11.

4.4.6 Relaxation dynamics

Relaxation dynamics of the $Fe(Pz_2Py)_2$ compound after optical pumping were studied at a fixed monochromator energy of 7125 eV, at which the intensity of the transient signal is the highest. As already mentioned, the pumping was performed at a wavelength of 343 nm. The experimental decay curve was fit with a monoexponential decay function, convoluted with a Gauss error function to account for the width of the X-ray probe pulse

in time domain. Experimental data along with a fit is presented in fig. 4.30.

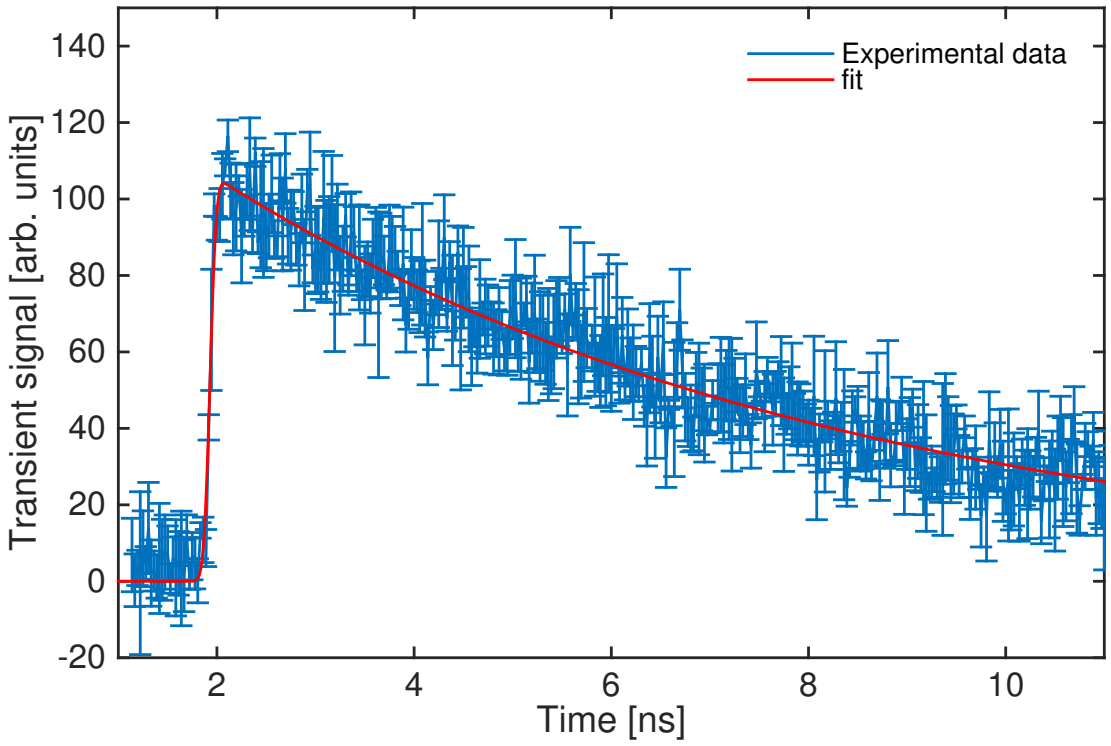

Figure 4.30: Deconvolution of the decay dynamics of the XAS transient signal measured at the energy of 7125 eV with a monoexponential decay model. Optical pumping of the sample performed with the 343 nm laser radiation.

The decay constant τ, obtained from the fit is 6.5 ns. Compared to other SCO compounds, $Fe(bpy)_3$ (τ=0.96 ns), $Fe(terpy)_2$ (τ=5.4 ns) [80, 81] such a decay constant is rather slow, indicating higher potential barrier ΔE between the high-spin and the ground state. This potential barrier, that needs to be overcome by the molecule in order to relax to the ground state is visualized in fig. 4.31. As the reaction coordinate for this class of compounds is the Fe-N bond length that always elongates for ~ 0.2 Å in the quintet high spin state, the height of the potential barrier ΔE is defined by the curvature of both potential curves and the energy difference between their minima. We can therefore conclude that the energetic difference between the minima of the potential curves of the high spin and the ground state of the $Fe(Pz_2Py)_2$ molecule must be lowered, compared to other SCO complexes, resulting in higher energy barrier and correspondingly lower transition rate from the high spin to the ground state.

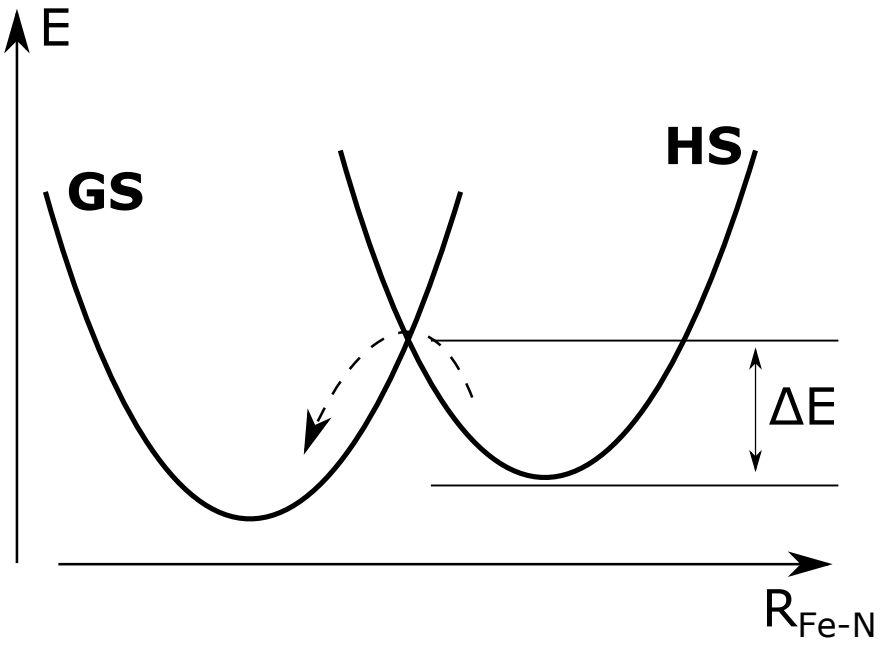

Figure 4.31: Potential energy scheme that represents relaxation pathway from the high spin to the ground state. Fe-N bond distance is the reaction coordinate. In order to transfer to the ground state, the molecule has to overcome energy barrier ΔE.

4.4.7 Alternative fitting model

As an alternative to the fitting approach used in the section 4.4.3 to fit the ground state spectrum, a new approach is suggested. The new approach is based on the fact, that not all atoms in the molecule can move freely, the atoms form chemical bonds with each other and therefore can be parametrized with a reduced number of fitting parameters. The suggested fitting model accounts for the geometry of the molecule and allows to connect the displacements of the atoms in higher coordination shells to the displacement of the atoms in the first coordination shell, if these atoms are considered to be rigidly connected. Such situation arises when, for example, the central atom is coordinated by atoms, that are a part of a ring or another robust structure, like for the $Fe(Pz_2Py)_2$ molecule, in which the central atom is coordinated by the nitrogen atoms from the pyridine and pyrazole rings (fig. 4.23). In addition to the reduction of the number of fitting parameters, the suggested model automatically ensures that the geometry of the molecule is not distorted during the fitting process. If the fit suggests that one of the coordinating atoms has to be shifted towards or away from the absorber, then other atoms that are connected to this shifted atom will be moved accordingly and the relative distances between them will be preserved. This is shown in fig. 4.32 where a pyridine ring is shifted as a robust unit further from the central iron atom.
The fitting procedure for the ground state EXAFS analysis presented here is the same as

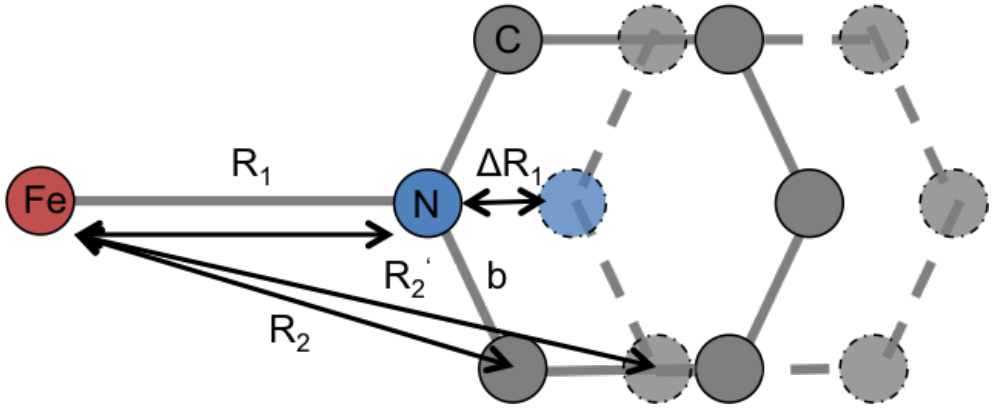

Figure 4.32: Graphical representation of the parametrization of the scattering paths of the $Fe(Pz_2Py)_2$ molecule, if the pyridine ring is shifted as a robust unit from the central Fe atom.

in the section 4.4.3, with the same FEFF calculation of the scattering paths, only their parametrization in the Artmeis software is different. An overview of the first twelve paths provided by FEFF calculation is given in table 4.12. Two fitting models with different number of considered scattering paths were tested. The first model includes only single scattering paths 1-4 and the second model includes all paths shown in the table, except path 10. All these paths have intensity more than 8% relative to the intensity of the most intense path and an effective path length below 3.3 Å. The first path is 6-fold degenerate and represents single scattering from the nitrogen atoms that coordinate the central Fe atom (first coordination shell). Paths 2, 3 and 4 represent single scattering from the second coordination shell nitrogen and carbon atoms that are a part of the pyridine and pyrazole rings. Path 6 is the single scattering path from the carbon atom, that bridges two pyrazole and one pyridine ligand. All shown double scattering paths involve the first coordination shell nitrogen atoms and either neighbouring second coordination shell nitrogen or carbon atom.
The model for the parametrization of the scattering paths is explained in fig. 4.32.
The parametrization of the scattering paths is based on the following assumptions:

- Uniform enlargement of the molecule
- Ligands can be treated independently
- Ligands do not rotate around the coordinating atom
- Pyrydine/pyrazole rings are robust

The first assumption is based on DFT calculations. The second point arises from the fact, that there are only multiple scattering paths that involve atoms from one ligand

molecule. The assumption that there is no rotation of the pyrydine/pyrazole rings around the coordinating atom is due to the fact that ligands are bridged by the central C atom (fig. 4.23). The main structural parameter of the alternative model is the uniform elongation of the Fe-N bonds of the first coordination shell ΔR_1 (fig. 4.32). As the pyrydine/pyrazole rings are considered to be robust and non-rotating, displacements of all other atoms of the ligand are entirely defined by ΔR_1. The displacements of the second coordination shell atoms with respect to the first coordination shell ones can be extracted via the cosine theorem as:

$$\Delta R_2 = \sqrt{(R_1 + \Delta R_1)^2 + b^2 - 2b(R_1 + \Delta R_1) * \cos(\alpha)} - R_2 \tag{4.16}$$

where b is the distance between the second coordination shell atom and the first coordination shell one, R_1 and R_2 are the distances from the first and second coordination shell atoms to the absorber atom, ΔR is the elongation of the first coordination shell bond distance and α is the angle between vectors R_1 and R_2 (fig. 4.32). For the double scattering paths the correction to the path length is given by:

$$\Delta R_{ms} = \frac{1}{2}(\Delta R_1 + \Delta R_2) \tag{4.17}$$

Table 4.12: Scattering paths, obtained from the FEFF calculation for the ground state molecular structure of the $Fe(Pz_2Py)_2$ complex. Indices 1 and 2 show to which coordination shell a certain atom belongs. Atom C_3 is the atom that bridges the ligands (fig. 4.23). R_{eff} is given in Å.

No	Degen	R_{eff}	Amp	Trajectory
1	6	1.983	100	$Fe - N_1 - Fe$
2	4	2.881	28.8	$Fe - N_2 - Fe$
3	2	2.888	12.8	$Fe - C_2 - Fe$
4	2	2.939	12.29	$Fe - C_2 - Fe$
6	2	3.001	11.71	$Fe - C_3 - Fe$
7	4	3.106	8.49	$Fe - C_2 - N_1 - Fe$
8	4	3.109	21.58	$Fe - C_2 - Fe$
9	8	3.120	15.84	$Fe - N_2 - N_1 - Fe$
10	4	3.123	3.04	$Fe - H - Fe$
11	4	3.131	9.59	$Fe - N_1 - C_2 - Fe$
12	8	3.217	28.97	$Fe - N_1 - C_2 - Fe$

In the alternative model, atoms in the first and second coordination shells are assigned

with the Debye-Waller factors σ_1 and σ_2 correspondingly. C atom, that bridges three ligands is assigned with parameters ΔR_{C_3} and σ_{C_2}. The multiple scattering paths have Debye-Waller factor σ_3. In total, the model with the single scattering paths contains five fitting parameters: S_0^2, ΔE_0, ΔR_1 and the Debye-Waller factors for the first and second coordination shells σ_1 and σ_2 correspondingly. The reduced number of the fitting parameters allows to reduce the fit range in R-space for this model to 1 Å – 2.5 Å. The second model that includes more distant atoms and multiple scattering paths has two additional structural parameters that are ΔR_{C_3} for the bridging carbon atom and σ_3 that is assigned to the multiple scattering paths, because there is no good way to connect the mean-square displacements of the multiple scattering paths with the mean-square displacements of the separate atoms. The fit range for the second model is 1 Å – 2.9 Å. The structural and non-structural parameters, obtained from the ground state EXAFS fitting with both models are summarized in table 4.13 and the fit results are shown in fig. 4.33.

Table 4.13: Summary of the structural and non-structural parameters, obtained from the fitting of the ground state EXAFS spectrum of the $Fe(Pz_2Py)_2$ molecule with two models with alternative parametrization of the fitting parameters. The ss model includes only the single scattering paths from the 6 nearest neighbours and the model ms includes single and multiple scattering paths with $R_{eff} < 3.3$ Å. The value of the energy shift ΔE is given in eV, values for ΔR are given in Å and values for the Debye-Waller factors are given in Å^2.

	S_0^2	ΔE_0	ΔR_1	ΔR_{C_3}	σ_1	σ_2	σ_3
model ss	0.743	-3.96	-0.0098		0.001	0.003	
model ms	0.873	-4.45	-0.0093	-0.15	0.003	0.001	0.01

As can be seen, there is a good agreement between the experimental data and the fit in both k and R space independent whether the multiple scattering paths are included or not. Both fits nicely reproduce peaks for the first and second coordination shells of the pseudo radial distribution function as well as all main features of the EXAFS oscillation function $\chi(k)$. Some high-frequency features of $\chi(k)$ are not reproduced because they require inclusion of longer scattering paths, that can not be paramterized as a function of ΔR_1.

The structural and non-structural parameters, obtained from the new fits are also in good agreement with those presented in section 4.4.3. The amplitude scaling factor, the energy shift and ΔR_1 are very similar for all three fitting models. The alternative fitting model with singe scattering paths also has the same value of the Debye-Waller factor σ_1 as the

basic model in section 4.4.3, though this value seems to be slightly underestimated. The model with the multiple scattering paths has a higher value of σ_1 and a relatively small value for σ_2 which is probably being compensated by the fitting routine by a larger value of σ_3.

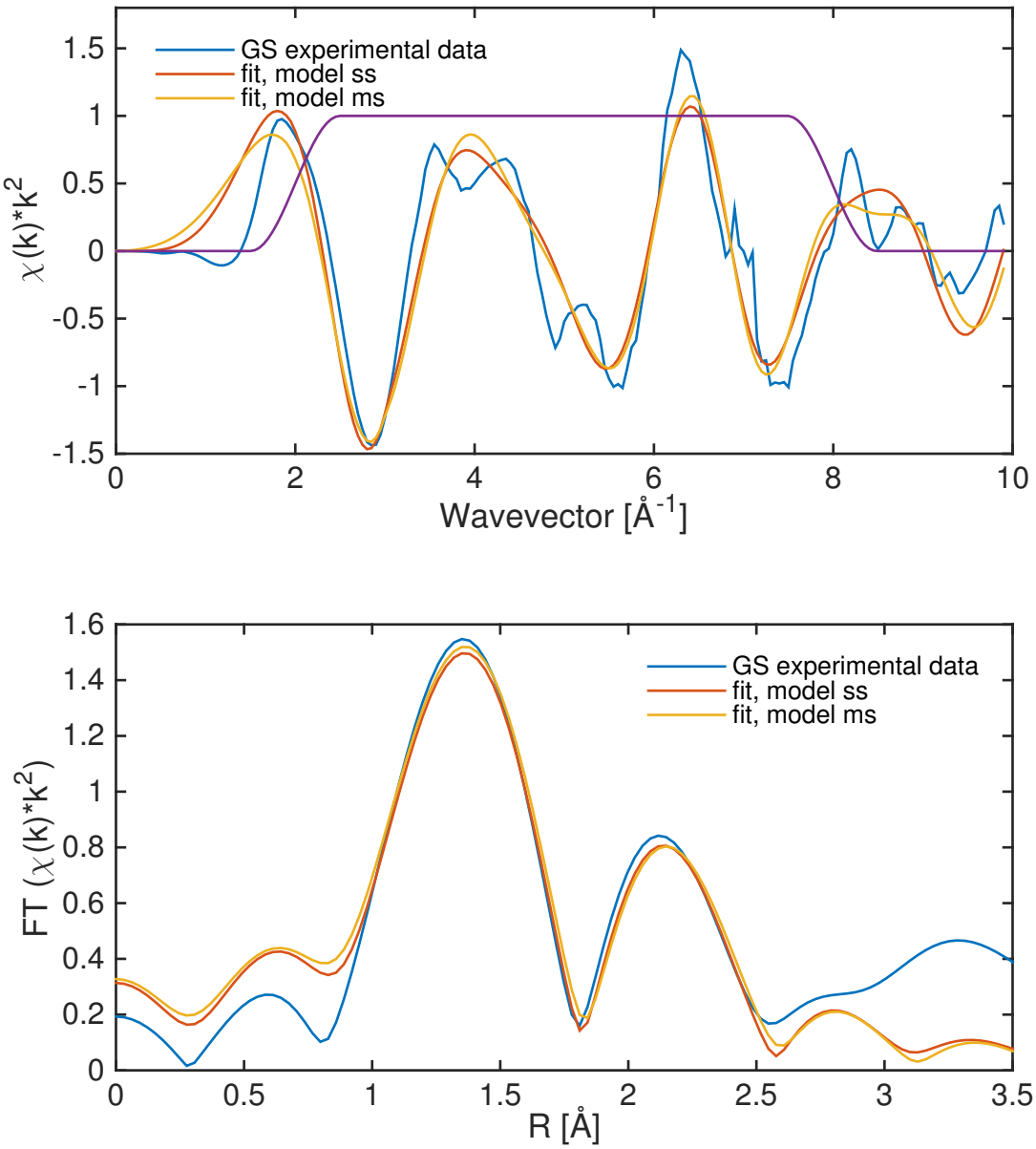

Figure 4.33: Results of the ground state fitting of the $Fe(Pz_2Py)_2$ molecule with an alternative parametrization of the scattering paths: k^2 weighed EXAFS function (top) and pseudo radial distribution function (bottom)

Interesting is that the fit suggests extremely large shift of the ΔR_{C_3} towards the iron

atom. In order to check whether this is related to the alternative way of parametrization, the basic ground state fitting model in section 4.4.3 was investigated again with one more fitting parameter ΔR_{C_3}. This parameter was assigned to path 6 instead of ΔR_2 in the same way as in the alternative fitting model. The obtained value of the new parameter ΔR_{C_3} is surprisingly -0.16 Å in agreement with the value from table 4.13. The other fit parameters and the fit quality itself were little affected, probably due to the relatively low intensity of this scattering path. This fact confirms that all models show consistent results and gives a hint that according to the EXFAS analysis and independent on the fitting model, there is a need to "pull" the second coordination shell atoms towards the central atom

4.4.8 Conclusions

A new approach to analyze possible excited state molecular geometries and distinguish which one is realized, was developed and applied to the $Fe(Pz_2Py)_2$ complex. Due to low excited state fraction it is not possible to make unambiguous statement whether the excited state of the studied molecule is quintet or triplet, but there are hints that it is rather quintet, which is also matching with the DFT calculation results. The new approach can be further used in experiments with higher signal/noise ratio.

The analysis of the XAS decay dynamics, measured at the energy of 7125 eV, yields 6.5 ns lifetime of the optically excited state of the $Fe(Pz_2Py)_2$ molecule. In comparison with other SCO complexes like $Fe(dcpp)_2$ (0.28 ns) or $Fe(bpy)_3$ (0.96 ns), $Fe(Pz_2Py)_2$ has a relatively long-lived excited state. According to the energy scheme for the class of SCO complexes, this indicates that the potential barrier for the transition to the ground state is high, meaning that the energy of the complex in the excited state is lowered and this state is well-stabilized.

In addition, an alternative approach to parametrization of the EXAFS scattering paths, that uses constraints based on the geometry of the molecule and the nature of the chemical bonds was suggested and its applicability to the $Fe(Pz_2Py)_2$ molecule was successfully demonstrated. The method allows to reduce the number of the free fitting parameters and can be applied when information about the first or the first and the second coordination shells is needed.

4.5 Tyrosinase model complexes

In the preceding section results on optical Raman scattering studies on two tyrosinase model complexes are presented. The presented results are a part of the publications [84, 85]. Like the natural tyrosinase, compounds [Cu(btmgp)]I and $[Cu(TMG_2tol)]_2$ form a peroxo Cu_2O_2 core in the presence of molecular oxygen and are therefore potential candidates for catalysis of various oxidation reactions. The oxygenated form of these compounds decays rapidly under room temperature with a decay rate on the order of $1\,s^{-1}$. The lifetime of the oxygenated form of the complex can be extended to hours and days when the sample is cooled down to temperatures below -60° C. [5, 86]. Therefore, a special vacuum cryostate was developed and produced, allowing to reach temperatures down to -80° C inside the sample cuvette and extending the lifetime of the oxygenated form of the studied complexes to make systematic and time consuming spectroscopic studies possible.

4.5.1 [Cu(btmgp)]I

The ability of the [Cu(btmgp)]I to bind molecular oxygen has been demonstrated before [87], however no systematic resonance Raman scattering studies have ever been reported. With a newly developed cryostate a resonance Raman study of the oxygenated form of [Cu(btmgp)]I complex was performed (fig. 4.34).

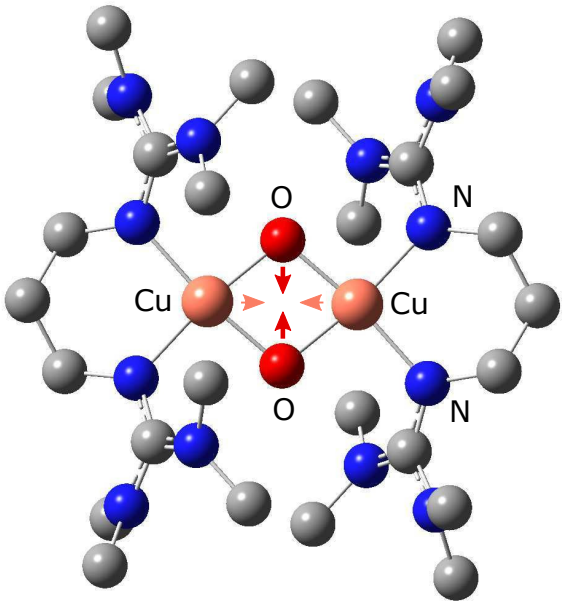

Figure 4.34: Oxo form of the [Cu(btmgp)]I complex. Two precursor molecules bind a molecule of oxygen and form Cu_2O_2 core. Arrows represent symmetric Raman active vibration of the core. The figure is adapted from [84].

[Cu(btmgp)]I is a mononuclear copper complex, in which the copper atom is coordinated by the bidentate (bis(tetramethyl)guanidino)propane ligand (btmgp) and a iodine ion. Upon oxygenation two precursor molecules bind a molecule of oxygen and a new dinuclear complex with a rhomb-like Cu_2O_2 core is formed. Each copper atom of the new molecule is four-fold coordinated: twice by the nitrogen atoms of the btmgp ligand and twice by the oxygen atoms. The oxygenation was performed by a supply of $^{16}O_2$ gas directly into precursor solution, cooled to -80° C. Degassed 99% propionitrile was used as a solvent.

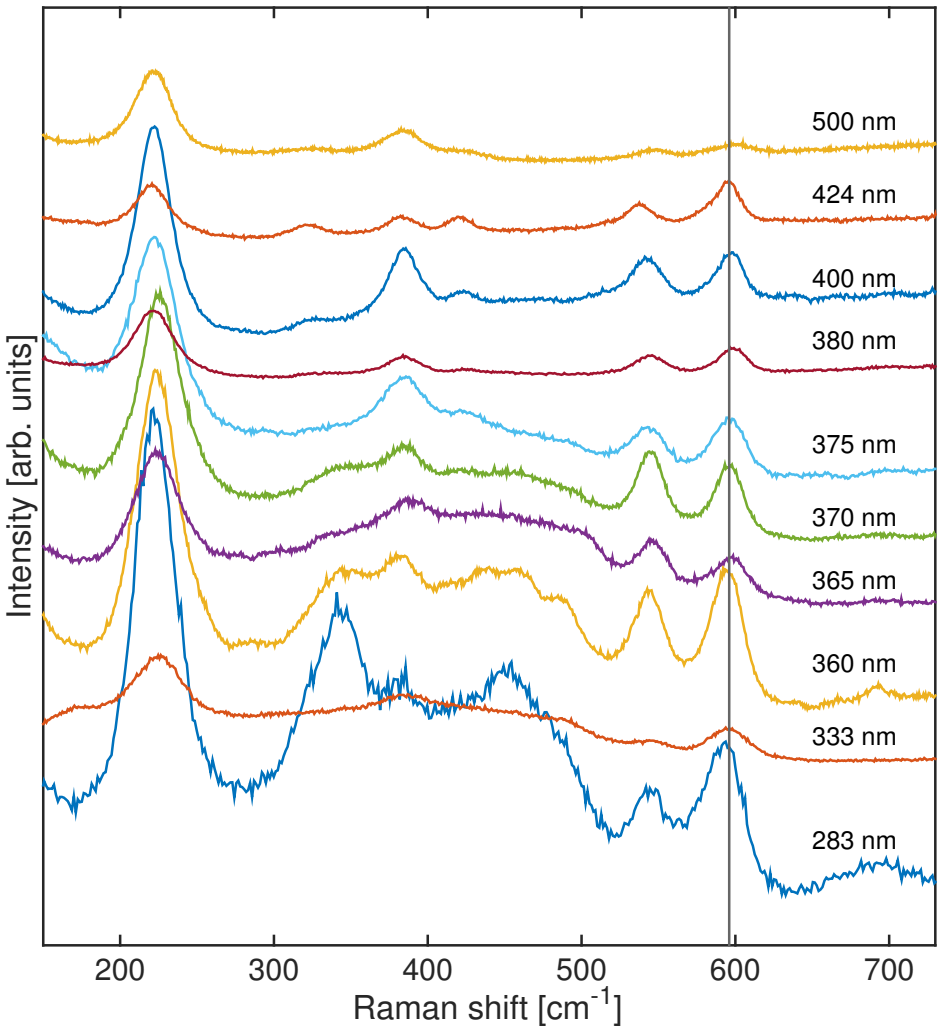

Figure 4.35: Resonance Raman study of the $^{16}O_2$ oxygenated [Cu(btmgp)]I compound. Gray vertical line is a guide to the eye and shows symmetric breathing mode of the Cu_2O_2 core. Excitation wavelength of each spectrum is shown on the right side. Spectra were offset along y-axis for convenience. The figure is adapted from [84].

The resonance Raman study was performed at ten different incident laser wavelengths

in the range from 282.4 nm to 500.2 nm. Stacked Raman spectra, recorded at each wavelength, normalized to the integration time, incident laser power and the absorption coefficient are shown in fig. 4.35. A dependence of the intensity of the 596 cm^{-1} Raman mode on the incident laser wavelength is shown in fig. 4.36. According to DFT calculation, this mode is a symmetric breathing mode of the Cu_2O_2 core of the oxygenated compound [88]. As can be seen from fig. 4.36, there is a distinct resonance behaviour in the UV spectral region at around 360 nm incident photon wavelength. A closer look shows a double resonance structure of the symmetric Cu_2O_2 vibration. The maxima of the peak intensity are observed at 358 nm and 370 nm or 3.46 eV and 3.35 eV, correspondingly. Taking into account the energy of the 596 cm^{-1} vibrational mode $h\nu_{vib} \approx 74$ meV, a double resonance can be assigned to the ingoing and the outgoing resonances with $2h\nu_{vib} \approx 148$ meV (experimental difference between positions of both maxima is 110 meV).

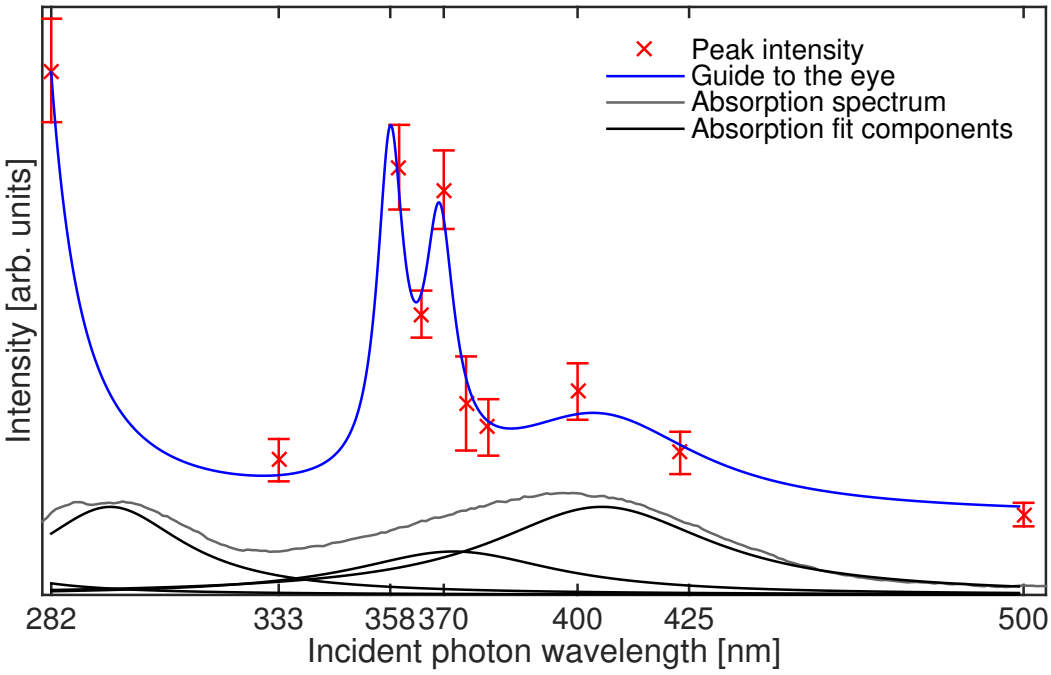

Figure 4.36: Dependence of the intensity of the symmetric Raman breathing mode of the oxygenated form of the [Cu(btmgp)]I complex as a function of the incident photon energy. The absorption spectrum of the complex and its deconvolution are shown with light gray and black lines, correspondingly. Blue curve acts as a guide to the eye. The figure is adapted from [84].

The presence of the resonance in the region 360 nm - 370 nm is additionally supported by the deconvolution of the absorption spectrum of the compound. The deconvolution with Lorenzian functions yields two components of the broad maximum of the absorption spectrum, covering a range from 333 nm to 500 nm. One of the components is centered

at 370 nm and can therefore represent the electronic transition, to which the 596 cm^{-1} vibrational mode couples.

4.5.2 $[Cu(TMG_2tol)]_2$

$[Cu(TMG_2tol)]_2$ complex is another tyrosinase model, potential for catalytic applications. In contrast to the mononuclear [Cu(btmgp)]I complex, non-oxygenated form of the $[Cu(TMG_2tol)]_2$ compound has a Cu_2 core. Each copper atom in this complex is coordinated by two nitrogen atoms of the ligands. In order to confirm the ability of this complex to bind molecular oxygen, a Raman study with an isotope exchange was conducted. For this purpose, a 5 mMol solution of the complex in 99% propionitrile was prepared in a oxygen- and water-free atmosphere (<0.5 ppm) and subsequently cooled to -85° C in the cryostate, mentioned earlier in this section.

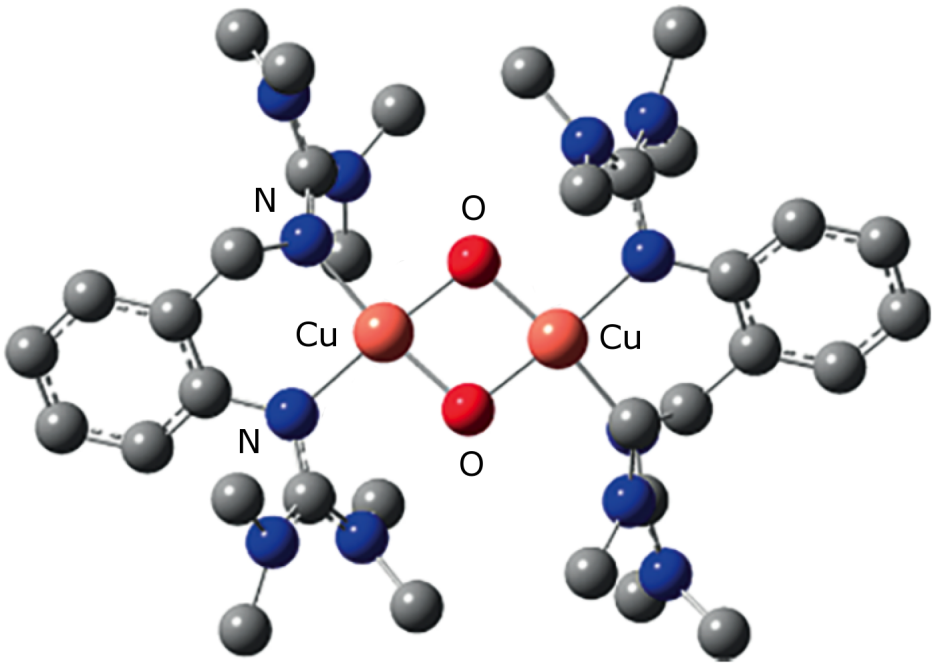

Figure 4.37: Oxygenated form of the $[Cu(TMG_2tol)]_2$ complex. A precursor molecule binds a oxygen molecule with the formation of the Cu_2O_2 core. The figure is adapted from [85].

After reaching -85° C, the solution was oxygenated with $^{16}O_2$ gas and Raman spectra of the oxygenated solution have been recorded. Afterwards, Raman spectra of the non-oxygenated solution, that was also cooled down to -85° C and oxygenated with $^{18}O_2$ gas were measured. The results of the measurements are presented in fig. 4.38. As can be seen, the Raman spectra of the oxygenated form of the $[Cu(TMG_2tol)]_2$ are similar to

those of the [Cu(btmgp)]I complex, supporting the fact, that the Cu_2O_2 core is formed. The mode, located 600 cm^{-1} is assigned by DFT to the symmetric breathing mode of the Cu_2O_2, analogous to the [Cu(btmgp)]I. Upon isotope exchange, the vibrational mode, originally located at 600 cm^{-1} for the oxygenation with the $^{16}O_2$ gas, shifts for -27 cm^{-1} to 572 cm^{-1} when oxygenated with heavier $^{18}O_2$ atoms, thus confirming the ability of the $Cu(TMGtol)_2$ to bind molecular oxygen.

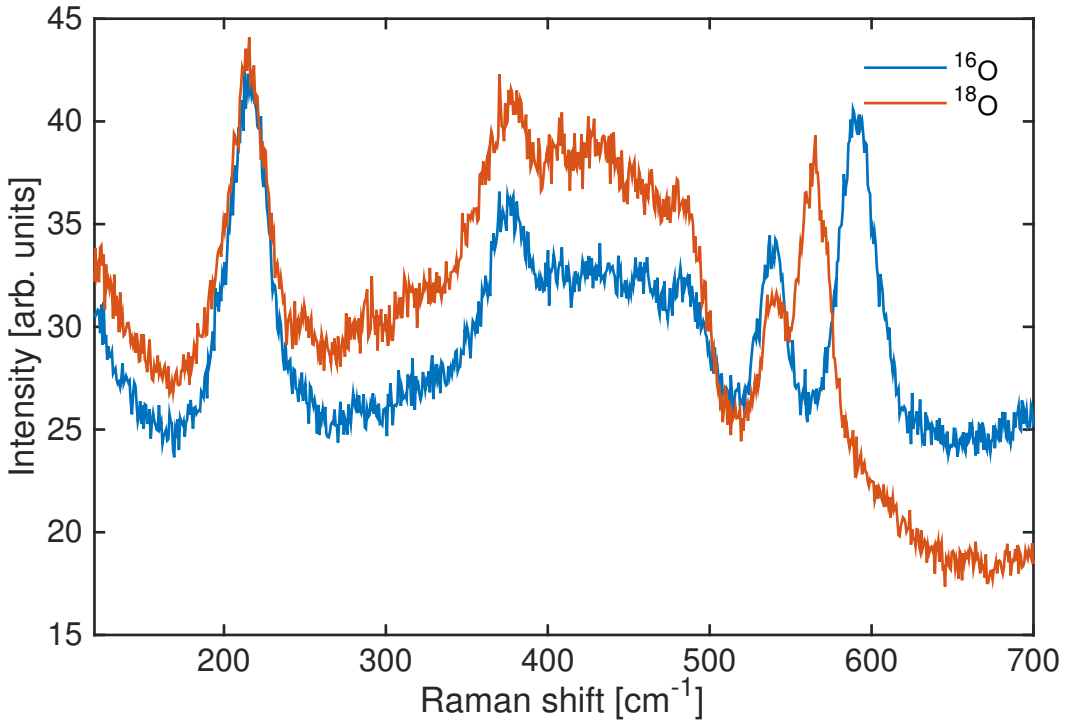

Figure 4.38: Shift of the 600 cm^{-1} Raman mode upon oxygenation of the $[Cu(TMG_2tol)]_2$ precursor with $^{18}O_2$ gas compared to $^{16}O_2$ gas. The figure is adapted from [85].

4.5.3 Conclusions

With the help of Raman scattering technique binding of molecular oxygen by two tyrosinase model complexes at low temperatures was successfully confirmed. The obtained results confirm the assignment of the experimentally measured Raman modes made by DFT calculation and provide an insight into the coupling between the electronic and vibrational transitions of the studied molecules.

Chapter 5

Summary and perspectives

The present work highlights results on instrumentation, scientific investigations on various classes of bio-inorganic transition metal complexes as well as new approaches for the EXAFS data analysis.

Within the instrumentation part new complex alignment approach was established and successfully applied to the VUV Raman monochromator. The suggested approach allowed to align and then characterize performance of the monochromator by means of optical laser interferometry, optical wavefront sensing and off-line X-ray measurements with actual soft X-ray photons and without using expensive FEL beamtimes. The new approach will be further used to align the second monochromator of the VUV Raman spectrometer. After completion of the alignment, the VUV Raman spectrometer will offer exciting measurement capabilities, combining high resolution and strong stray-light rejection of the confocal spectrometer design with an intermediate slit. This will allow studying inelastic excitations in media at the energies of transition metal L and M edges. A further exciting step will be to upgrade the setup with a femtosecond optical laser and all corresponding equipment to perform pump-probe experiments and fully utilize sub-100 femtosecond pulse duration of the free-electron laser FLASH. This will open a gateway for probing structural and electronic properties of matter at ultrafast time scales.

Within the part of the thesis that focuses on transition-metal complexes, structure and dynamic properties of various model complexes were characterized. Pump-probe X-ray absorption spectroscopy was employed to investigate ground and excited state molecular structures of the entatic state $Cu(TMGqu)_2$ complex and the spin crossover complex $Fe(Pz_2Py)_2$. For the $Cu(TMGqu)_2$ complexes that are available with oxidation state of the central Cu atom +1 and +2 in the ground state, it was shown from the experimental XAS transients that the optically excited state of the $[Cu(TMGqu)_2]^+$ is structurally and electronically similar to the ground state $[Cu(TMGqu)_2]^{2+}$. The EXAFS analysis of the ground and the optically excited state of the $[Cu(TMGqu)_2]^+$ showed contraction of the Cu-N bond by 0.074 Å in the excited state, in agreement with the theoretical predictions.

In addition to the structure and electronic properties, pump-probe XAS measurements allowed to extract excited state lifetimes for both $[Cu(TMGqu)_2]^+$ and $Fe(Pz_2Py)_2$. For the $Fe(Pz_2Py)_2$ a decay constant for the exited high-spin state of 6.5 ns is reported, which allows to conclude that excited state structure is better stabilized with a higher potential barrier between the excited and ground state, compared to some other compounds of this class.

Electron binding energies of the other entatic-state complex $Cu(DMEGqu)_2$ were characterized by steady-state X-ray photoelectron spectroscopy. The complex is very similar in structure to the $Cu(TMGqu)_2$ and is also available in two forms that have oxidation state of the copper atom +1 and +2 in the ground state. Obtained Cu $L_{2,3}$ binding energies confirmed the oxidation state of the central cooper atom being +1 or +2 depending on the sample type. In addition, the $1s$ electron binding energies of the nitrogen atoms for both $[Cu(DMEGqu)_2]^+$ and $[Cu(DMEGqu)_2]^{2+}$ species were extracted. The obtained values match well to the theoretical calculations and allow to make conclusions on the redistribution of the electron density within the molecule upon the change of the oxidation state of the central copper atom. The $1s$ electron binding energies of nitrogen can be further used to interpret XAS spectra of this complex, measured at the N K-edge. This will allow to get a deeper insight into to the structure and electronic properties of the entatic state complexes and characterize them by different techniques and at different absorption edges.

Two Tyrosinase model complexes [Cu(btmgp)]I and $[Cu(TMG_2tol)]_2$ were investigated by means of optical Raman spectroscopy in their oxygenated form. As the oxygenated form of these complexes is only stable under temperatures typically below -60° C, all measurements were performed in a specially developed cryostate that allows reaching temperatures below -80° C inside the air tight cuvette. By analysis of the Raman spectra of the $[Cu(TMG_2tol)]_2$ precursor oxygenated with $^{16}O_2$ and $^{18}O_2$ gas it was possible to confirm binding of the molecular oxygen by it with formation of the $Cu_2O_2(TMG_2tol)_2$ species. For the $^{16}O_2$ oxygenated form of the [Cu(btmgp)]I precursor, which is $Cu_2O_2(btmgp)_2$, resonance Raman study was performed, yielding a double resonance structure for the symmetric breathing mode of the Cu_2O_2 core within the region from 358 nm to 370 nm.

In addition to the experimental results, an alternative approach to parametrization of the EXAFS scattering paths in the IFEFFIT fitting routine was suggested. The applicability of this method was demonstrated on the ground state EXAFS spectrum of the $Fe(Pz_2Py)_2$ complex. The suggested method uses geometrical constrains that arise from the molecular structure and allows connecting changes of the second coordination shell distances to the first coordination shell ones, thus leading to a reduced number of structural fitting parameters. This reduces mathematical ambiguity of the fit, guarantees that structure of the parts of the molecule, like pyridine or pyrazole rings is not distorted dur-

ing the fitting routine and also allows to perform fitting in a narrower range in R-space, because the number of the free parameters is reduced. The method can be used if parts of the molecule are considered to be rigid and is not applicable to make parametrization of higher coordination shells or scattering paths that are more than double. This makes the method helpful, if information about the local environment around the absorber, like first or first and second coordination shells is needed.

From the perspectives point of view, applying *Light-Induced Excited Spin State Trapping* (LIESST) effect with a newly developed cryostate might be very efficient to collect Raman spectra of the high-spin state of the $Fe(Pz_2Py)_2$ complex. If the sample solution is cooled down to -80° C in a cryostate and is being continuously illuminated with CW radiation that triggers transition to the HS state, then due to low temperature a significant fraction of the molecules will be trapped in the high spin state and their Raman scattering spectra can be collected. The obtained Raman spectra will allow to unambiguously characterize the symmetry and the structure of the HS state and will potentially allow to distinguish triplet and quintet HS geometries.

Chapter 6

Acknowledgments

First of all I would like to thank my supervisor Michael Rübhausen for giving me the opportunity to become a part of a very nice and friendly research group and participate in exciting scientific experiments in various fields of modern physics. His inspiring guidance and supervision helped me to go through sometimes tough stages of the research process, making me more confident and self-standing in the field of science. It is a great pleasure to work with Michael!

I would also like to thank my co-supervisor Arwen Pearson. Her always immediate and clear feedback and willing to advance my professional development always kept me on the right way! In addition, I want to appreciate numerous and valuable scientific discussions with Nils Huse and Clemens Ulrich. Many interesting ideas were born during these discussions and later they became a milestones of my thesis.

It would not have been possible to get exciting experimental results without exciting samples. I am therefore extremely grateful to Sonja Herres-Pawlis and Alexander Hoffmann for providing the samples and opening the door to the world of bio-inorganic chemistry! In addition, not only an exciting sample, but also an excellent experiment is needed. I would thus like to thank Benjamin Dicke, Maria Naumova, Siarhei Dziarzhytski, Günter Brenner, Niko Höppel and Benjamin Grimm-Lebsanft, with whom we had many long beamtimes at FLASH, PETRA III and BESSY research facilities together. I would also like to appreciate the help of Holger Weigelt for numerous upgrades of the VUV Raman spectrometer. Apart from all written above I want to thank Dieter Rukser, Florian Biebl and Gerd Neuber, with whom we prepared and conducted numerous Raman scattering experiments and Noei Heshmat, for her help with the XPS measurements.

It is impossible to omit former and current members and guests researchers of the APOG group: Philipp Bremer, Bastian Besner, Calvin Brett, Rilana Maeser, Shirly Josefina Espinoza, Paul Graham and Romain Grasset. You are good friends and colleagues!

And finally, my deepest and most sincere gratitude to my family. Your value in my life can not be overestimated!

Publication preprint

Alignment of the aberration-free VUV Raman monochromator at FLASH

Mykola Biednov, Benjamin Dicke, Günter Brenner, Holger Wiegelt, Barbara Keitel, Michael Rübhausen and Siarhei Dziarzhytski

Alignment of the aberration-free VUV Raman monochromator at FLASH

Authors

Mykola Biednov[ab]*, Benjamin Dicke[ab], Günter Brenner[c], Holger Weigelt[c], Barbara Keitel[c], Michael Rübhausen[ab] and Siarhei Dziarzhytski[c]

[a]Institut für Nanostruktur- und Festkörperphysik, Universität Hamburg, Notkestrasse 85, Hamburg, 22607, Germany

[b]Center for Free-Electron Laser Science, Deutsches Elektronen-Synchrotron, Notkestrasse 85, Hamburg, 22607, Germany

[c] Deutsches Elektronen-Synchrotron DESY, Notkestrasse 85, Hamburg, 22607, Germany

Correspondence email: mbiednov@physnet.uni-hamburg.de

Synopsis One or two sentences suitable for the Journal contents listing (style: IUCr synopsis).

Abstract The vacuum-ultraviolet (VUV) double-stage Raman spectrometer is permanently installed as an experimental end-station at the PG1 beamline of the soft X-Ray/XUV free-electron laser in Hamburg (FLASH). The monochromator stages are designed according to the Czerny-Turner optical scheme, adapted for the VUV photon energy range, with optical elements installed at grazing-incidence angles. Such an optical scheme along with the usage of off-axis parabolic mirrors for light collimation and focusing, allows for aberration-free spectral imaging on the optical axis. Combining of the two monochromators in additive dispersion mode allows for reaching high resolution and superior stray light rejection, but puts high demands on the quality of the optical alignment. In order to align the instrument with the highest precision and to quantitatively characterize the instrument performance and thus the quality of the alignment, optical laser interferometry, Hartmann-Shack wavefront-sensing measurements as well as off-line soft X-ray measurements and extensive optical simulations were conducted. In this paper the concept of the alignment scheme and the procedure of the internal optical alignment are presented. Furthermore, we show our results on the imaging quality and resolution of the first monochromator stage.

Keywords: VUV Raman spectrometer, alignment, interferometry, Free-Electron Laser, wavefront sensor

1. Introduction

Resonant Inelastic X-Ray Light Scattering (RIXS) is a powerful spectroscopic tool that can be utilized to study different types of elementary excitations in, for example, strongly correlated systems like manganites or cuprates, or charge transfer processes in bio-inorganic molecules with metal centers (Ament *et al*. 2017; Rusydi *et al*. 2014). RIXS is a *photon-in photon-out* process in which the change in the energy and momentum of the incident photon during the scattering process is investigated. This technique allows studying elementary excitations of matter. The technique is element and orbital specific when it is in resonance with an atomic absorption edge by inducing specific orbital transitions of the element of interest. At the same time, such a tuning of the incident energy may result in a great enhancement of the scattering cross-section due to resonant nature of the scattering process (Kotani and Shin 2011). RIXS is a "photon hungry" technique and availability of the tunable high-brilliance sources is crucial for an experiment. Moreover, growing interest on dynamics studied via RIXS requires short in fs-ps range excitation pulses which nowadays become more available at light sources as free-electron lasers. The high-brilliance high repetition rate free-electron laser FLASH is capable of providing sub 100-femtosecond pulses with the wavelength in the range from 6.9 to 47nm (Ackermann *et al*. 2007), which covers the range of L-edges of lighter elements or M-edges of the heavier ones, such as transition metals. These properties were decisive to build a VUV Raman spectrometer as a permanent end-station.

From the experimental point of view, the successful realization of RIXS experiments puts high demands on the instrument, especially when low-energy excitations with typically sub 50 meV excitation energies are studied and interaction cross-sections are small. To meet this purpose, a two-stage double monochromator Raman spectrometer with an intermediate slit was designed (Rusydi *et al.* 2014; Rübhausen *et al*. 2004). Each spectrometer stage works according to the Czerny-Turner optical scheme and enables aberration-free spectral imaging on the optical axis. In order to achieve superior resolution and stray light rejection, the design also requires special care in the alignment of the instrument. One of the most crucial aspects of the confocal operation mode with an intermediate slit is that the position of the intermediate focal plane must remain fixed for all photon energies or consequently for all possible angles of the diffraction grating. Therefore, three different techniques were combined in order to align the optical components and verify their aligned state. As the main alignment technique optical laser interferometry was employed. It allows evaluating the quality of the laser wavefront behind different optical elements of the monochromator with the precision on the order of the wavelength of light used (here 633 nm). Complementary, wavefront sensing using a Hartmann-Shack wavefront sensor (LOT; Schäfer et al. 2006) was used and the results obtained, were cross-checked with the ones from the optical laser interferometry studies. Finally, the alignment quality of the monochromator was validated by employing an off-line X-ray source, which has been

adapted to provide soft X-ray photons. This could be used to perform systematic performance tests in the energy region of interest and independent of the FEL availability.

2. VUV Raman spectrometer overview

The high-resolution double stage VUV Raman spectrometer is a permanent end-station of the PG1 branch of the plane grating monochromator beamline at FLASH (Martins *et al*. 2006; Dziarzhytski *et al*. 2016; Tiedke *et al*. 2009). This instrument has been developed at the University Hamburg in collaboration with DESY for inelastic scattering (Raman) experiments in the soft X-ray spectral region from 20 to 200 eV, intended to provide an unprecedented spectral resolution of 2-15 meV and superior stray light suppression, which allows studies of low energy quasiparticles in various solid samples. The spectrometer design is based on a confocal additive arrangement of two high-resolution monochromator stages, shown of Fig.1 (Rusydi *et al*. 2014, Rübhausen *et al*. 2004). In brief, the sample is located in the sample chamber and emits under illumination with the FEL radiation elastically and inelastically scattered photons. Both types of photons are collected by the first monochromator stage. This stage acts also effectively as an entrance objective that collects a relatively large solid angle and reduces the stray-light by several orders of magnitude by predispersing the light separating the elastic from the inelastic contribution. A slit mechanism situated between the monochromators allows only photons into the second stage that are inelastically scattered. The second stage is the spectrograph stage that disperses the light further onto the detector plane, where the spectrum is recorded by an intensified charged coupled camera (ICCD). Each monochromator chamber, shown in Fig. 1 as SP1 and SP2 houses two off-axis parabolic mirrors for light collimation and focusing and a grating bench that can hold up to 4 optical gratings. The schematic layout of the monochromator is depicted in Fig.1.

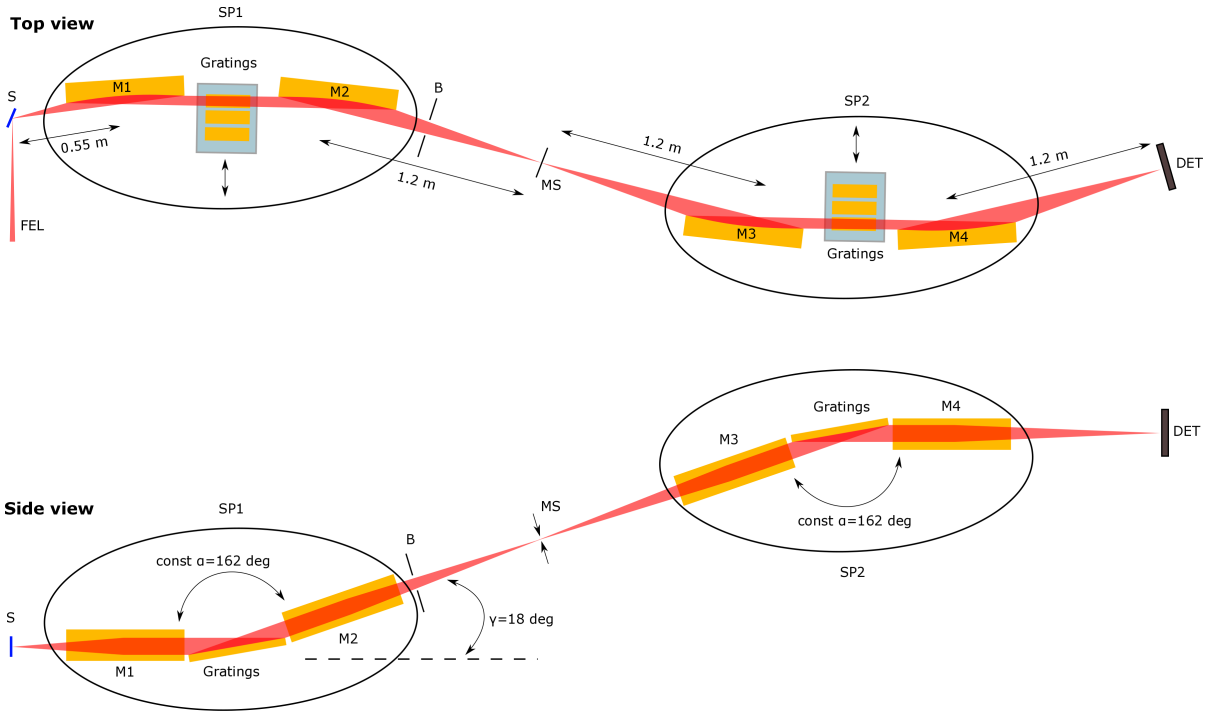

Figure 1 Optical scheme of the VUV Raman spectrometer. M1-M4 off-axis parabolic mirrors, MS middle slit, B baffle system, S sample, DET detector camera. SP1, SP2 monochromator chambers.

The sample S is located in the focal point of the first off-axis parabolic (OAP) mirror M1. The scattered light is collimated and directed onto the grating unit G1. Note, that in both monochromator stages the parabolic mirrors deflect the beam perpendicular to the dispersion plane. Thus, the light is focused along the short axis of the parabola (sagittal focusing), reducing the influence of optic slope errors. The maximum acceptance angle of M1 is 37×82.6 mrad (v×h). G1 works in inside order orientation. The vertically dispersed photons are collected and focused onto the intermediate slit (labelled “MS” in Fig 1.) by the second OAP mirror M2. As mentioned before, the light transmitted through the intermediate slit is then collected and further dispersed by the second monochromator stage in a similar fashion. The Raman spectrometer works with a constant included angle of 162°, thus the mirror positions are fixed, only the gratings have to be rotated in order to choose or scan the wavelength, enabling the operation as a double monochromator. By using the gratings in zeroth order, any wavelength can be focused. This property is used in the alignment process of the instrument.

The grating unit G1 of the first monochromator stage hosts two diffraction gratings: G1-3 and G1-4 with a groove density of 576 lines/mm and 1120 lines/mm, covering the spectral energy range of 36-144 eV and 70-210 eV, correspondingly. Gratings are switched between each other by moving them transversely to the beam in horizontal plane (see Fig.1). In addition, a plane mirror is installed and can be used instead of the diffraction grating in case a higher throughput is needed.

3. Alignment

In this section we present the procedure and the results of the internal optical alignment of the single VUV Raman monochromator SP1. The optical alignment approach was based on using a Laser Unequal Path Interferometer (LUPI) from Space Optics Research Lab, coupled with a 90° off-axis focusing parabolic mirror (FP), to provide a source point for the VUV Raman monochromator (see Fig. 2). A single mode He-Ne laser with central wavelength of 633 nm is used to provide the laser beam for the interferometric alignment. LUPI and FP were mounted as one unit on a common laser breadboard, installed on a hexapod from Physik Instrumente (PI, model number H-850.H2). This allowed precise control over the source point position and its fine-tuning. Complementary, the evaluation of the alignment quality was performed via wavefront-sensing measurements (Keitel *et al*. 2016).

The alignment procedure consists out of four major steps that will be further discussed in the following:

1) Alignment of the FP
2) Alignment of the LUPI stage with respect to the OAP mirror M1
3) Alignment of the gratings at unit G1 (one-by-one)
4) Alignment of the OAP mirror M2

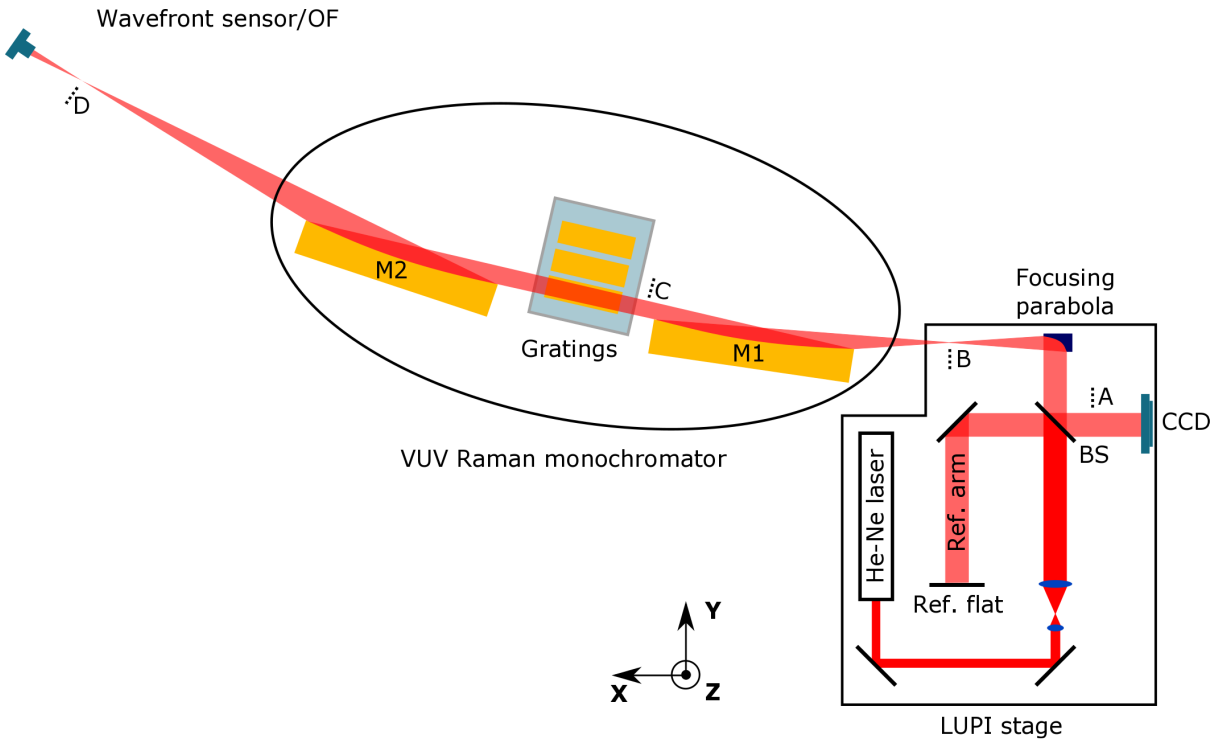

Figure 2 Optical scheme of the LUPI stage, coupled to the VUV Raman monochromator chamber. The beamspliter (BS) splits the beam from the single mode He-Ne laser into reference and test arms and recombines them again on the CCD. The beam in the test arm is focused by the FP to create a source point for the M1 mirror of the monochromator. During different stages of the alignment process, optical flat mirror (OF) has to be placed at points B, C, and D. An imaging lens can be placed at a position A for the pre-alignment purposes. A retroreflector was used at position C as explained in section 3.2.

3.1. Interferometer preparation

At a first alignment step, the laser beam in the test arm of the LUPI spectrometer has to be focused to create a source point for the first mirror M1 of the VUV Raman spectrometer. Considering the numerical aperture of the OAP mirror M1 and the need to fold the laser beam due to space constraints in the FLASH experimental hall, a 90° OAP mirror with parental focal distance of 75 mm was used. The surface quality of this OAP mirror is $\lambda/4$. The mirror is 1inch in diameter, which corresponds to an f-number of 5.91. Given the smaller f-number of the focusing parabola, compared to that of M1, means that the mirror M1 is over illuminated by the FP. Thus only the central part of the wavefront with the highest quality, provided by the FP, will illuminate M1 and participate in the formation of the interference pattern. The FP is placed in a kinematic mount which allows pitch, roll and yaw adjustments. The alignment was performed according to the scheme depicted in Fig.2. A high quality ($\lambda/20$) optical flat mirror (OF) was placed in the focal point of the FP (position B) and the pairs of degrees of freedom pitch/yaw of the focusing parabola and tip/tilt of the OF were altered together to achieve a parallel and uniformly distributed fringes in the interferogram.

3.2. Alignment of the interferometer to mirror M1

In order to bring the source point of the LUPI close enough to the focus of mirror M1 and to obtain a visually resolvable interference pattern which then could be further corrected, a prealignment step is needed (www.sorl.com; Barkhouser and Raymond 1999). For this purpose, a glass retroreflector prism (surface quality $\lambda/10$) was placed behind M1 at a distance of approximately 10 cm (Fig.2, point C). The beam in the reference arm was blocked and an imaging lens was put into the test arm in front of the CCD camera such that the camera is in the focus of the lens (Fig.2, point A). This allowed the observation of the return spot from the test arm, focused on the CCD (see Fig.3). The goal of this pre-alignment step was to achieve the best possible focusing of the return spot. As a retroreflector always provides backreflection, only adjustments of the hexapod in X, Y and Z coordinates were needed. The initially obtained shape of the return spot was a skewed line. Vertical adjustment of the hexapod (Fig.3 (a)-(c)) corrected the angle of the line towards the horizontal, thus removing the XY component of the observed astigmatism. Continuous horizontal adjustment (Fig.3 (d)-(f)) allowed focusing of the return beam to the smallest possible round-shaped spot, meaning that this pre-alignment step is

complete. After finishing the pre-alignment, the retroreflectror was replaced with the high quality optical flat mirror, the imaging lens was removed and the beam in the reference arm was unblocked, thus revealing an interference pattern on the CCD chip. Further and therefore more precise alignment is achieved by adjusting the horizontal/vertical position of the source point followed by a tip/tilt correction of the OF.

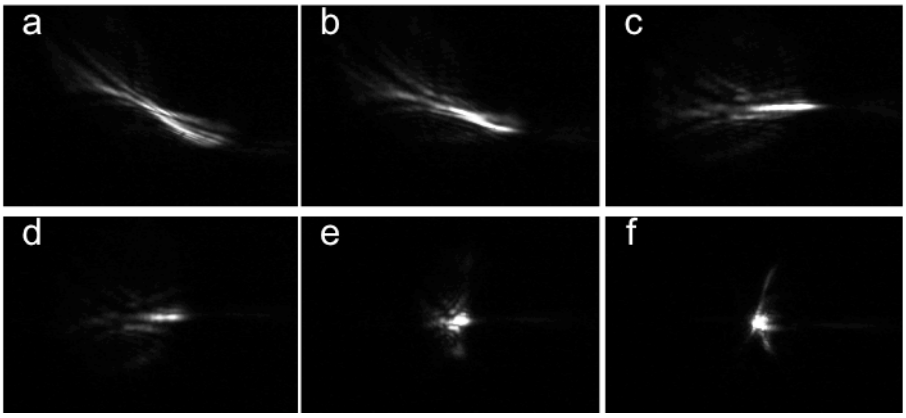

Figure 3 Return spot from M1, focused on the CCD chip. (a)-(c) correction of the vertical error. (d)-(e) shrinking of the line profile into a spot by gradual correction of the horizontal error.

A sequence of interferograms, showing progressive vertical and horizontal alignment is presented in Fig.4. The obtained pattern is cross-like with an additional tilt, indicating both Y^2-X^2 and XY astigmatism, according to Zernike theory (Born and Wolf 1965). Such a pattern appears due to a wrong height and off-axis distance(OAD) of the source point with respect to the mirror M1. The correction of the vertical offset (Fig.4 (a)-(c)) results in a gradual rotation of the "cross" such that it is symmetric with respect to the center horizontal and vertical lines. This adjustment removes the XY components of the astigmatic aberration. As soon as this is achieved, the OAD needs to be corrected. A shift of the source into the correct direction results in the enlargement of the cross and finally in its transformation into a set of concentric circles (Fig.4 (d)-(f)). The next alignment step is adjusting the source to the correct focal distance. Again, a shift in the correct direction along the M1 optical axis enlarges the circles and increases the period of the interference pattern.

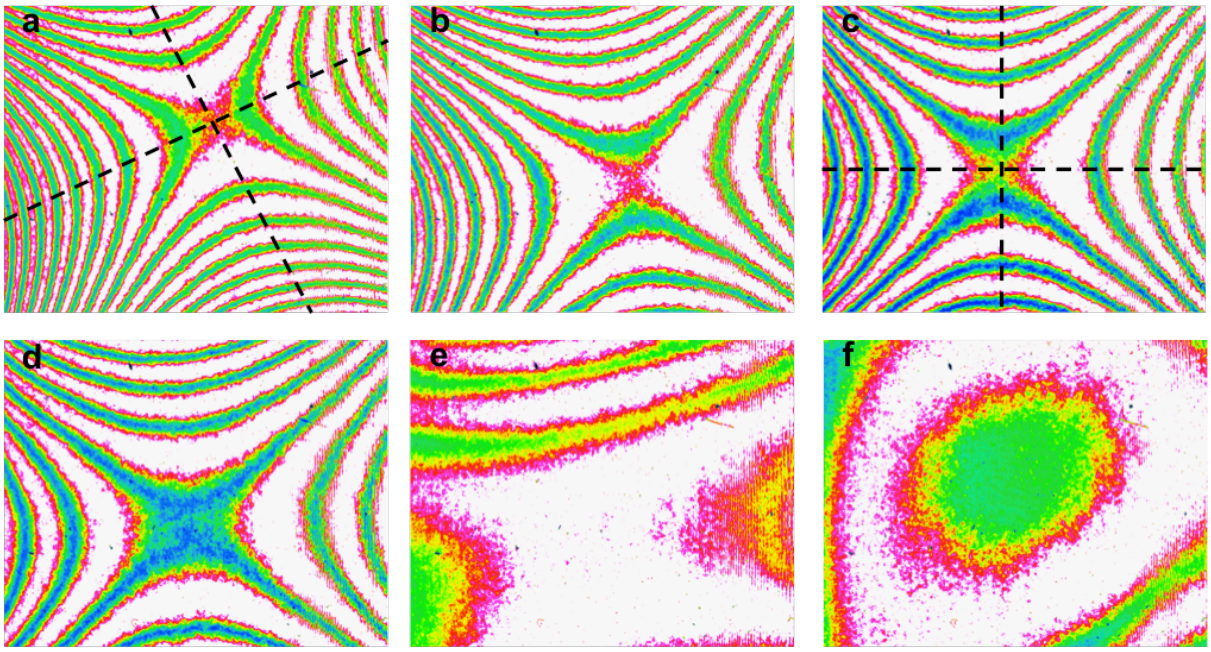

Figure 4 Interferograms showing the alignment of the LUPI to the M1 mirror. OF was used to provide backreflection on M1. (a)-(c) progressive vertical alignment leads to the rotation of the astigmatic „cross“ pattern. (d)-(f) good vertical and progressive horizontal alignment. Some residual vertical misalignment becomes visible on image (f).

Finally, a uniform intensity distribution (piston) can theoretically be achieved, meaning that two plane parallel waves interfere. Vibrations in the experimental hall and air turbulences can obscure the interference pattern and residual aberrations, which makes further improvements challenging. In particular when the source point is very close to the M1 focus and the observed fringes period is such that not more than 1-2 fringes are visible. Therefore, after obtaining a piston-like pattern, a tilt was introduced to the system deliberately. This was achieved by tipping/tilting the reference flat to observe 5-7 horizontal and vertical lines in the pattern, respectively. The goal was to make them symmetric around the imaginary line that goes through the center of the interference pattern, perpendicular to the fringes (see Fig.5). This would mean that the reflected wavefront in the reference arm is flat and the source point is in the focus of M1.

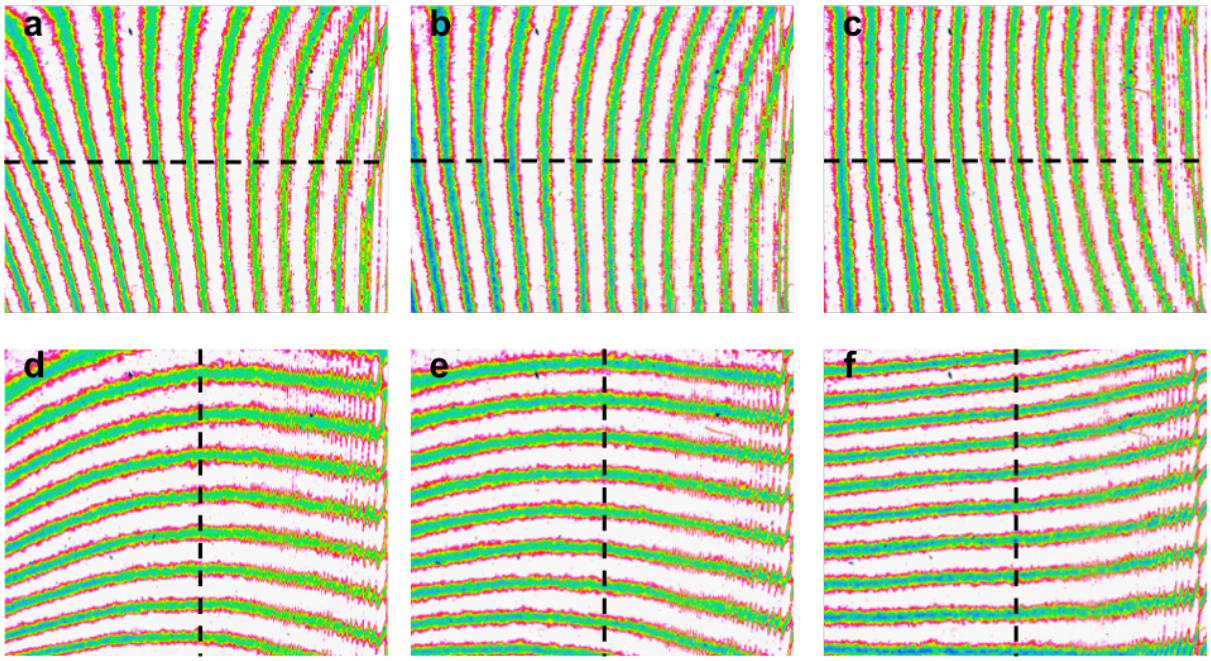

Figure 5 Introduction of the tilt into the system for visualisation of the residual aberrations and their consequent correction. (a)-(c) correction of the vertical error. (e)-(f) correction of the horizontal error. (c) and (f) are the final interference patterns.

First, the reference flat mirror of the LUPI was tilted to obtain vertical lines in the pattern. The vertical position of the source point, was adjusted together with the tip of the OF to achieve the required symmetry condition (Fig.5 (a)-(c)). After that, the reference flat was adjusted to observe horizontal fringes. OAD of the source point and tilt of the OF were optimized to form parallel and straight fringes (Fig.5 (e)-(f)). Fig.5(c) and (f) show the final optimized patterns.

After having aligned the LUPI system to M1, the optical flat mirror was removed and the spectrometer grating bench was rotated into a 90° configuration perpendicular to the optical axis of M1, in order to provide back-reflection of the collimated light on M1. This configuration allowed aligning all gratings installed to have identical interference patterns. This ensures that the imaging properties of the spectrometer as well as its resolution will not depend on the grating that is being used. The obtained interferograms of the installed gratings and the mirror blank are compared in Fig.6.

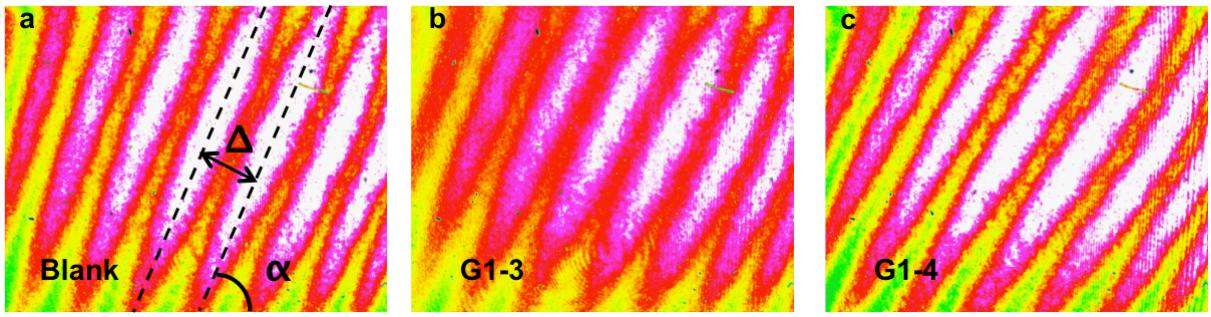

Figure 6 Tilt fringes, showing resulting alignment of the blank mirror (a) and the installed diffraction gratings (b), and (c). The patterns are obtained, by placing the above mentioned optical elements (diffraction gratings, blank mirror) in the 90° orientation, to provide backreflection on M1. The identical tilt of the fringes and their equal periods confirm their proper alignment with respect to each other and to the mirror M1.

3.3. Alignment of the mirror M2

After having aligned the LUPI-M1-gratings systems, the grating bench was returned to its nominal 0^{th} order diffraction position of 9° relative to the optical axis of M1, and the OF was placed on a high-precision translation stage in the focus of the parabolic mirror M2 (see Fig.2, point D). The interference pattern showed presence of both Y^2- X^2 and XY astigmatism contributions. The latter could be corrected by either changing the pitch of the grating bench or the yaw angle of the mirror M2. The correction of the XY astigmatism was achieved by small adjustment of the 0^{th} order angle of the grating bench by less than 2 mrad.

In order to obtain a full quantitative analysis of the remaining aberrations we switched from interference pattern measurements to wavefront sensor measurements. A direct measurement of the wavefront eliminates the issue of low contrast in the interference pattern due to intensity attenuation of the light in the test arm of the LUPI, compared to it's reference arm. The reason for the low intensity is simply because of six additional reflections from M1-blank mirror-M2 upon forward and backward light propagation, considering that the mirror diamond-like carbon coating is optimized for VUV photons.

Wavefront measurements were carried out using a Hartmann-Shack wavefront sensor from Laser-Labratorium Göttingen e.V (LOT). It is sensitive in the wavelength range of 350 nm – 1100 nm and consists of a 12 mm x 12 mm microlens array in a focal distance of 3.6 mm to the CCD camera. The lenses are 150 µm x 150 µm in size. The 12 bit CCD camera has a resolution of 1280 x 1040 pixels with a field of view of 8.25 mm (h) x 6.6 mm (v). The absolute accuracy at 633 nm is between λ/50 to λ/150, with a relative sensitivity up to λ/10000.

Wavefronts, showing the alignment procedure of the M2 mirror together with the focal spots retrieved by Fresnel back-propagation of the measured intensity distribution are presented in Fig. 7. The first Zernike aberrations for each wavefront were calculated using the Arizona-Fringe notation with 37 polynomials and are summarized in Table 1 (Laser Beam Profiler MrBeam 1997-2017).

In the upper row of Fig. 7 the measured wavefronts behind the mirror M2 are shown at the position of the wavefront sensor which was installed ~30 cm behind the focus position of M2. In Fig. 7(a) the initial wavefront behind the mirror M2 prior to correction of the 0th order angle of the grating bench is dominated by the Y^2-X^2 astigmatic contribution, in agreement with the interferometric

measurements. Optimization of the M2 pitch angle corrects the Y^2-X^2 component of the astigmatism (Fig 7(b)), leaving the XY one. Finally, correction of roll and x of the M2 mirror eliminates the remaining aberrations and yields to the final wavefront, shown in Fig.7(c). The peak-to-valley value for each wavefront is given in λ and could be reduced to about half of the initial value. The size of the focus could significantly be reduced to a round shape of about 25.5 µm each in x and y direction.

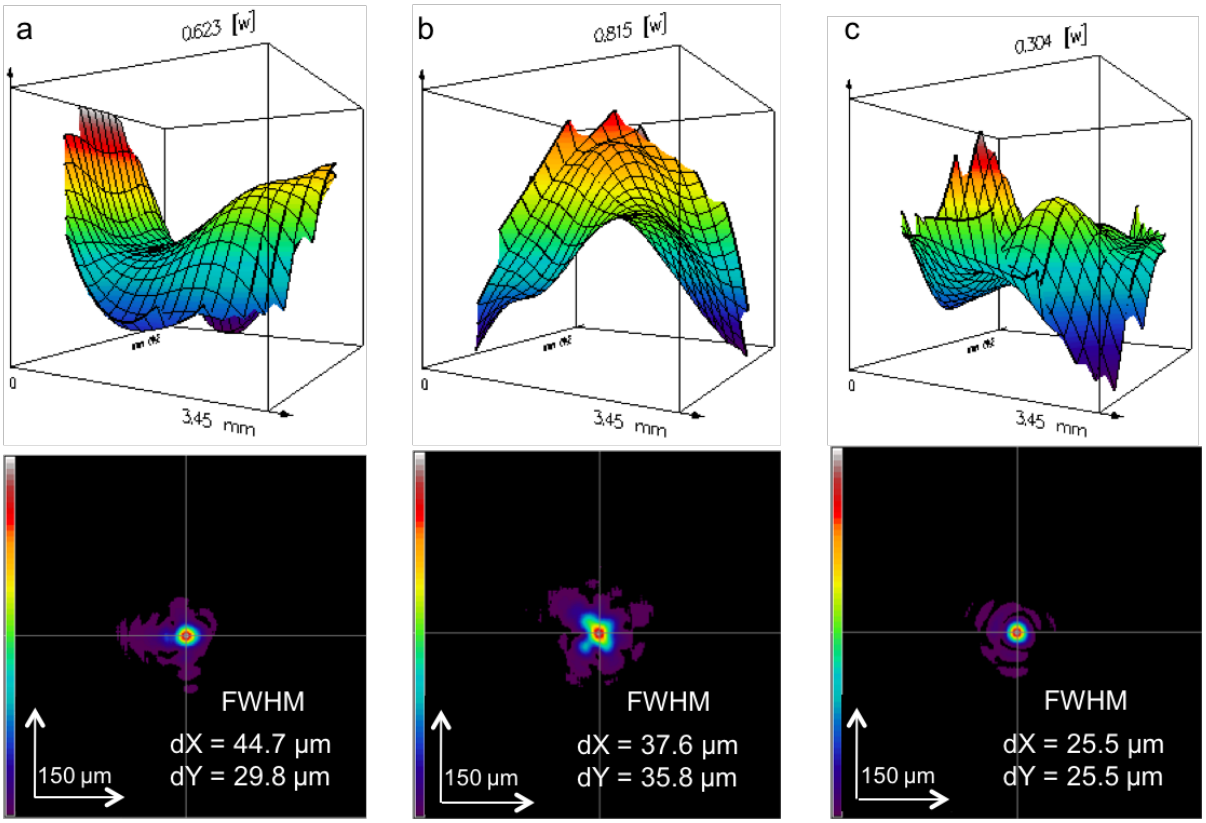

Figure 7 In the upper row measured wavefronts behind the mirror M2 are shown at the position of the wavefront sensor. The inital wavefront shows dominant presence of astigmatic contributions (a), wavefront after pitch optimization of M2 (b) and the final wavefront after alignment of roll and x of M2 (c). The peak-to-valley value for each wavefront is given in λ and could be reduced to about half of the initial value. The lower row shows the intensity profiles at the focus position of M2. They were retrieved by Fresnel back-propagation of the intensity profile measured at the position of the wavefront sensor. The focus size in x and y direction is given in fwhm for the cross marked positions. The focus size could significantly be reduced to a round shape of about 25.5 µm each in x and y direction.

Table 1 Zernike aberrations, corresponding to the wavefronts of Fig. 7 for λ=633 nm.

Zernike aberrations	(a)	(b)	(c)
Astigmatism Y^2- X^2	0.237 λ	0.115 λ	0.021 λ
Astigmatism XY	0.079 λ	0.375 λ	0.002 λ

Coma X	0.109 λ	0.071 λ	0.077 λ
Coma Y	0.009 λ	0.032 λ	0.000 λ
Triangular coma	0.051 λ	0.019 λ	0.049 λ
Quadratic astigmatism	0.008 λ	0.038 λ	0.017 λ
Spher. aberration	0.008 λ	0.046 λ	0.016 λ

After completion of the M2 alignment, OF was returned to the focus of M2 and gratings bench was scanned, yielding final interference patterns of the aligned SP1 optical elements (Fig. 8) with different gratings of the monochromator chamber, installed in the beam and confirming proper alignment of the system. The best straightness and parallel nature of the interference pattern can be obtained for the blank and grating G1-3, whereas G1-4 shows a slightly increased tilting of the interference fringes.

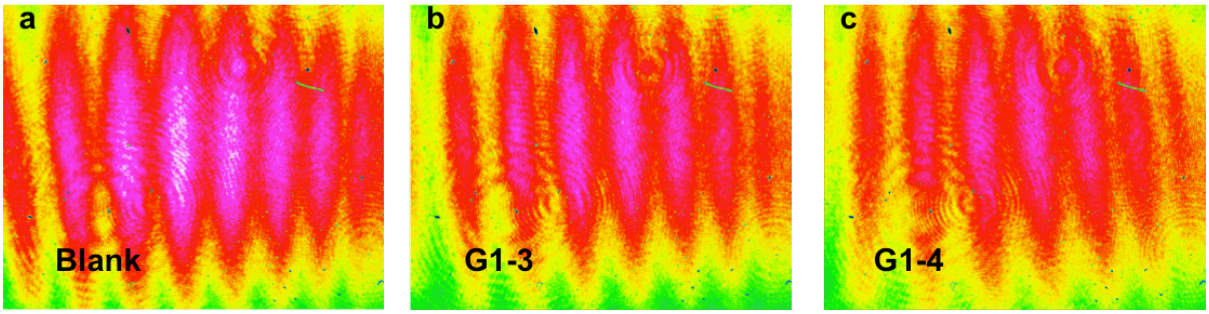

Figure 8 The interference fringes, showing the final alignment of the blank mirror (a) and diffraction gratings (b), (c). The patterns were obtained after M2 alignment with OF placed in M2 focus. The identical tilt of the fringes and their equal periods indicate interference of two plane waves thus confirming proper alignment of the optical elements with respect to each other as well as to the mirrors M1 and M2.

4. Offline X-Ray measurements

After completion of the interferometric alignment with visible photons, the performance of the spectrometer was characterized in the soft X-ray range utilizing a special X-ray tube, the so called "Manson's source" McPherson Light source, model 642, depicted in Fig.9. The source is equipped with a 200 µm pinhole rigidly mounted in front of the photon emitting anode at the distance of 16 mm (see Fig. 9). For spectrometer performance characterization, the photon emission at the $L_{2,3}$-edges of the Al edge of the Al-Mn anode was investigated. The chamber with the X-ray tube was mounted on the hexapod instead of the LUPI interferometer and the pinhole was brought to the M1 focus. Both, the Manson's source pinhole and the LUPI pinhole were fiducialised in advance. The replacement of the LUPI with Manson's source was performed under surveying with approx. 300 µm precision. The wavefront sensor (Fig.1) was replaced by an ICCD camera from Princeton Instruments (PIXIS-XO

2048B), attached to the spectrometer chamber via the metal bellows and placed in the nominal focal position. The mounting platform below the ICCD camera is motorized and allows moving the camera along the optical axis of M2. The entire system, consisting of the monochromator and the ICCD camera acts like a one-stage spectrometer. A 3D scan of the source position combined with a longitudinal scan of the ICCD position was performed with spectrometer in 0^{th} order (imaging mode) to bring the x-ray source exactly to the M1 focus with an accuracy of 50 µm. An optimized pinhole image was obtained at the position of the ICCD camera x_0=125 mm in our coordinate system.

The spectrometer performance in the soft X-ray range was tested in terms of imaging properties in 0^{th} diffraction order, in terms of spectrally resolving properties in 1^{st} and 2^{nd} diffraction orders as well as simulations were done for a comparison. These verification steps will be discussed in more detail in the following sections.

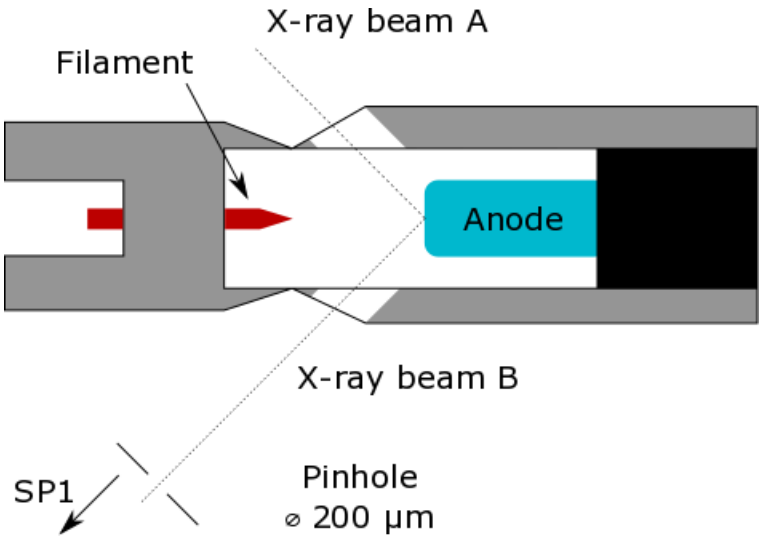

Figure 9 Schematic drawing of the X-ray source, used in verification of the spectrometer performance. The pinhole is located 16 mm away from the anodes surface.

4.1. Comparison of the SHADOW simulations with X-ray source experiment

Prior to performing the alignment procedure and experimental studies with the Manson's source, the first monochromator stage and the source have been extensively studied in terms of possible effects of optics and source point misalignments via ray tracing using SHADOW software package (Cerrina and Sanches 2010).

The source for the ray tracing has an uniform photon energy distribution from 73.1 eV to 61.1 eV to mimic the 12 eV energy width of the Al $L_{2,3}$ emission line (Neddermyer *et al*. 1970; Ederer *et al*. 1988; Poletto *et al*. 1999), circular shape with radius of 0.3 mm, and a uniform divergence of 14 mrad in fwhm.

Specifications and slope errors of the optical elements of the first monochromator used for the ray tracing can be found in (Dziarzhytski *et al.* 2018). Here, the only difference is that an additional circular pinhole with 0.1 mm radius is placed at the distance of 550 mm in front of the first parabolic mirror M1, i.e. in its focus. The source is placed at the distance of 566 mm from the mirror M1, which corresponds to the actual distance of 16 mm between the anode surface and the limiting pinhole.

As discussed in Sec.2 the spectrometer disperses the collected light in the vertical plane, therefore the vertical source size and its spectral bandwidth defines the spectral resolution of the spectrometer to a large extend. The calculated highest spectral resolution of the spectrometer at 73 eV photon energy presuming a vertical source size of 200 µm is 220 meV for the grating G1-3 (576 l/mm groove density) and 90 meV for G1-4 (1120 l/mm groove density), respectively, both working in the 1st diffraction order. The resolution of the spectrometer with G1-3 grating in 2nd diffraction order at the same photon energy is 85 meV.

Ray tracing results for the spectrometer imaging properties in 1st diffraction order along the beam caustic in comparison with experimentally recorded images of the pinhole are shown in Fig. 10. The detector plane has been shifted upstream and downstream by 35 mm relative to the nominal focal position (see Fig. 10 (a), (b) and (c)). A change of the slope of the high energy flank (right side) along the caustic is observed in both simulations and experiment. The line is added as an eye guide in the figures. Such a change of the flank leads to a decrease of the spectrometer resolution due to smearing out the sharp L_3 rising edge and L_2 peak while binning. This criterion was used in the measurements with the X-ray tube to define the focal position of the SP1 monochromator unit.

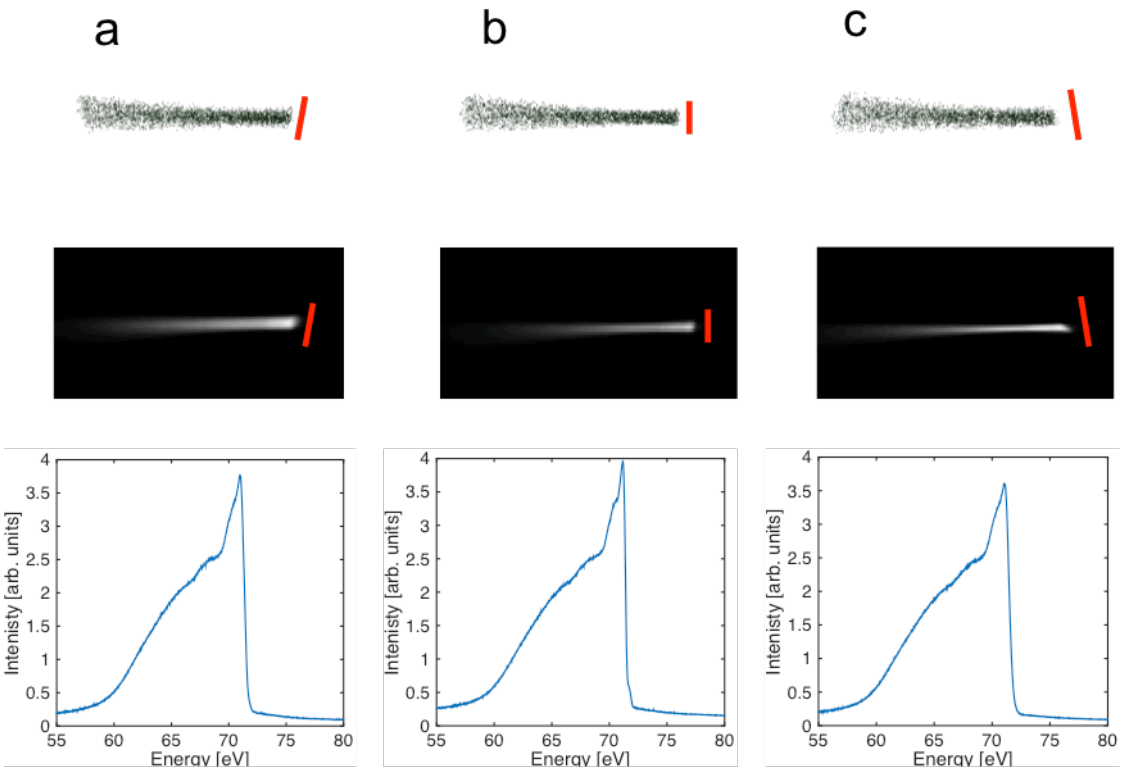

Figure 10 Simulated (top row) and measured (middle row) 2D images of the Al $L_{2,3}$ band as well as projected intensity profiles (bottom) for different longitudinal positions of the detector: -35 mm from the nominal focus (a), in focus (b) and +35 mm from the focus (c)). Change of the slope of the high energy flank (right side) along caustic is observed in both simulations and experiment. The line is added as an eye guide. Energy is increasing from left to right.

4.2. Determination of the focal position

Aberrations lead to the distortion of the image in the 1st order, resulting in a decrease of the slope of the rising edge of the Al L_3 emission peak and smearing out spin-orbit coupling, thus providing a good criterion for the position of the focal plane of the spectrometer and its resolution. This criterion is especially applicable, because Al L_3 edge has a sharp rising edge near the Fermi energy E_f, which is mostly broadened due to instrument response function (Neddermyer *et al*. 1970; Ederer *et al*. 1988; Poletto *et al*. 1999). The longitudinal position of the ICCD camera was scanned within ±35 mm range from the position, where the best 0th order image was found. The recorded spectral intensity distribution at each detector position was background corrected and integrated within the region of interest, yielding the Al $L_{2,3}$ X-Ray fluorescence spectrum (Fig. 10, bottom). The slope of the rising edge of each spectrum was calculated as the average of 5 highest values of the 1st derivative of the measured spectrum in the vicinity of the rising edge (see Fig. 11(a), (b)). Error bars were extracted as a standard deviation for these 5 points. Slope dependencies for each grating were normalized to 1. Measurements were performed for grating G1-3 in 1st and 2nd diffraction orders, mimicking different photon energies, and for G1-4 in 1st diffraction order. Results of the analysis are presented in Fig. 12, and are summarized in Table 2. As one can see, the maxima for all scans are within the range of 123.2-125.3 mm, whereas the optimum 0th order image was found to be at 125 mm. This confirms that the position of the focal plane for both gratings doesn't change within the measurement precision when going from 0th diffraction order to 73 eV for G1-4 grating and 73 eV and 36.5 eV energies for G1-3 grating, respectively. This ensures that the spectrum after the first monochromator stage will always be projected onto the fixed intermediate slit plane, most efficiently suppressing the stray light and coupling the desired energy window correctly into the second monochromator.

A zoom to the rising edge region of the Al $L_{2,3}$ spectrum, confirming the improvement of the resolution and formation of the L_2 pre-edge (inset) upon correction of the ICCD longitudinal position is presented in Fig.11(a).

Estimated widths of the L_3 edge as a measure of the spectrometer resolution recorded with different gratings and diffraction orders are compared with theoretical ones as obtained in the ray-tracing and are summarized in Table 3. Table 3 shows, that for grating G1-3, both, first and second order resolutions as determined by our experiments match the ray tracing results within the experimental resolution. Grating G1-4, however, which should show a similar resolution than G1-3 in second order

exhibits a performance, which is about a factor of two off. This might be connected to a number of factors indicating a worse quality of G1-4 such as grating inhomogeneities, which are difficult to address through a ray-traycing simulation. Furthermore , as already discussed for Fig. 8 the interferences fringes in Fig. 8 (c) do not show the same quality of the straightness and are not as parallel to each other as compared to Grating G1-3. Together this can result very well in the reduced resolution of grating G1-4.

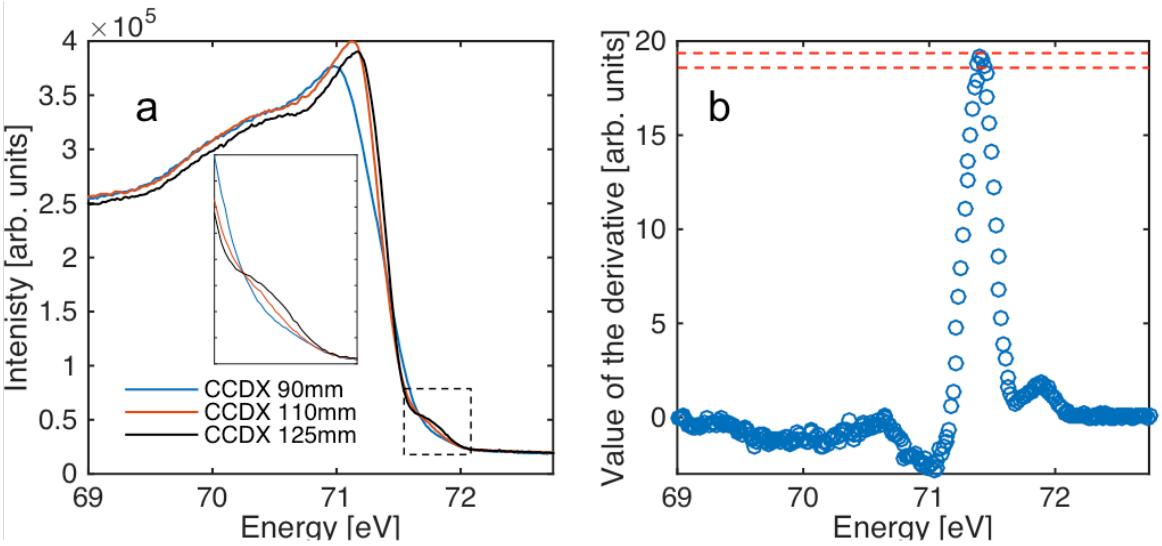

Figure 11 (a) Formation of the pre-edge feature at 71.8 eV and decrease in the slope of the rising edge of the Al $L_{2,3}$ spectrum upon approaching to the CCDX=125 mm position. (b) Example of the derivative used for the slope analysis (first derivative of the spectrum, measured with the G1-3 grating in 1st diffraction order at CCDX=125 mm). Red lines indicate the borders of the range, within which the average value of the derivative and the error bar are calculated.

Table 2 Positions of the maximum of the parabolic fit with 90% confidence band to the experimentally measured dependencies of the slope of the rising edge of Al $L_{2,3}$ X-ray fluorescence. Optimum 0th order position is at 125.0 mm.

G1-3 1st order	G1-3 2nd order	G1-4 1st order
123.2±3.2 mm	125.3±3.5 mm	123.9±3 mm

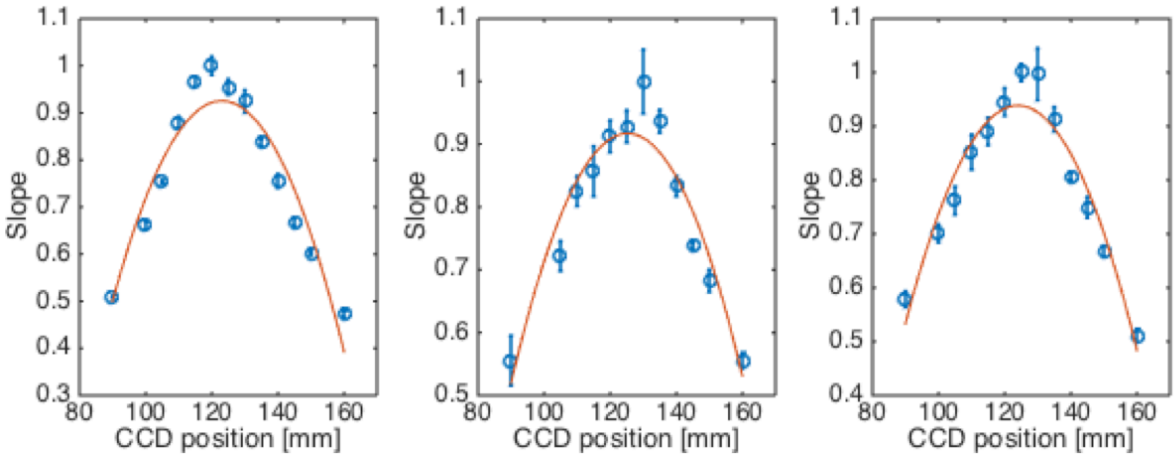

Figure 12 Increase in the slope of the rising edge of the Al $L_{2,3}$ X-ray fluorescence spectrum for G1-3 grating in 1st order (left), G1-3 in 2nd diffraction order (middle) and G1-4 in 1st diffraction order (right) upon approach of the CCD position to 125 mm. Red line is the fit of the parabolic function to the data.

Table 3 Comparison of the spectrometer resolution measured with Manson's source and calculated in SHADOW

Grating	G1-3	G1-3	G1-4
Photon energy	73 eV	36.5 eV	73 eV
Experiment	239±24 meV	102±10.2 meV	200±20 meV
Theory	220 meV	85 meV	90 meV

4.3. Conclusions

In this work an advanced alignment concept was applied to the VUV Raman monochromator. Optical laser interferometry measurements together with wavefront measurements were used to align the monochromator. Both methods qualitatively and quantitatively verify the alignment. The aligned state of the instrument was further confirmed in the VUV energy range by investigating the X-ray fluorescence at the Al $L_{2,3}$ edge with the help of an off-line X-ray source compared with SHADOW ray-tracing results. Taking into account that the investigated effective energy range covers almost the entire working range of grating G1-3 and the identical interferometric alignment of both gratings, we can conclude that the spectrometer performs within its design specifications.

4.4. Acknowledgement

The authors acknowledge the funding by the Deutsche Forschungsgemeinshaft DFG (FOR1405) via Ru-773/6-2 and Ru-773/4-2. In addition, we appreciate very much the help of the MEA2 group DESY

for the fiducialization and surveying of the experimental equipment. We are also very thankful to Luca Poletto (CNR - Institute of Photonics and Nanotechnologies) who provided the X-ray source and Martin Beye (DESY-FLASH) for useful discussions.

5. References

Ackermann et al., (2007). Nature Photonics, 336-342.

Ament L. J. P. et al., (2011). Rev. Mod. Phys., 83, 705.

Barkhouser, R. H., Raymond G. Ohl (1999). Proc. SPIE. Vol. 3782, 601-614.

Born M. and Wolf E. (1965). Principles of Optics (Pergamon, New York), Sec. 9.2.

Cerrina, F. and Sanches del Rio, M. (2010). Handbook of Optics, 3rd ed., ch. 35 New York: McGraw Hill.

Dziarzhytski, S. et al., (2016). J. Synchrotron Rad. 23, 123-131.

Dziarzhytski, S. et al., (2018). J. Synchrotron Rad. 25, 138-144.

Ederer, D. L. et al. (1988). Phys. Rev. B, V. 37, 15, p. 8594 – 8597.

Keitel, B. et al., (2016). J. Synchrotron Rad. 23, 43-49.

Kotani, A., Shin, S. (2001). Reviews of modern physics, Volume 73, No.1

Laser Beam Profiler MrBeam V.3.7.0 (1997-2017). Laser-Laboratorium-Göttingen

LOT. https://lot-qd.de/de/produkte/licht-laser/laser-beam-diagnostics/product/hartmann-shack-wellenfrontsensor-1/

Manual from SORL

Martins M. et al., (2006). Rev. Sci. Instrum. 77, 115108.

Neddermeyer, H. & Wiech, G. (1970). Phys. Lett., v. 31A, 1, p. 17-18.

Plönies, E., Tiedtke, K. (2015). Optical technologies for Extreme-Ultraviolet and Soft X-ray Coherent

Poletto, L., Boscolo, A. and Tondello, G. (1999). SPIE Proc. Vol 3764, Ultraviolet and X-Ray Detection, Spectroscopy and Polarimetry III, 94-102.

Rusydi, A. et al., (2014). Phys. Rev. let. 113 (6), 067001.

Rübhausen, M. et al., (2004). Technical Design Report. BMBF project number 05KS4GU2.

Sources, edit by Canova, Frederico, Poletto, Luca. Springer series in optical sciences, Vol. 197, Springer Heidelberg.

Schäfer B. et al., (2006). Review of Scientific Instruments 77, 053103.

Tiedke K. et al., (2009). New Journal of Physics 11, 023029.

Bibliography

[1] Edward I. Solomon, David E. Heppner, Esther M. Johnston, et al. Copper active sites in biology. *Chemical Reviews*, 114:3659–3853, 2014.

[2] Gaspar Ana B, Vadim Ksenofontov, Maksym Seredyuk, and Philipp Gütlich. Multifunctionality in spin crossover materials. *Coordination Chemisrty Reviews*, 249:2661–2676, 2005.

[3] Helmut Beinert. Copper a of cytochrome c oxidase, a novel long-embattled, biological electron-transfer site. *Eur. J. Biochem.*, 245:521–532, 1997.

[4] Liviu M. Mirica, Xavier Ottenwaelder, and T. Daniel P. Stack. Structure and spectroscopy of copper-dioxygen complexes. *Chem. Rev.*, 104:1013–1045, 2003.

[5] Sonja Herres-Pawlis, Ulrich Flörke, and Gerald Henkel. Tuning of copper(I)-dioxygen reactivity by bis(guanidine) ligands. *Eur. J. Inorg. Chem.*, pages 3815–3824, 2005.

[6] Antonin Vlček Jr. Mechanistic roles of metal-to-ligand charge-transfer excited states in organometallic photochemistry. *Coordination Chemistry Reviews*, 177:219–256, 1998.

[7] Edward I. Solomon and Ryan G. Hadt. Recent advances in understanding blue cooper proteins. *Coordination chemistry Reviews*, 255:774–789, 2011.

[8] Philipp Gütlich, Yann Garcia, and Harold A. Goodwin. Spin crossover phenomena in fe(II) complexes. *Chem. Soc. Rev.*, 29:419–427, 2000.

[9] Robert J.P. Williams. Energised (entatic) states of groups of secondary structures in proteins and metalloproteins. *Eur. J. Biochem.*, 234:363–381, 1995.

[10] Bert L. Vallee and Robert J.P. Williams. Metalloenzymes: The entatic nature of their active sites. *Proc. Natl. Acad. Sci. USA*, 59:498–505, 1968.

[11] Alexander Hoffmann, Stephan Binder, Anton Jesser, et al. Catchning an entatic state-a pair of copper complexes. *Angewandte Chemie*, 53:299–304, 2014.

[12] Sonja Herres-Pawlis, Stephan Binder, Andreas Eich, et al. Stabilization of a highly reactive bis(mu-oxo)dicopper(III) species at room temperature by electronic and steric constraint of an unconventional nitrogen donor ligand. *Chem. Eur. J.*, 15:8678–8682, 2009.

[13] Patricia Liebhäser, Alexander Hoffmann, and Sonja Herres-Pawlis. Tyrosinase model systems. synthesis, spectroscopy, theory and catalysis, 2016.

[14] Laura Santagostini, Michele Gullotti, and Enrico Monzani. Reversible dioxygen binding and phenol oxygenation in a tyrosinase model system. *Chem. Eur. J.*, 6(3), 2000.

[15] Griffiths J.S. *The Theory of Transition Metal Ions*. Cambridge Uniersity Press, New York, 1961.

[16] Decurtins S., Gütlich P., Köhler C.P., Spiering H., and Hauser A. Light-induced excited spin state trapping in a transition-metal complex: the hexa-1-propyltetrazole-iron(II) tetrafluorobate spin-crossover system. *Chemical Phuysics Letters*, 10(1), 1984.

[17] Cardona M. and Güntherodt G. *Light Scattering in Solids II*. Springer-Verlag Berlin Heidelberg New York, 1982.

[18] Bernath F. *Spectra of Atoms and Molecules*. Oxford University Press, Inc., 2 edition, 2005.

[19] Derek A. Long. *The Raman Effect*. John Willey and Sons, 2002.

[20] Peter Y. Yu and Cardona M. *Fundamentals of Semiconductors*. Springer Berlin Heidelberg New York, 3 edition, 2005.

[21] Loudon R. The raman effect in crystals. *Advances in Physics*, 13:423–482, 2006.

[22] Ting Guo. More power to x-rays: New developments in x-ray spectroscopy. *Laser and Photon Rev.*, 3(6):591–622, 2009.

[23] Koningsberger D. and Prins R. *X-Ray Absorption: Principles, Applications, Techniques of EXAFS, SEXAFS, and XANES*. John Wiley and Sons, 1988.

[24] Thompson A. and Vaughan D. *X-Ray data booklet*. University of California, 2 edition, 2001.

[25] Rehr J.J. and Albers R.C. Theoretical approaches to x-ray absorption fine structure. *Rev. Mod. Phys.*, 72(621), 2000.

[26] Rehr J.J. et al. New high-energy approximation for x-ray absorption near edge structure. *Phys. Rev. B*, 34(4350), 1986.

[27] Bressler C. and Chergui M. Molecular structural dynamics probed by ultrafast x-ray absorption spectroscopy. *Annu. Rev. Phys. Chem.*, 61:263–282, 2010.

[28] Stern E.A. Theory of the extended x-ray absorption fine structure. *Phys. Rev. B*, 10(3027), 1974.

[29] Sayers D.E., Stern E.A., and Lytle F.W. New technique for invetigating noncrystalline structures: Fourier analysis of the extended x-ray absorption fine structure. *Phys. Rev. Lett.*, 27(1204), 1971.

[30] John F. Watts and John Wolstenholme. *An introduction to Surface Analysis by XPS and AES*. John Willey and Sons, 2003.

[31] Wagner C.D., Riggs W.M., Davis L.E., and Moulder J.F. *Handbook of X-ray photoelectron spectroscopy*. Perkin-Elmer, 1979.

[32] James E. Castle. A wizard source of expertise in xps. *Surf. Interface Anal.*, 33:196–202, 2002.

[33] Yin L., Adler I., Tsang T., et al. Paramagnetism and shake-up satellites in x-ray photoelectron spectra. *Chemical physics letters*, 24(1), 1974.

[34] Kim K.S. Charge transfer transition accompanying x-ray photoionization in transition-metal compounds. *Journal of Electron Spectroscopy and Related Phenomena*, 3:217–226, 1974.

[35] Fiermans L., Hoogewijs R., and Vennik J. Electron spectroscopy of transition meta oxide surfaces. *Surface Science*, 47:1–40, 1975.

[36] Nesbitt H.W., Legrand D., and Bancroft G.M. Interpretation of Ni 2p XPS spectra of Ni conductors and Ni insulators. *Phys. Chem Minerals*, 27:357–366, 2000.

[37] Ghijsen J., Tjeng L.H., van Elp J., et al. Electronic structure of Cu_2O and CuO. *Physical Review B*, 38(16), 1988.

[38] Casa Software Ltd. *Peak fitting in XPS. XPS fitting manual*, 2006.

[39] Ament L.J.P. et al. Resonant inelastic x-ray scattering studies of elementary excitations. *Rev. Mod. Phys.*, 83(705), 2011.

[40] Rusydi A. et al. Electronic screening-enhanced hole pairing in two-leg spin ladders studied by high-resolution resonant inelastic x-ray scattering at Cu M-edges. *Phys. Rev. Lett.*, 113(6), 2014.

[41] Kotani A. and Shin S. Rsonant inelastic x-ray scattering spectra for electrons in solids. *Reviews of modern physics*, 71(1), 2001.

[42] Spectra-Physics. *Tsunami: Mode-Locked Ti::sapphire Laser*, 1995.

[43] Schulz B., Baeckström D., Budelmann D., et al. Fully reflective deep iltraviolet to near infrared spectrometer and entrance optics for resonant Raman spectroscopy. *Review of Scientific Instruments*, 76, 2005.

[44] Benjamin Grimm-Lebsanft. *Investigation of charge-transfer processes in modern synthetic bioinorganic copper complexes by steady state and time-resolved optical spectroscopy*. PhD thesis, Universität Hamburg, 2016.

[45] Spectra-Physics. *GWU-FHG: Flexible Harmonic Generator*, 2005.

[46] Tiedke K. et al. The soft x-ray free-electron laser FLASH at DESY: beamlines, diagnostics and end-stations. *New Journal of Physics*, 11, 2009.

[47] Kondratenko A. M. and Saldin E. L. Generation of coherent radiation by a relativistic electron beam in an ondulator. *Particle Accelerators*, 10:207–216, 1980.

[48] Ilka Flegel and Joerg Rossbach. The bright future of x-ray sources: Linac-based free electron lasers. *Europhysics News*, 31(6):12–14, 2008.

[49] Ayvazyan V., Baboi N., Bähr J., et al. First operation of a free-electron laser generating GW power radiation at 32 nm wavelength. *Eur. Phys. J. D*, 37:297–303, 2006.

[50] Dziarzhytski S. et al. Microfocusing at the PG1 beamline at FLASH. *J. Synchrotron Rad.*, 23:123–131, 2016.

[51] Martins M. et al. Monochromator beamline for flash. *Rev. Sci. Instrum.*, 77, 2006.

[52] Rübhausen M. et al. Technical design report, BMBF project number 05KS4GU2. Technical report, 2004.

[53] Balewski K., Brefeld W., Decking W., et al. Petra III: A low emittance synchrotron radiation source. Technical report, DESY, 2004.

[54] Franz H., Leupold O., Roehlsberger R., et al. Technical report: PETRA III: Desy's new high brilliance third generation synchrotron radiation source. *Synchrotron Radiation News*, 19:25–29, 2007.

[55] Göries D., Dicke B., Rödig P., et al. Time resolved pump and probe x-ray absorption fine structure spectroscopy at beamline P11 at PETRA III. *Review of Scientific Instruments*, 87, 2016.

[56] SPECS surface Nano Analystics GmbH. *SpecsLab Prodigy–Quick Guide*, 2013.

[57] *Praktikumsversuch: Oberfëchenanalytik mittels Röntgenphotoelectronspectroscopie (XPS)*, 2013.

[58] Keitel B. et al. Hartmann wavefront sensors and their application at FLASH. *J. Synchrotron Rad.*, 23:43–49, 2016.

[59] *Alignment manual from SORL*, 2000.

[60] Barkhouser R.H. and Raymond G. Ohl. Interferometric alignment and figure testing of large (0.5 m) off-axis parabolic mirrors in a challenging cleanroom environment. *Proc. SPIE*, 3782:601–614, 1999.

[61] Born M. and Wolf E. *Principles of optics.* Pergamon, New York, 1965.

[62] Cerrina F. and Sanches del Rio M. *Handbook of Optics.* New York. McGraw Hill, 3rd edition, 2010.

[63] Neddermeyer H. and Wiech G. Soft x-ray L-emission spectrum of aluminum. *Phys. Lett. A*, 31:17–18, 1970.

[64] Ederer D.L. et al. Electronic structure of the icosahedral and other phases of aluminum-manganese alloys studied by soft x-ray emission spectroscopy. *Phys. Rev. B.*, 37:8594–8597, 1988.

[65] Poletto L., Boscolo A., and Tondello G. Ultraviolet and x-ray detection, spectroscopy and polarimetry III. *Proc. SPIE*, pages 19–20, 1999.

[66] Dziarzhytski S. et al. Diffraction gratings metrology and ray-tracing results for an XUV Raman spectrometer at FLASH. *J. Synchrotron Rad.*, 25:138–144, 2018.

[67] Alexander Hoffmann, Janna Börner, Ulrich Flörke, and Sonja Herres-Pawlis. Synthesis and properties of guanidine-pyridine hybrid ligands and structural characterisation of their mono- and bis(chelated) cobalt complexes. *Inorganica Chemica Acta*, 362(4):1642–1652, 2006.

[68] Dicke B., Hoffmann A., Stanek J., et al. Transferring the entatic-state principle to copper photochemistry. *Nature Chemistry*, 10:355–362, 2018.

[69] Bressler C. and Chergui M. Ultrafast x-ray absorption spectroscopy. *Chemical Reviews*, 104(1781), 2004.

[70] Munira Chalil, Matthew A. Marcus, Amanda L. Smeigh, et al. Picosecond x-ray absorption spectroscopy of a photoinduced Iron(II) spin crossover reaction in solution. *J. Phys. Chem. A*, 110(1):38–44, 2006.

[71] Wojciech Gawelda, Melanie Johnson, Frank M. F. Groot, et al. Electronic and molecular structure of photoexcited $[Ru(II)(bpy)_3]^{2+}$ probed by picosecond x-ray absorption spectroscopy. *J. Am. Chem. Soc.*, 126:5001–5009, 2006.

[72] Smolentsev G. and Soldatov A. Quantitative local structure refinement from XANES: Multi-dimensional interpolation approach. *J. Synchrotron Rad.*, 13(19), 2006.

[73] Smolentsev G. and Soldatov A. Fitit: New software to extract structural information on the basis of XANES fitting. *Computational Materials Science*, 39(569), 2007.

[74] Rehr J.J., Kas J.J., Prange M.P., et al. Ab initio theory and calculations of x-ray spectra. *Comptes Rendus Physique*, 10(548), 2009.

[75] Uwe Gerstmann. Private correspondence. email from 02.05.2017, 2017.

[76] B. Ravel and M. Newville. Athena, Artmis, Hephaestus: data analysis for x-ray absorption spectroscopy using IFEFFIT. *J. Synchrotron Rad.*, 12:547–541, 2005.

[77] Shulman G. R., Yafet Y., Eisenberger P, and Blumberg W. Observation and interpretation of x-ray absorption edges in iron compounds and proteins. *PNAS*, 73(5):1384–1388, 1976.

[78] Briois V., Sainctavit Ph., Gary J. Long, and Fernande Grandjean. Importance of photoelectron multiple scattering in iron K-edge x-ray absorption spectra of spin-crossover complexes. full multiple scattering calculations for several iron(II) trispyrazolylborate and trispyrazolylmethane complexes. *Inorg. Chem.*, 40(5):912–918, 2001.

[79] Ulrich Herber, Rita Siris, Alexander Hoffmann, et al. A ccordinative study on Fe(II), Zn(II) and Cu(II) complexes with novel tridentate bis(pyrazolyl)methane complexes (submitted). *Zeitschrift für anorganishe und allgemeine Chemie*, 2018.

[80] Gawelda W. *Time-resolved x-ray absorption spectroscopy of transition metal complexes*. PhD thesis, Ecole Polytechnique de Lausanne, 2006.

[81] Britz A. *Ultrafast X-ray Spectroscopies of Transition Metal Complexes Relevant for Catalysis*. PhD thesis, Universität Hamburg, 2016.

[82] Bressler C., Saes M., Chergui M., Abella R., and Pattison P. Optimizing a time-resolved x-ray absorption experiment. *Nuclear Instruments and Methods in Physics Research A*, 467–468:1444–1446, 2001.

[83] Prof. Dr. Sonja Herres-Pawlis. Private correspondence. email from 25.07.2017, 2017.

[84] B. Grimm-Lebsanft, C. Brett, F. Strassl, et al. A cryostate for low temperature resonance raman measurements on operando oxygenated bioinorganic model complexes. *Inorganica Chimica Acta*, 2017.

[85] F. Stassl, B. Grimm-Lebsanft, Dieter Rukser, et al. Oxygen activation by copper complexes with an aromatic bis(guanidine) ligand. *Eur. J. Inorg. Chem*, pages 3350–3359, 2017.

[86] Daniella Schurr, Florian Strassl, Patricia Liebhäser, et al. Decay kinetics of sensitive bioinorganic species in a superfocus mixer at ambient conditions. *React. Chem. Eng.*, 1:485–493, 2016.

[87] Sonja Herres, Andreas J. Heuwing, Ulrich Flörke, et al. Hydroxylation of a methyl group: synthesis of $[Cu_2(btmmO)_2I]$ and of $[Cu_2(btmmO)_2]_2$ containing the novel ligand (bis(trimethylmethoxy)guanidino)propane (btmmo) by copper-assisted oxygen activation. *Inorg. Chim. Acta*, 358:1089–1095, 2005.

[88] Martin Rohmüller, Alexander Hoffmann, Chrisitan Thierfelder, et al. The Cu_2O_2 torture track for a real-life system: $[Cu_2(btmgp)_2O_2]^{2+}$ oxo and peroxo species in density functional calculations. *J. Comput. Chem.*, 36:1672–1685, 2015.

List of publications

1. **Mykola Biednov**, Benjamin Dicke, Günter Brenner, Holger Weigelt, Barbara Keitel, Michael Rübhausen and Siarhei Dziarzhytski. Alignment of the aberration-free VUV Raman monochromator at FLASH (in preparation). *J. Synchrotron Rad.*, 2018.

2. B. Dicke, A. Hoffmann, J. Stanek, M. S. Ramp, B. Grimm-Lebsanft, F. Biebl, D. Rukser, B. Maerz, D. Göries, M. Naumova, **M. Biednov**, G. Neuber, A. Wetzel, S. M. Hofmann, P. Roedig, A. Meents, J. Bielecki, J. Andreasson, K. R. Beyerlein, H. N. Chapman, C. Bressler, W. Zinth, M. Rübhausen and S. Herres-Pawlis. Transferring the entatic-state principle to copper photochemistry. *Nature Chemistry*, 10:355–362, 2018.

3. Maria Naumova, Dmitry Khakhulin, Mateusz Rebarz, Martin Rohmüller, Benjamin Dicke, **Mykola Biednov**, Alexander Britz, Shirly Espinoza, Benjamin Grimm-Lebsanft, Miroslav Kloz, Norman Kretzschmann, Adam Neuba, Jochen Ortmeyer, Roland Schoch, Jakob Andreasson, Matthias Bauer, Christian Bressler, Wolf Gero Schmidt, Gerald Henkel and Michael Rübhausen. Structural dynamics upon photoexcitation–induced charge transfer in a dicopper(I)-disulfide complex. *Phys. Chem. Chem. Phys.*, 20:6274–6286, 2018.

4. B. Grimm-Lebsanft, C. Brett, F. Strassl, D. Rukser, **M. Biednov**, F. Biebl, M. Naumova, A. Hoffmann, L. Akinsinde, D. Brückner, S. Herres-Pawlis and M. Rübhausen. A cryostat for low temperature resonance Raman measurements on *operando* oxygenated bioinorganic model complexes. *Inorganica Chimica Acta*, 2017.

5. Florian Strassl, Benjamin Grimm-Lebsanft, Dieter Rukser, Florian Biebl, **Mykola Biednov**, Calvin Brett, Ricardo Timmermann, Fabian Metz, Alexander Hoffmann, Michael Rübhausen and Sonja Herres-Pawlis. Oxygen Activation by Copper Complexes with an Aromatic Bis(guanidine) ligand. *Eur. J. Inorg. Chem.*, pages 3350–3359, 2017.

Publications, not related to the PhD research area

1. **Mykola Biednov**, Tatyana Lebedeva and Pavlo Spilovuy. Gold and Aluminum based surface plasmon resonance biosensors: sensitivity enhancement. *Proc. SPIE 9506*, doi: 10.1117/12.2177992, 2015.

Eidesstattliche Versicherung / Declaration on oath

Hiermit versichere ich an Eides statt, die vorliegende Dissertationsschrift selbst verlasst und keine enderen als die angegebenen Hilfsmittel und Quellen benutzt zu haben.

Die eingereichte schriftliche Fassung entspricht der auf dem elektronishen Speichermedium.

Die Dissertation wurde in der vorgelegten oder einer ähnlichen Form nicht shon einmal in einem früheren Promotionsverfahren angenommen oder als ungenügend beurteilt.

Hamburg, den

Unterschrift der Doktorandin / des Doktoranden